Imperial College of Science, Technology and Medicine
Department of Mechanical Engineering

Data Processing Technique and its Applications in Sheet Metal Forming Processes

Yang Zheng

Submitted in part fulfilment of the requirements for the degree of
Doctor of Philosophy in Mechanical Engineering of Imperial College London
and the Diploma of Imperial College, Dec 2019

Declaration of Originality

This is to certify that the intellectual content of this thesis is the product of my own work under the supervision of Dr Liliang Wang at the Department of Mechanical Engineering of Imperial College London. I have clearly referenced all sources used in this thesis. This thesis has not been submitted yet for a degree or diploma at any other university or institution.

Yang Zheng
Department of Mechanical Engineering
Imperial College London
25 Dec 2019

Declaration of Copyright

The copyright of this thesis rests with the author and is made available under a Creative Commons Attribution Non-Commercial No Derivatives licence. Researchers are free to copy, distribute or transmit the thesis on the condition that they attribute it, that they do not use it for commercial purposes and that they do not alter, transform or build upon it. For any reuse or redistribution, researchers must make clear to others the licence terms of this work.

Abstract

In recent years, Finite Element Analysis (FEA) has been widely used by the metal forming industry in conjunction with traditional practical techniques, resulting in an accumulation of vast volumes of FEA results. With the increasing trend for the application of cloud computing services to FE software, the traditionally independent manufacturing sectors are being transformed into cloud connected communication networks through horizontal and vertical integration solutions. Industrial Research is shifting towards an eco-friendlier approach through exchanging, sharing and utilising of these data. Advancements in these newly developed technologies have brought new challenges to the sheet metal forming industry, leading to the emergence of a unique research field of data processing technologies for metal forming processes.

One of the most significant issues in the field is the extraction of insightful information from information-absent FEA data. In this work, the focus is on a dataset comprising of vast volumes of experimentally verified FEA data from various part geometries. Several data classification algorithms were developed using physical-based models and machine learning models, respectively, enabling a digital characterisation of finite elements from sheet metal forming process simulations in the absence of spatial or visual data. Machine learning models were developed to recognise the geometric information by over 90 percent accuracy. Based on the understanding of thermo-mechanical history of sheet metal forming processes, including stress state, such as the Lode parameter and stress triaxiality, several physical-based algorithms were then developed which were rigorous in recognising the flange zone, flat bottom and side wall with an excellent accuracy.

In addition, research in metal forming processes has traditionally followed the convention of validating hypotheses with repeatable experimental trials. However, the reliable characterisation of boundary conditions remains challenging, which can be partly explained by the fact that the real boundary conditions in metal forming processes are not well understood, especially for coefficient of friction (COF) and interfacial heat transfer coefficient (IHTC). A systematic data visualisation technique was developed to generate a tribo-map and an IHTC-map, characterising the thermo-mechanical history of a sheet metal process, including relative sliding distance, contact pressure and temperature difference between the workpiece and tool, which enables an insight into the evolutionary boundary conditions at different workpiece-tool interfaces. Such a data-driven approach is also adopted in this work to shape the experimental strategies by in-

troducing variable contact/sliding conditions, and the friction of coefficient and interfacial heat transfer coefficient obtained at these variable testing conditions were found to have excellent match with numerical models.

Acknowledgements

I would like to express my sincerest gratitude to my supervisor Dr Liliang Wang for the continuous unconditional support, guidance and encouragement during my PhD journey. I appreciate all the extraordinary knowledge you have taught that enrich my understanding, all the thoughtful vision you have shared that broaden my horizon and all the invaluable advice you have given that benefit me for life. I would also like to thank my second supervisor Prof Jianguo Lin for always being there when I needed his support and guidance.

I would like to acknowledge my project PhDs and PDRAs, Dr Yiran Hu, Dr Haoxiang Gao, Dr Jun Liu, Dr Omer El Fakir and Dr Denis J. Politis, my co-authors, Dr Xiaochuan Liu and Ms Xiao Yang and many MEng and MSc students, Vivian Liang, Xinyang Yuan, Yuxuan Liu, Geng Lin Chong for their support, advice and help on research, experiment and academic writing at different stages of my 4 years PhD study.

A special thank to Dr Ailing Wang who guided me at the beginning of my PhD and always giving me excellent idea during my study. Shout out my F4 friends, Dr Xiaochuan Liu, Dr Yuhao Sun and Dr Qunli Zhang for the happiness and difficulties we experienced during our PhD life together, in memory of the time of every Chinese New Year and Christmas in London.

I also would like to give thanks to all the friends in MoM group Zhaoheng Cai, Kehuan Wang, Xi Luan, Saksham, Matt, Kang and my gymbuddy Xiaochen Lu and Jun Liu, my roommates Jinghua Zheng and Qinmeng Luan, my buddy Dr Diyang Li and Victor Peng. I also wish to thank my friend Ah Lue for his long distance support.

Last but not the least, I would like to thank my family and my girlfriend, Han, who are supporting me spiritually throughout my PhD studies. I would not achieved such results without you. To you this thesis is dedicated.

'He is a man whose determination makes forget to eat, whose happiness makes forget his troubles and who knows not that old age is stealing upon him.'

– *Confucius*

Contents

Declaration of Originality i

Declaration of Copyright iii

Abstract v

Acknowledgements vii

List of Figures xv

List of Tables xxiii

List of Publication xxv

Nomenclature xxix

1 Introduction 1

1.1 Background 1

1.2 Motivation and objectives 4

1.3 Thesis structure 6

2 Literature review **8**

2.1 Lightweight sheet metal forming process 9

2.1.1 Fast Light Alloys Stamping Technology (FAST) of aluminium alloy . . . 10

2.1.2 Fast Warm Stamping (FWS) process of steel 11

2.1.3 Hot stamping process for titanium alloy 12

2.2 Data representation in metal forming process 14

2.2.1 Flow stress, strain and strain rate 14

2.2.2 Stress state, Lode parameter and stress triaxiality 16

2.2.3 Product geometry 18

2.3 Classification using machine learning technique 19

2.3.1 Single neuron neural network (SNNN) and logsitic regression 19

2.3.2 Feedforward neural network (FFNN) 22

2.3.3 Recurrent neural network (RNN) 22

2.4 Characterisation of boundary condition for sheet metal forming processes 23

2.4.1 Characterisation of coefficient of friction (COF) 23

2.4.2 Characterisation of interfacial heat transfer coefficient (IHTC) 26

3 Data Collection and pre-processing **28**

3.1 Introduction 28

3.2 Data collection 29

3.3 Data pre-possessing 30

3.3.1 Data clearing and weighting 30

3.3.2 Data standardisation and normalisation 31

3.3.3 Data labelling for geometric features 32

4 Development of machine learning based data classifier 35

4.1 Summary 35

4.2 Introduction 36

4.3 Methodology 37

4.3.1 Preparation of training set 37

4.3.2 Model architecture 38

4.3.3 Model evaluation methods 40

4.4 Results of logistic regression model for binary classification 42

4.5 Results of Feedforward neural network 44

4.5.1 One-hidden layer FFNN 44

4.5.2 Multi hidden layer feedforward neural network 46

4.6 Recurrent neural network 48

4.6.1 Effect of learning rate and use of non-linearity in FC-1 48

4.6.2 Effect of layer number in LSTM 48

4.6.3 Methods of reducing classifier variance 49

4.6.4 Comparison of final models 52

5 Development of physics based data filtering technique 55

5.1 Summary 55

5.2 Strain-based filter 55

5.2.1 Strain related parameters preparation 56

5.2.2 Filter Mechanism and criterion 56

5.2.3 Strain filter results 58

5.3 Temperature drop filter 58

5.4 Unified thermo-mechanical evolutionary algorithms 60

5.4.1 Thermo-mechanical data review 61

5.4.2 Development of model 68

5.5 Results and discussion 70

6 Development of a data visualisation technique 73

6.1 Summary 73

6.2 Introduction 74

6.3 Tribological Data processing for hot stamping of aluminium alloys 75

6.4 Results and discussion 81

6.4.1 Overall contact conditions at tool surface 81

6.4.2 Contact condition evolution during the wear process at the tool surface . 82

7 Development of data-driven experiment for variable contact conditions 88

7.1 Experimental methods of the tribology test 88

7.1.1 Test material 88

7.1.2 Test equipment and setup 89

7.1.3 Results and discussion 90

7.2 Experimental setup of the interfacial heat transfer test 92

7.2.1 Test material 92

7.2.2 Test equipment 92

7.2.3 Results and discussion 93

8 Conclusion **96**

8.1 Thesis review 96

8.2 Summary of thesis achievements 96

8.3 Future work 98

A Appendix: The galling behaviour of advanced coating contacts with aluminium alloy during sliding wear **99**

A.1 Introduction 99

A.2 Material and experiment method 100

A.3 Results and discussion 101

A.3.1 Effects of coating on the evolution of friction coefficient 101

A.3.2 Surface topography analysis: galling effect 104

A.4 Conclusion 106

B Appendix: FE simulation of aluminium galling inducted forming tool failures under multi-cycle loading conditions **107**

B.1 Introduction 107

B.2 Interactive friction model 109

B.3 Coating design: a feasible study 111

B.4 Results and discussion 111

B.5 Conclusion 116

C Appendix: Data-driven tensile test guidelines for hot stamping of aluminium alloys **117**

C.1 Introduction 117

C.2 Methodology: data-driven approach for tensile test 118

C.3 Results and discussion: thermo-mechanical characteristics of the hot aluminium stamping technology 119

C.4 Conclusion 121

List of References **121**

List of Figures

1.1 SmartForming® cloud finite element analysis platform and the data-driven manufacturing industry workflow 3

1.2 Strategy of test guidance generated based on data analysis 5

1.3 Methodology for extracting of insightful information from information-absent FEA data 6

1.4 Schematic for the key contributions of the thesis 7

2.1 Schematic for main contents covered in literature review 8

2.2 (a) A typical part formed in a stamping or draw die showing the die ring, but not including the punch or blankholder, (b) section of tooling in a draw die showing the punch and Binder 9

2.3 Schematic for forming 6 series aluminium alloy using Fast light Alloys Stamping Technology (FAST) and conventional hot stamping technique 11

2.4 Schematic for forming high strength steel using Fast-Warm Stamping and conventional hot/warm stamping processes 12

2.5 Schematic of the hot stamping process of titanium alloy (a) during heating of the sample, (b)at the positioning stage, (c) during forming and (d)at the final stage. 13

2.6 The stress/strain distribution on the Von Mises plane development, where x-axis is the Lode parameter and y-axis is the equivalent stress (Yuan, 2008) 17

2.7 Illustration of machine learning model 19

2.8 Single Neuron Neural Network (left) and logistic function (right) 20

2.9 3 Layer Neural Network (the two diagrams represent identical neural network) . 22

2.10 Schematic illustration of simplified tests for sheet meta forming Bay et al. (2008), including (1) Strip drawing with flat dies, (2) Bending under tension, (3) Drawing with tangential compression, (4) Bending with tangential compression, (5) Draw bead testing, (6) Strip -tension testing, (7) Hemispherical stretching, (8) Strip reduction testing 24

3.1 Key elements of machine learning based data classification technique. **a** Schematic view of an example data set, **b** creation of a prediction model via the fingerprinting and learning steps. N and M are the number of training examples and the number of fingerprint components, and **c** problem solving by prediction model . 29

3.2 Through a preliminary principal component analysis, the dimensionality (parameters) of the raw data reduces from 132 to 3. The three most important parameters are initial temperature, final temperature and final strain, indicated as C1, C2 and C3, respectively. A sample of the raw data is illustrated in a 3D scatter plot. The colour indicates the geometric region of the element, suggesting that simple data processing technique did not work well on these datasets. . . . 30

3.3 Secondary polynomial surface function fitting by using the x,y coordinates of 9 elements, one centre element and 8 neighbouring elements 33

3.4 Labelling results on a sample component, illustrating the Blank holding, Flat bottom, Vertical wall, Inclined wall, shoulder and Corner areas respectively . . . 34

4.1 Binary classification problem with 2-dimensional input feature 36

4.2 Matrix of input data of all training elements 37

4.3 Model architecture for (a) logistic regression (b) feed-forward neural network and (c) deep recurrent neural network 39

4.4 Example of a confusion matrix for describing the performance of a classification model 41

4.5 The confusion matrix of logistic regression model using (a) strain data set and (b) full data set at optimised learning rate 43

4.6 The learning curve of logistic regression classification with different learning rate, 0.05, 0.1, 1 and 3 respectively 43

4.7 The confusion matrix of test data sets of one hidden layer FFNN model of (a) 4, (b) 8, (c) 12, (d) 20 neurons, respectively 45

4.8 The confusion matrix of three layer FFNN model 47

4.9 The confusion matrix of test set of FFNN models with (a) three hidden layers, (b) four hidden layers and (c) five hidden layers 47

4.10 Dropout of Neural Network 49

4.11 The confusion matrix for final 2 layer LSTM model 52

4.12 The confusion matrix for final 3 layer LSTM model 53

4.13 The confusion matrix for final 2 layer with leaky-ReLU activation LSTM model 53

4.14 The confusion matrix for final 2 layer bi-direction LSTM model 54

5.1 Schematic of the strain-based filter, dark blue part represents left-over elements, and the remaining parts are filtered elements for die cavity region, and each step the left-over is sent into the next level of filter 57

5.2 Example of data used in physical-based classification model research. Normalized pressure of raw data are illustrated along the normalised forming process, showing different patterns with various geometric locations. 61

5.3 Example of data used in physical-based classification model research. Strain rate of raw data are illustrated along the normalised forming process, showing different patterns with various geometric locations. 62

5.4 Example of data used in physical-based classification model research. Major strain of raw data are illustrated along the normalised forming process, showing different patterns with various geometric locations. 62

5.5 Example of data used in physical-based classification model research. Normalized temperature of raw data are illustrated along the normalised forming process, showing different patterns with various geometric locations. 63

5.6 Example of data used in physical-based classification model research. Normalized major stress of raw data are illustrated along the normalised forming process, showing different patterns with various geometric locations. 64

5.7 Example of data used in physical-based classification model research. Stress triaxiality stress of raw data are illustrated along the normalised forming process, showing different patterns with various geometric locations. 64

5.8 Stress state evolution data of finite element used in physical-based classification model research, showing the load parameters and stress triaxiality with different geometric features in sheet metal forming processes 67

5.9 Random forest based feature importnace analysis 68

5.10 Discrete fitting result of major strain, normalised temperature and stress triaxility for blank holding area, flat bottom and side wall region, respectively 69

5.11 Confusion matrix results of classification algorithms for (a) blank holding area, (b) flat bottom and (c) side wall regions, respectively 71

6.1 Data processing in the context of closely related processes of in data-driven decision making in sheet metal forming research 75

6.2 Tribological data processing procedure 77

6.3 Schematic of relative sliding velocity calculation 79

6.4 (a) Probability and (b) temperature difference distributions as a function of the contact pressure and wear velocity on the tool surface during hot stamping of AA6xxx aluminium alloys 82

6.5 (a) Probability and (b) temperature difference distributions as a function of the contact pressure and wear distance on the die surface during hot stamping of AA6xxx aluminium alloys 83

6.6 filtered visualisation of tool life prediction 85

6.7 (a) Probability and (b) temperature difference distributions as a function of the contact pressure and normalised wear distance on the punch surface 86

6.8 (a) Probability and (b) temperature difference distributions as a function of the contact pressure and normalised wear distance on the blankholder surface 86

6.9 (a) Probability and (b) temperature difference distributions as a function of the contact pressure and wear distance on the die surface with the drawbead during hot stamping of AA6xxx aluminium alloys 87

7.1 Schematic illustration of a pin-on-disc test (left) and Anton Paar pin-on-disc test setup (right) 89

7.2 Friction test with load jump condition 91

7.3 Schematic of the IHTC test facility, including (1) a pedestal, (2) a die, (3) a frame, (4) a workpiece, (5) two blankholders, (6) two guide pillars and (7) insulating sliding block 93

7.4 IHTC experimental setup in Gleeble 93

7.5 Contact pressure and contact area distributions in the progression of the hot stamping process 94

7.6 (a) Variable contact pressure evolution (b) IHTC evolution, and the comparison between the experimental and simulated temperature evolutions with data-driven IHTC test 95

A.1 The evolution of friction coefficient at room temperature of a) substrate 1 sliding with AA6082 pin, b) substrate 1 sliding with AA7075 pin, c) substrate 2 sliding with AA6082 pin and d) substrate 2 sliding with AA7075 pin under various coatings 102

A.2 The evolution of friction coefficient at 300°C of a) substrate 1 and b) substrate 2 under various coatings with AA 6082 pin 103

A.3 The evolution of friction coefficient of substrate 3, substrate 2-AlCrN and substrate 1-AlCrN with AA 6082 pins at a) 25°C and b) 300°C 103

A.4 Evolution of friction coefficient of a) substrate 1-AlCrN, b) substrate 2-AlCrN, c) substrate 3 at 25°C and 300°C with AA 6082 pin 104

A.5 Surface topography analysis of a) substrate 3, b) substrate 1-AlCrN and c) substrate 1-CrN with AA 6082 pin at 25°C, 300°C, 450°C 105

B.1 Evolution of friction coefficient by experimental data and friction model under different loads 109

B.2 Pam-stamp simulation of U-shape bending process, presenting the (a) first, (b) forming and (c) final stages of the process; the model consists of a blank, blank holder, punch and die 111

B.3 Remaining coating thickness distributions on the die after (a)500 cycles (b) 20000 cycles (c) 40000 cycles of forming operations detailed wear features, and remaining coating thickness distributions on the (d) die (e) punch (f) top blank holder, after 40000 cycles of forming operations, and coating distribution of (g) die (h) punch and (i) top blank holder when coating breaks down 112

B.4 Wear of volume after 40000 cycles of forming operation 113

B.5 Typical pressure distribution on the (a) die (b) punch (c) top blank holder for U-shape bending, and relative sliding distance distribution on the (d) die (e) punch (f) top blank holder for U-shape bending at blank holding force of 30 kN 114

B.6 Volume of wear on Die (right) and Blank holder (left) after 40000 cycles of forming operation 115

B.7 Designed coating thickness of die, punch and top blank holder for 40000 cycles . 115

C.1 Smartforming simulation database - 'strategy' implementation process 118

C.2 Temperature and strain rate distribution for AA6082 formed under hot stamping conditions 120

C.3 Temperature and strain rate distribution for AA6082 formed under hot stamping conditions 121

List of Tables

2.1 Significant variables in sheet metal forming 14

2.2 Contact conditions of different tribological testing methods in sheet metal forming 26

3.1 Labelling criterion for finite element models with known geometric information . 34

4.1 Scale label for each geometric feature 38

4.2 Accuracy of logistic regression classification using different data set at different learning rate 42

4.3 Accuracy of data filter for different neurons in a one hidden layer FFNN 44

4.4 Accuracy of FFNN models with multiply hidden layer 47

4.5 Effect of learning rate and nonlinearity in FC-1 layer on RNN model performance, using batch size of 4096 at 2000 iterations 48

4.6 Effect of number of LSTM recurrent layer on RNN model performance, using batch size of 4096 at 5000 iterations 49

4.7 Study of dropout in fully connected layers 50

4.8 Investigation on the effect of L2 regularization 51

4.9 Investigation on the regularisation effect of batch size at different Learning Rates 51

4.10 Performance of various fined tunned models 52

5.1 Parameters in heat transfer filter 59

5.2 Model parameter obtained from uni-variate model 70

7.1 Technical Specifications for the Anton Paar high temperature tribometer 90

7.2 Technical Specifications for Gleeble 3800 thermo-mechanical simulator 92

B.1 Material constants and model parameters of the friction model 110

B.2 Designed coating thickness applied on forming tool for U-shape bending case study115

List of Publication

Peer-reviewed journal publications

1. Hu, Y., **Zheng, Y.**, Politis, D.J., Masen, M., Cui, J. and Wang, L., 2019. Development of an interactive friction model to predict aluminium transfer in a pin-on-disc sliding system. *Tribology International*, 130, pp.216–228.

2. Wang, A., **Zheng, Y.**, Liu, J., El Fakir, O., Masen, M. and Wang, L., 2016. Knowledge Based Cloud FE simulation - data-driven material characterization guidelines for the hot stamping of aluminium alloys. *Journal of Physics: Conference Series*, 734, 032042.

3. Liu, X., El Fakir, O., **Zheng, Y.**, Gharbi, M.M. and Wang, L., 2019. Effect of tool coatings on the interfacial heat transfer coefficient in hot stamping of aluminium alloys under variable contact pres-sure conditions. *International Journal of Heat and Mass Transfer*, 137, pp.74–83.

4. Yang, X., Hu, Y., **Zheng, Y.**, Politis, D.J. and Wang, L., 2019. Coating effects on the galling behaviour of aluminium metal forming processes. *Materials Science and Engineering: Conference Series*, 651, p.012022.

5. Liu, J., Wang, A., **Zheng, Y.**, Liu, X., Gandra, J., Beamish, K., Petre, A. and Wang, L., 2017. Hot stamping of AA6082 tailor welded blanks for automotive applications. *Procedia Engineering*, 207, pp.729–734.

6. Yang, X., Zhang, Q., **Zheng, Y.**, Liu, X., Politis, D.J., El Fakir, O. and Wang, L., 2019. Development of an interactive friction model to predict high-temperature friction coefficient evolution and lubricant breakdown behaviour. *Friction*, Under review.

7. Hu, Y., Gharbi, M.M., Liang, V., **Zheng, Y.**, Politis, D.J. and Wang, L., 2018. The Galling Behavior of Advanced Coating Contacts with Aluminium Alloy during Sliding Wear. *Key Engineering Materials*, 767, pp.117–123.

8. Wang, A., El Fakir, O., Liu, J., Zhang, Q., **Zheng, Y.** and Wang, L., 2019. Multi-objective finite element simulations of a sheet metal forming process via a cloud-based platform. *The International Journal of Advanced Manufacturing Technology*, 100(9-12), pp.2753–2765.

9. Gao, H., Politis, D.J., Luan, X., Ji, K., Zhang, Q., **Zheng, Y.**, Gharbi, M.M. and Wang, L., 2017. Forming limit prediction for AA7075 alloys under hot stamping conditions. *Journal of Physics: Conference Series*, 896, 012089.

Conference paper

1. **Zheng, Y.**, Wang, A., Liu, X., Ji, K., Said, R. and Wang, L., Knowledge based cloud FE simulation: data-driven material characterization guidelines for hot stamping of aluminium alloys. *Conference of Chinese Society for Technology of Plasticity*, Jinan, China, 2017.

2. **Zheng, Y.**, Hu, Y., Gharbi, M.M., Politis, D.J. and Wang, L., Development of coating design guidelines for a sheet metal forming tool-a feasibility study. *Tool Conference*, Bratislava, Slovakia, 2016.

3. Hu, Y., **Zheng, Y.**, Yang, X., Politis, D.J., Wang, L., Gharbi, M.M. and Cui, J., FE simulation of aluminium galling induced forming tool failures under multi-cycle loading conditions: A feasibility study. *International Conference On Advanced High Strength Steel And Press Hardening*, Hefei, China, 2018.

4. Liu, X., **Zheng, Y.**, El Fakir, O., Said, R. and Wang, L., Characterisation of the contact pressure dependent inter-facial heat transfer coefficient for a hot stamping process following a data driven approach. *International Conference on New Forming Technology*, Bremen, Germany, 2018.

5. Wang, A., **Zheng, Y.**, Liu, J., El Fakir, O., Masen, M. and Wang, L., Knowledge based cloud FE simulation a multi-objective FEA system for advanced FE simulation of hot stamping process. *International Conference and Workshop on Numerical Simulation of 3D Sheet Metal Forming Processes*, Bristol, UK, 2016.

6. Hu, Y., **Zheng, Y.**, Politis, D.J., Wang, L. and Gharbi, M.M., Investigation of galling behaviors between an aluminum alloy and metal forming tool. *International Conference on Advanced High Strength Steel and Press Hardening*, Xian, China, 2016.

7. El Fakir, O., Lim, C., Haque, F., **Zheng, Y.**, Liu, X. and Wang, L., Process optimisation using a data guided online platform. *International Conference on the Technology of*

Plasticity, Columbus, USA, 2020.

Patent

1. Dhawan, S., El Fakir, O., Zhang, Q., Wang, A., **Zheng, Y.**, Wu, G., Wang, L., An Online Database for Hosting and Executing Numerical Models. Patent file number: 201911116210.6.

Nomenclature

α	Learning rate
$\bar{\sigma}$	Flow stress
$\bar{\varepsilon}$	Equivalent strain
$\dot{\bar{\varepsilon}}$	Equivalent strain rate
$\dot{\varepsilon}$	Strain rate
$\dot{r}$	Heat generation
κ	Heat generation efficiency
μ_σ	Lode parameter
ρ	Density
σ	Stress
σ_1	First principal stress
σ_2	Second principal stress
σ_3	Third principal stress
σ_y	Von mises yield strength
ε	Strain
ε_1	First principal strain
ε_2	Second principal strain

ε_3 Third principal strain

c_1 Strain filter constant

f_c Parameter factor of physical based model

F_t Criteria factor of physical based model

s_f Final step

s_i Initial step

t_f Time indicator of physical based model

v_f Forming speed

A Area of the finite element

b bias

BH Blank holding area

C Convexity

c Specific heat capacity

COF Coefficient of friction

DC Die cavity

FB Flat bottom area

FC Full connected layers

FEA Finite element analysis

FFNN Feedforward neural network

FWS Fast warm stamping

i Element number

IHTC Interfacial heat transfer coefficient

J Cost of the function

K Strength coefficient

k Internal heat transfer coefficient

LSTM Long short-term memory

m Number of mini-batch

n Strain hardening exponent

P Contact pressure

RNN Recurrent neural network

s Step number

SNNN Single neuron neural network

SW Side wall

T Temperature

V Volume

W Weighting ratio

w Weights

Chapter 1

Introduction

1.1 Background

Metal forming is one of most classic manufacturing crafts whose history can be traced back to the early stages of civilisation, which remains of particular relevance for model industry and society in most products encountered to this day. With the 4th Industrial Revolution, Metal forming is now experiencing a transformation, from the way metal forming products are designed and tested, through to how they're manufactured, delivered and maintained (Zhou et al., 2015). The Cyper-Physical System (PCS), Internet of Things (IoT), Big data analytic, Artificial Intelligence (AI), Machine Learning are the key techniques leading this transformation, connecting together previously isolated manufacturing sectors into interconnected communicating-actuating networks (Qin et al., 2016). It is aimed to achieve higher efficiency and stronger economic ties in industry through horizontal and vertical integration of R&D data, knowledge and other capabilities to realise intelligent manufacturing (de Baas, 2010).

Finite Element Analysis (FEA) plays a critical role in metal forming industry. In particular, knowing the relationship between material response and the applied fields, is an essential constituent for predicting the thermo-mechanical behaviour of metal with sophisticated conditions, which enables the optimisation of forming processes (Ablat and Qattawi, 2017). A considerable amount of research to address different aspects of problems on numerical analysis also

effectively enhanced the functionality of FEA, like formability(Bruschi et al., 2014; Isik et al., 2014), springback (Chongthairungruang et al., 2013; Li et al., 2002), friction modelling (Nielsen and Bay, 2018) and heat transfer modelling (Liu et al., 2017). The high capability of FEA to replicate the metal forming processes leads its wide utilisation in most industrial sectors, such as raw material production, components and forming tools design, manufacturing and paint bake processes. The FE results produced makes it an emerging data source to improve the efficiency of the manufacturing system. However, these data are still in isolation within the industrial sectors.

Although FEA software is able to predict most of the thermo-mechanical behaviours like stress, strain and temperatures of components during forming processes, researchers typically require a deeper analysis, including the effects of pre-form annealing on material formability (Luo et al., 2008), the impact of artificial/natural ageing on post-form strength(Myhr et al., 2015), and the critical tool life cycle (Binder et al., 2017). Predicting these effects involves solving time- and temperature-dependent constitutive equations, and new advanced material models are constantly being proposed to address them. However, integrating such models into FEA software requires significant effort, and has only been done for a very small selection of them. The increasing adoption of cloud computing service can therefore be supplemented by an online platform allowing these advanced models to be digitised and executed alongside FEA software.

Innovative online FEA platform, SmartForming® was most recently developed by the Imperial College London Metal Forming Group to allow frontier knowledge to be implemented with advanced numerical models via a cloud based system (Wang et al., 2016; Wang, El Fakir, Liu, Zhang, Zheng and Wang, 2019). The schematic as shown in Fig. 1.1. The platform can provide data inputs for, or compute data outputs from, FE software, with the advanced models being divided into two types, pre-FEA models and post-FEA predictive models. Flow-stress, IHTC-mate(Liu et al., 2019) and Tribo-mate are pre-FEA modules, corresponding to three essential inputs in conventional FE software: flow stress data, the interfacial heat transfer coefficient (IHTC) and the coefficient of friction (COF), respectively. An automatic fitting model is also available for calibrating experimental testing results against numerical models. In terms of post-FEA models, Tailor focuses on forming process optimisation based on customised

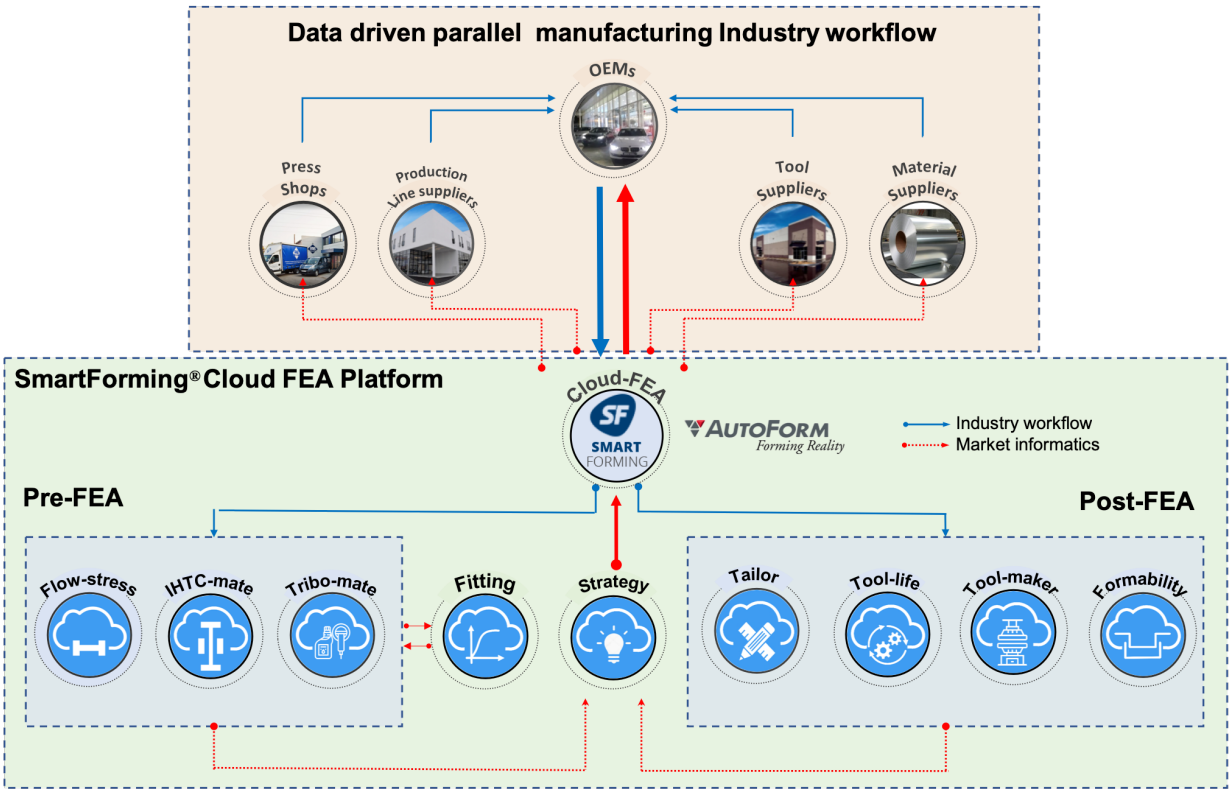


Figure 1.1: SmartForming® cloud finite element analysis platform and the data-driven manufacturing industry workflow

requirements(Zhang et al., 2019), Tool-life aims to predict the life-time of lubricant and forming tools over multiple production cycles(Hu et al., 2018), Tool-maker helps tool designers to assess the quenching rate of the forming process (Liu et al., 2016), and Formality identifies critical regions in a component where necking/failure may occur (Gao et al., 2017). Strategy model is referring to a data-driven material testing scheme which will be introduced in chapters 6 and 7.

Such cloud FEA services are central to knowledge digitisation as well as intelligent manufacturing, providing essential CAE tools more widely but also enabling streamlined knowledge and data exchange, particularly between researchers and researchers, researchers and industry users. From an academic point of view, the platform provides a novel path to publish new knowledge in a digitised approach and enhance the academic communication in more direct way. The frontier knowledge with these advanced models are more likely to be implemented by commercial FEA simulation software to enhance analytical capacity. It not only bridges the gap between scientific knowledge and practical implementation, it also realises the value

of knowledge created by academic researchers. From an industry prospective, the platform enables end-to-end collaboration across research and industrial sectors and along the entire value chain, which can result in additional benefits such as flexible production and distributed manufacturing. Manufacturers would be able to select different grades of raw material, and produce different versions of a product with regards to individual customers' specifications, such as the setup of the paint bake cycle and the requirement for the final strength. Customers would also be able to find local material suppliers and manufacturers to receive items faster, reducing manufacturers' inventory and shipping costs. The cumulative data will turn into big data, with the potential to implement data analytical methods to deliver additional value from the platform. In recent years, traditional FEA software companies, like *AutoForm*® and *ESI*® are developing their own cloud services as a computing resource. All these new technologies have therefore brought new challenges to metal forming engineers and researchers, leading to the emergence of a unique research field of data processing techniques in metal forming processes.

1.2 Motivation and objectives

Over the past thirty years, data science has developed from one discipline to a multi-disciplinary field that employs mathematical algorithms and scientific theories to extract insightful information from dataset, which is particularly useful for industrial applications. The metal forming industry is a well-established industry that generates vast volumes of data through FE analysis, with limited capability of effective collection and processing to optimise manufacturing processes. Two essential sets of information are crucial in metal forming processes, namely the evolutionary thermo-mechanical behaviour and geometric features. An effective understanding and prediction of these characteristics enables an optimised processing window to be developed to minimise material waste and improve process and part design. Due to the information-absent data being contained in the data source, the development of a data processing technique, e.g. classification algorithm, able to extract insightful information from these data becomes a critical challenge to digitally characterise the sheet metal forming processes by employing numerical algorithms.



Figure 1.2: Strategy of test guidance generated based on data analysis

In addition, research in metal forming processes has traditionally followed the convention of validating hypotheses with repeatable experimental trials. The accuracy of FE analysis is significantly dependent on the material characterisation, as well as definitions of boundary conditions, such /hlas coefficient of friction (COF) and interfacial heat transfer coefficient (IHTC). COF significantly affects the variation in stress distributions, lubricating conditions, die surface characteristics and homogeneous deformation across the contact area between forming tools and workpiece. IHTC is also a parameter of vital importance to determine the cooling rate and the post-form strength when optimising the forming condition, especially for processes at elevated temperature. However, the reliable characterisation of boundary conditions remains challenging, which can be partly explained by the fact that the actual boundary conditions in metal forming processes are not well understood. Throughout the tool surfaces, the contact/sliding conditions vary over the duration of forming process thus presenting significant challenges in modelling this behaviour using conventional mathematical models. The workpiece-tool interfaces at different regions, such as the blank-holding area, die radius and die cavity areas, also have different friction coefficients and wear conditions. Therefore, there is a clear need for analyses of the evolution of these boundary conditions to establish a relationship between fundamental tests and metal forming processes to improve the effectiveness of experimental testing and modelling. Fig.1.2 shows the general concept and motivation of generating a data-driven test guidance.

The following objectives were conducted to achieve the aim of this work:

- Collect and establish a standard database of experimentally verified finite element simulations for a fast light alloy stamping technique.

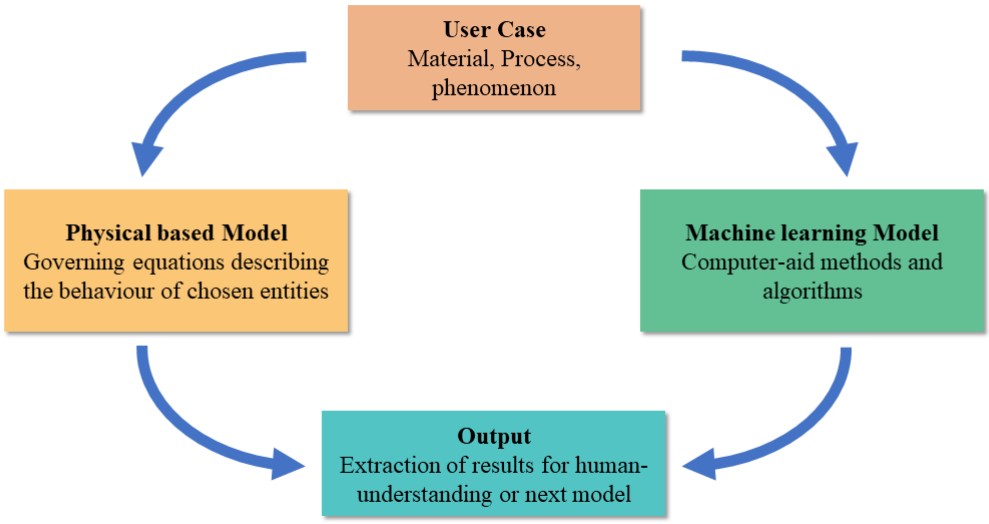


Figure 1.3: Methodology for extracting of insightful information from information-absent FEA data

- Explore and develop a data processing framework to recognise the geometric information from finite element analysis of this metal forming process by using a numerical approach and a physical-based algorithm (see Fig.1.3).
- Develop digital characterisation to reveal the boundary condition evolution of metal forming process to enable a data-driven test approach.

1.3 Thesis structure

The structure of the thesis and the interconnections between the chapters of this work are shown in Fig.1.4, in which the four different colours indicate the main four contributions of this thesis. **Chapter 2** firstly reviews the literature related to this work. **Chapter 3** describes the data collection, and how they were pre-processed, including data clearing, weighting, labelling and normalising process. **Chapter 4** describes the development of the machine learning classification model, where a logistic regression classifier, an feedforward neural network (FFNN)

classifier, and a deep recurrent neural network (RNN) classifier were constructed and compared. **Chapter 5** introduces the development of physically-based models, where a strain-based model, a temperature-based model and a thermo-mechanical evolutionary algorithm framework were established. **Chapter 6** describes the development of data visualisation method for illustrating the boundary condition characterisation during the metal forming process towards data-driven COF and IHTC testing schemes. **Chapter 7** briefly introduces the feasibility study of experiment work by utilising the data-driven testing scheme.

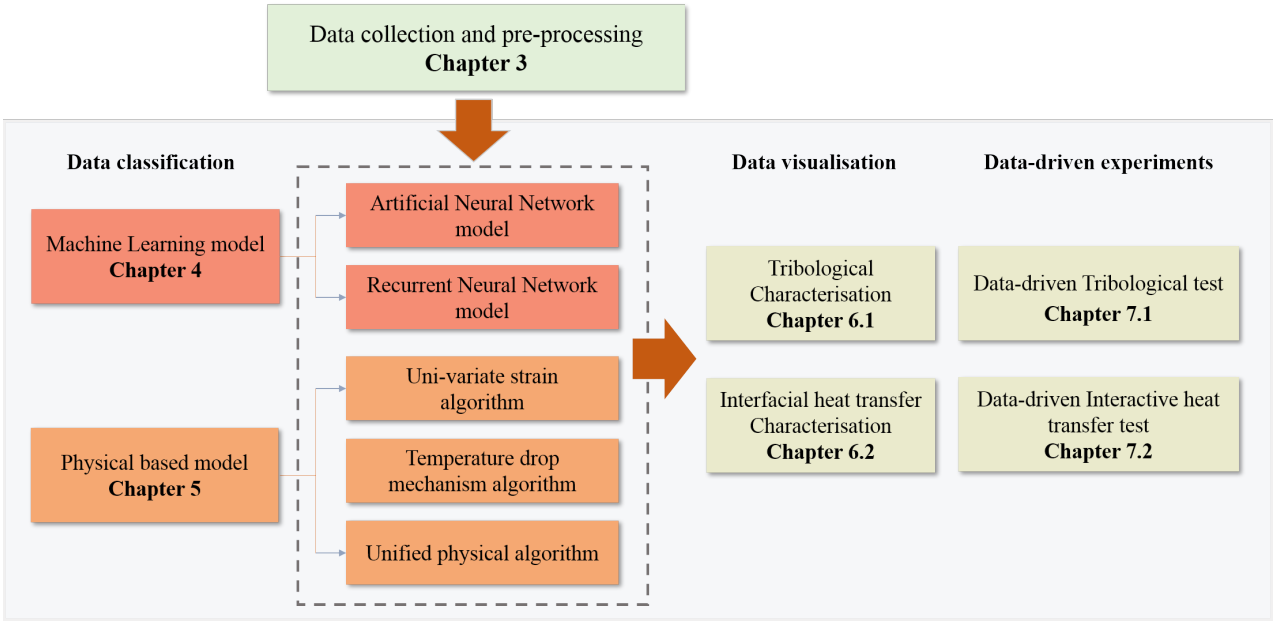


Figure 1.4: Schematic for the key contributions of the thesis

Chapter 2

Literature review

This chapter aims to provide an overview on knowledge and information required in this work. The schematic for main contents covered in this section are as shown in Fig.2.1. In order to establish a data processing framework, it requires understanding on the sheet metal forming process as well as data processing methods. This chapter firstly reviewed some newly developed sheet metal forming process whose finite element data was used in this work. The focus has been placed up on on the stamping technique of lightweight sheet material at elevated temperature, as well as and their thermo-mechanical behaviours. The well-established data processing techniques were then reviewed, including different machine learning classification methods. In order to provide a data-driven testing scheme, the traditional boundary condition characterisation method, including friction test and IHTC tests were reviewed.

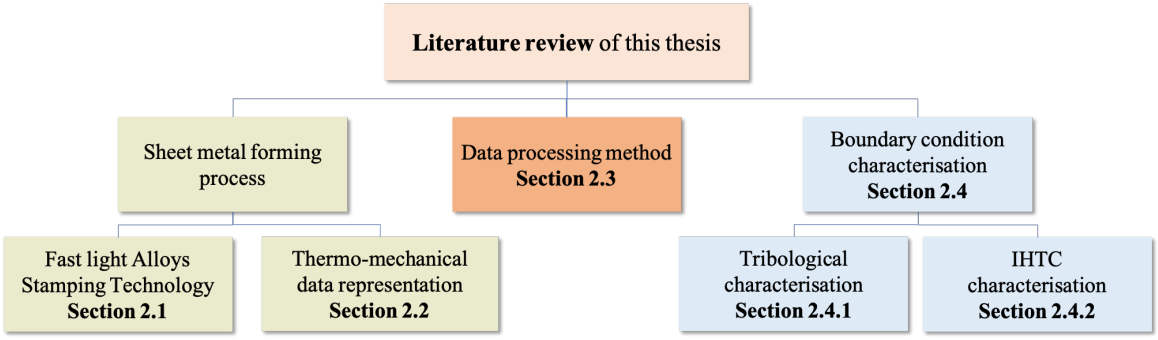


Figure 2.1: Schematic for main contents covered in literature review

2.1 Lightweight sheet metal forming process

The concerns of environmental problems has driven manufacturing industries to saving energy by reducing the weights of the products, especially in the automotive industry (Mallick, 2010). One efficient approach is to replace the traditional steel by lightweight materials, such as ultra-high strength steel, aluminium alloys, titanium alloys or composites (Froes, 1994). In addition, forming these materials in an efficient process is also a big challenge. Sheet metal forming refers to the process where a sheet blank is plastically deformed between tools to obtain the desired configuration in a very short time, and a schematic is shown in Fig.2.2. This forming technique has the advantages of high efficiency and energy saving in mass production, and the final products exhibit high strength-to-weight ratio and metallurgical properties. Due to the ever-increasing costs, sheet metal forming techniques are designed and developed with maximum energy efficiency and minimum forming cycle time. Several novel sheet metal forming processes were recently proposed, invented and patented by Imperial College London Metal Forming group (Wang and Kopec 2019; 2018).

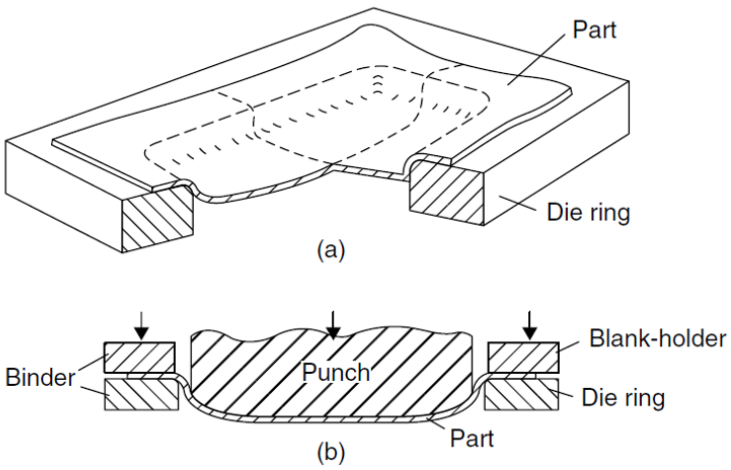


Figure 2.2: (a) A typical part formed in a stamping or draw die showing the die ring, but not including the punch or blankholder, (b) section of tooling in a draw die showing the punch and Binder (Hu et al., 2002)

2.1.1 Fast Light Alloys Stamping Technology (FAST) of aluminium alloy

A novel Fast light Alloys Stamping Technology (FAST) is proposed to manufacture structural panel components, which enables over 90% cycle time reduction comparing to conventional hot stamping process (Zhang et al., 2019). The concept of FAST is to deform the component in a very short time and obtain a high strength by using the proper raw material with desired microstructure and chemical composition. The schematic of conventional hot stamping process and FAST are shown in Fig. 2.3 as blue line and blank line, respectively. The blank is firstly heated to the target temperature at an ultra-fast rate, and formed and quenched in the cold dies immediately. To form the common 6 series aluminium alloys, the strength of the component is mainly contributed by the post-form precipitation hardening (Shercliff and Ashby, 1990), and the well accepted precipitation response mechanism has been studied by Milkerit et al. (2012), who found that the post-form precipitation hardening is dependent on the initial microstructure and the chemical composition of the raw material.

Therefore, by controlling the microstructure of the raw material, the paint bake cycle is sufficient for the final component to reach a high strength. Compared to the conventional stamping technique of aluminium alloys, the solute heat treatment (SHT) and artificial ageing can be eliminated. The solute heat treatment refers to holding the sheet metal at a suitable temperature until a solid solution condition, and cooling rapidly enough to hold these constituents in solution (Garrett et al., 2005). The artificial ageing refers to holding the sheet metal at a elevated temperature to produce optimum size, distribution of microstructure (Dahle et al., 2001). Removing these processes results in a considerable increase in mass production efficiency and decrease in energy consumption, but the challenge also arises to predict the post-form strength after FAST and following paint-bake cycle. Zhang et al. (2019) proposed a physical-based model enabling a quantitative prediction and control for the FAST products.

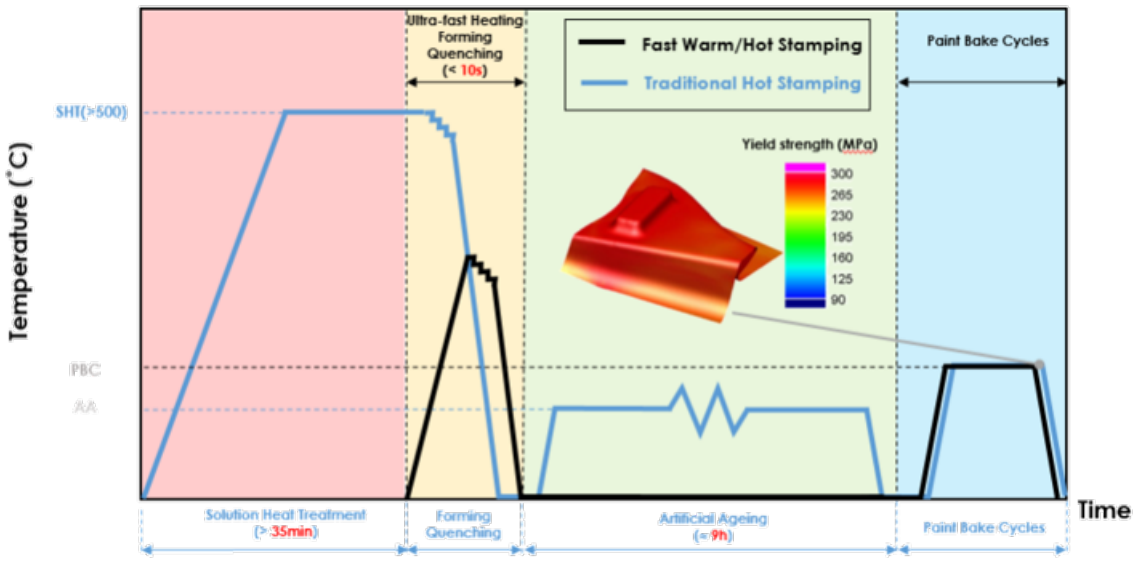


Figure 2.3: Schematic for forming 6 series aluminium alloy using Fast light Alloys Stamping Technology (FAST) and conventional hot stamping technique (Zhang et al., 2019)

2.1.2 Fast Warm Stamping (FWS) process of steel

The Fast Warm Stamping (FWS) process is the process where a steel blank is heated up at ultra-fast rate to an appropriate temperature, usually at 350 - 450°C, whilst minimising the changes in microstructure which determines the post-form strength. Using the proposed method, a similar strength of as-received material can be retained in the formed part while the cycle time and energy costs are reduced. The feasibility of the FWS technology was initially studied by Sun (2020).

Fig. 2.4 indicates the schematic diagram and microstructural evolution of the FWS process of martensite steel and conventional hot/warm stamping process of ferrite steel. The MS1180 blank with desired mechanical properties and microstructures is heated rapidly at an ultra-fast heating rate to an appropriate temperature (dependent on the complexity of the part geometry), where the formability of the blank is sufficient to form the part. This temperature is below a critical temperature which could lead to a substantial change to the microstructure of the metal being heated. Once the blank reached the target temperature, it is subsequently stamped and quenched immediately. High forming speed is applied to avoid excessive heat loss so that the blank temperature maintains its temperature. The FWS process reduces the heating time significantly and eliminates the austenitization process prior to stamping, so that the total cycle

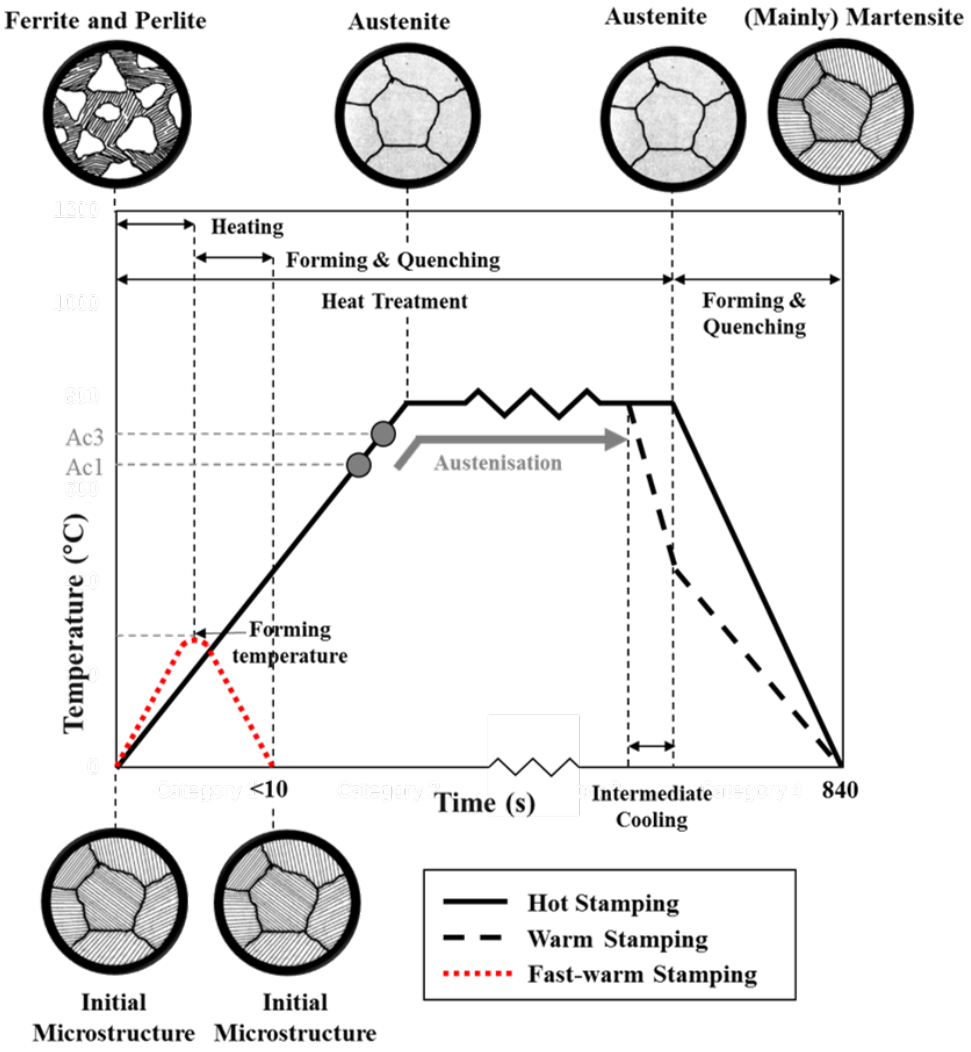


Figure 2.4: Schematic for forming high strength steel using Fast-Warm Stamping and conventional hot/warm stamping processes (Sun et al., 2020)

time for manufacturing the MS1180 parts is within 10 seconds. The ultra-fast heating rate would avoid undesirable changes to the initial microstructures of the sheet metal so that the nearly full mechanical strength of the pre-form condition can maintained. Additionally, the energy consumption/cost of this forming technology is reduced by maintaining forming temperature at the minimum level, whilst also ensuring sufficient formability to form the components.

2.1.3 Hot stamping process for titanium alloy

In the aerospace sector, titanium alloys are widely used in a high strength structural components (Peters et al., 2003). However, it is a very high energy and time consumption process to

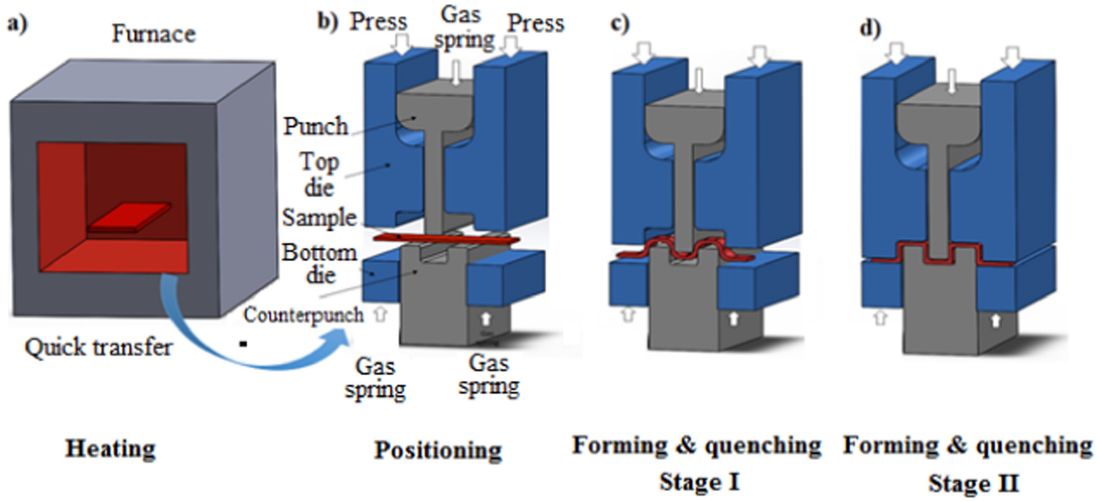


Figure 2.5: Schematic of the hot stamping process of titanium alloy (a) during heating of the sample, (b)at the positioning stage, (c) during forming and (d)at the final stage. (Kopec, 2018)

form titanium alloys into products with complex geometry. Kopec (2018) proposed an innovative forming technology to shape Ti6Al4V titanium alloy, using the similar idea, where the hot blank was formed between low temperature forming tools. Traditional hot stamping processes have mainly focused on aluminium alloys and ultra-high strength steels, for the automotive industry. Kopec et al. (2018) conduct a number of studies on the hot stamping of titanium alloys under varying temperatures as well as the microstrucutrue evolution. As shown in Fig. 2.5, the hot stamping of titanium alloy consists three states: heating, transferring, and simultaneously forming and quenching. Titanium parts were initially heated up to 850°C and then soaked for about 180s utill a stable temperature was realised. It was then transferred to forming tool where the temperature keeps decrease, and formed at about 700°C in cold dies. In the following quenching process. the temperature rapidly dropped to approximately 350°C and then gradually decreased to room temperature. Hot stamping tests that the qualified part can be formed between 750°C and 850°C. The microstructure experiences recovery, phase transformation and recrystallization during deformation (Li et al., 2019).

2.2 Data representation in metal forming process

In order to develop a reliable data processing technique for sheet metal forming processes, it is essential to understand the data being processed, i.e. the thermo-mechanical behaviour during the forming process. Physical phenomena governing sheet metal forming and the controlled process variables were reviewed in this section. The most related variables have been listed in Table 2.1 (Altan et al., 1983), including sheet material, deformation zone, tooling and equipment/product. The data classification part is mostly related to sheet material, deformation zone and equipment/product, while the tooling effect is involved in the boundary condition characterisation.

Table 2.1: Significant variables in sheet metal forming

Sheet material or blank	**Deformation Zone**
Flow stress	Deformation mechanics
Thermal/physical properties	Metal flow, velocities, strain, strain rate
Initial conditions	Stresses and contact pressures
Blank size, location and thickness	Temperatures
Tooling	**Equipment and product**
Tool geometry and forces	Speed/production rate
Tool temperature	Product geometry
Lubricant used	Mechanical properties

2.2.1 Flow stress, strain and strain rate

In analysing and optimising a sheet metal forming process for a given material, the important variables include the blank properties (e.g. composition, temperature, deformation history, and pre-strain), the flow stress of the blank material for various strain values, and the surface and boundary conditions. Among them, the flow stress is the most important variable. A metal forming process is dominated by two physical mechanisms; strain hardening, also known as work hardening, and strain-rate hardening. Due to the movement and accumulation of dislocations within the crystal structure of a metallic material, the flow stress increases with increasing strain, demonstrating strengthening behaviour of the material at a given temperature (Avitzur, 1968). Various temperatures are employed in different forming technology. For instance, cold forming of simple-shaped components is conducted at room temperature, hot stamping of

complex-shaped components is conducted at the solution heat treatment (SHT) temperature of the material and forming of multi-phases materials is conducted at their phase-transformation temperature. It was found that the flow stress decreases with increasing temperature because of more dislocations being recovered at a higher temperature (Hansen, 1977). In addition to sthe train hardening mechanism, strain-rate hardening has a significant effect on the plastic deformation of the material as well. The flow stress of a material increases with increasing strain rate due to the fact that the annealing has less time to occur and thus the density of dislocations is smaller at a higher strain rate (Lin, 2015). This is typical behaviour of viscoplastic material formed at different strain rates.

These properties or parameters are input into the FE software in the form of discrete data known as 'look-up tables', a set of constitutive equations or a single value. The reliable FE analysis depends on the accurate determination of these properties. The flow curves (Eq. 2.2) for sheet materials are usually determined based on load versus elongation data obtained from tensile tests. At room temperature, the stress-strain relationship can be approximated by the power-law equation:

$$\bar{\sigma} = K\bar{\varepsilon}^{n} \tag{2.1}$$

here K is known as the strength coefficient and the n as the strain hardening exponent. However, the flow stress of many metals, such as aluminium alloy, show a strong dependence on both strain rate and temperature at hot working temperatures. A set of unified visco-plastic constitutive equations have been proposed to model these phenomena by Prof. Lin (Lin, 2015),and the flow stress, $\bar{\sigma}$ is a function of equivalent strain, $\bar{\varepsilon}$, equivalent strain rate, $\dot{\bar{\varepsilon}}$ and temperature T:

$$\bar{\sigma} = f(\bar{\varepsilon}, \dot{\bar{\varepsilon}}, T) \tag{2.2}$$

These thermo-mechanical features of the sheet blank during the deformation can be found in relevant literature. Strain rates in the range of $10^{-5} - 10^{-2}\mathrm{s}^{-1}$ are typically used in the superplastic forming technique (Horita et al., 2000; Watanabe et al., 1999), whereas 10^{-1}-1 s^{-1} are used in steel sheet metal forming (Turetta et al., 2006). Hot stamping of aluminium alloys typically involves strain rates in the range of $10^{-1} - 10\mathrm{s}^{-1}$. Large variations in temperature

ranges also exist across different applications, such as in hot stamping of aluminium alloys and steel, where a range of 150 - 525°C or 150 - 1000°C are used respectively (Li and Ghosh, 2004).

2.2.2 Stress state, Lode parameter and stress triaxiality

The stress state is also a very important indicator during the forming process. The sheet metal forming process is a constant volume deformation process, which contains three types of plastic deformation: elongation, plane strain, and compression, respectively. The specific deformation type in a complex forming process is determined by the stress state, which is usually described by six independent stress components on Cartesian coordinate planes. However the characteristic quantities such as the stress tensor invariant, major/minor stress, Lode coefficient and stress triaxiality at this point will not change with the change of the coordinate system. Therefore, the characteristic value of stress tensor plays an important role in describing the routine of plastic deformation (He et al., 2004*a*). The Lode coefficient and stress triaxiality can reflect the relative magnitude of the intermediate principal stress and has a certain corresponding relationship with the strain type. Therefore, it can be used to judge the strain type and the complexity of the deformation (He et al., 2004*b*; Hu et al., 2004). According to the relationship between stress state and Lode coefficient. Yuan 2008 determined the ratio of strain increment by Lode coefficient, and then the idea of plastic deformation type is established. The quantitative relationship between stress state, Lode coefficient and plastic deformation type is established. By displaying the Lode coefficient diagram in the post-processing program of the finite element numerical simulation software, the strain type of the whole field of the workpiece can be given.

In Fig. 2.6, x-axis indicates the Lode parameter, μ_σ, which represents the type of deformation, $\mu_\sigma > 0$ is a compressive strain, $\mu_\sigma < 0$ is a tensile strain, $\mu_\sigma = 0$ is plane strain condition, and the y-axis indicates stress triaxiality, which represents the stress state, 2/3>j>1/3 is the bi-tensile condition, $\sigma_1 > \sigma_2 > \sigma_3 > 0$, $1/3 > j > -1/3$ is in tensile-compressive condition, $\sigma_1 > \sigma_1 = 0 > \sigma_3$, and when - 1/3>j>-2/3 is the bi-compressive condition, $0 = \sigma_1 > \sigma_2 > \sigma_3$. The lode parameter and the stress triaxiality is given by:

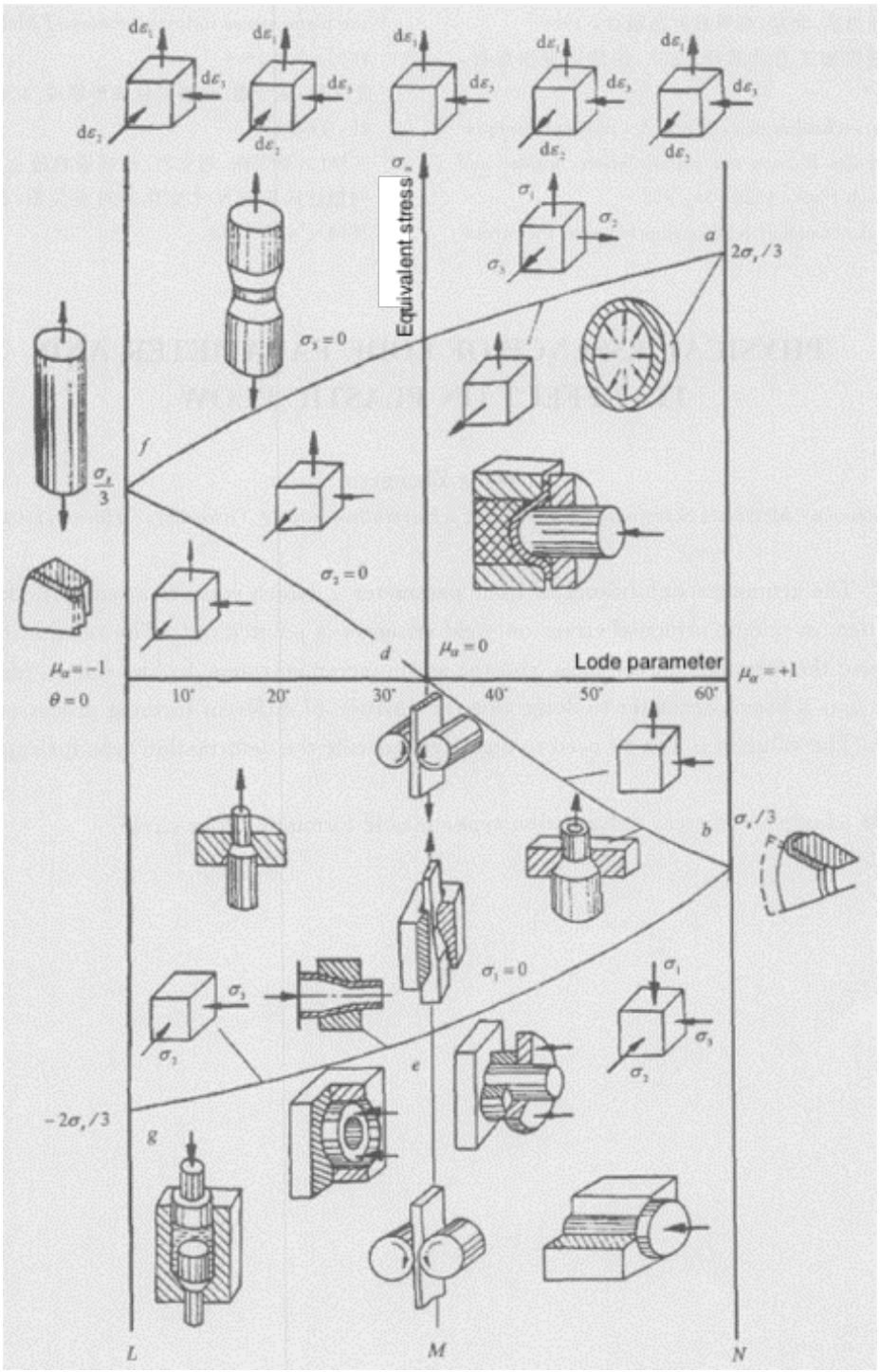


Figure 2.6: The stress/strain distribution on the Von Mises plane development, where x-axis is the Lode parameter and y-axis is the equivalent stress (Yuan, 2008)

$$\mu_\sigma = \frac{2\sigma_2 - (\sigma_1 - \sigma_3)}{\sigma_1 - \sigma_3}, -1 < \mu_\sigma < 1 \tag{2.3}$$

$$j = \frac{\sigma_1 + \sigma_2 + \sigma_3}{3\sigma_y}, -\frac{2}{3} < j < \frac{2}{3} \tag{2.4}$$

where σ_y is the von mises yield strength. In the Figure. 2.6, the $\sigma_3 = 0$, $\sigma_2 = 0$ and $\sigma_1 = 0$, the top, middle and bottom curve indicates the bi-tensile plane, tensile-compression plane and bi-compression plane, respectively.

2.2.3 Product geometry

The behaviour of plastic deformation and quenching of a material is different depending on its geometric features, which can be approximately divided into three zones, namely blank holding, bottom and sidewall. The blank holding area is generally subjected to a radial tensile stress and a circumferential compressive stress, resulting in a relatively small strain (Altan et al., 1983). Meanwhile, this zone has a good quenching efficiency due to the compression generated by a press holding force. Although subjected to different tensile stresses along both radial and circumferential directions, the bottom zone also has minor strain and thinning due to restricted plastic deformation. Similar to that on the blank holding area, the quenching efficiency on the bottom zone is high as well due to the sufficient contact between the forming tools. In contrast, the sidewall zone withstands a high tensile stress and thus strain. However, its quenching rate is relatively low due to the designed die clearance and the consequent insufficient contact between the forming tools. According to the behaviour of plastic deformation and quenching on different zones, typical processing parameters are applied in the metal forming processes. For instance, a material is partially heated with a higher temperature on the bottom and sidewall zones to increase its ductility and a lower temperature on the blank holding area to maintain a high strength. Meanwhile, the formed material can be partially quenched to achieve the desired microstructure and/or phase formation on different zones. A small contact pressure (holding force) is applied on the blank holding area to decrease its quenching rate and thus maintain

its high drawability, while a large contact pressure is applied on the bottom and sidewalls zones to increase its quenching rate (Avitzur, 1968). Additionally, lubricants and coatings with typical properties, e.g. viscosity, heating point and thermal conductivity, are applied on different geometric zones to meet the desired requirements on the friction and heat transfer, etc. Therefore, the information of geometric feature is demanded to divide other information accordingly, which is used to guide the metal forming processes based on different geometric zones.

2.3 Classification using machine learning technique

Basic principles of machine learning are introduced in this section. The goal of machine learning is building computer programs that can automatically improve themselves in performing certain tasks from experience (data) (Mitchell, 1997).The essence of the (supervised) machine learning algorithms is to learn a function $f : x \rightarrow y$, where x is the training data usually with high dimension information, and y is corresponding output (see figure Fig. 2.7)

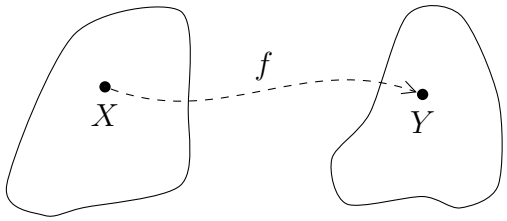


Figure 2.7: Illustration of machine learning model, Ng (2018)

2.3.1 Single neuron neural network (SNNN) and logsitic regression

Neural network is a biologically inspired machine learning mode. In this section, single neuron neural network, the simplest neural network, is introduced. The the mathematical form of the model and the mechanism of the learning process is introduced in this section. Following the foundational papers (Carpenter, 2008; Graves, 2012; Socher et al., 2014), a typical SNNN structure is given by:

$$f_w(\boldsymbol{x}) = \sum_{i=1}^{i=n} w_i x_i + b = \boldsymbol{w}^T \boldsymbol{x} + b \tag{2.5}$$

where the feature is represented as $\boldsymbol{x}$ and the predicted output is y. Both w and b are training parameters, presenting the weights and the bias. Thus, a problem with any dimensional input feature and resultant model can be generalised as a linear regression model ($\boldsymbol{w}$ is a column array of dimension n-by-1 and $\boldsymbol{w}^T = [w_1, ..., w_n]$). Different from regression, a classification problem refers to the problem with discrete answers. where a non-linear function is thus required. Logistic function is the mostly used in solving classification problem (Kleinbaum et al., 2002), so that the SNNN model is also called logistic regression model.

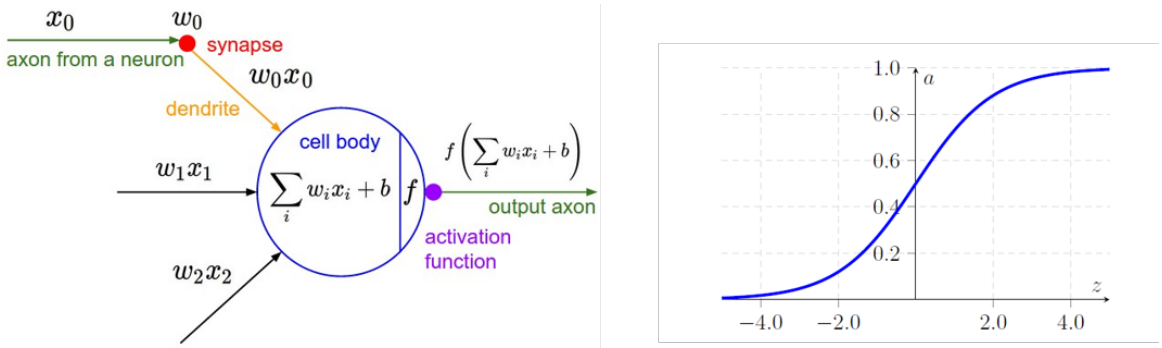


Figure 2.8: Single Neuron Neural Network (left) and logistic function (right)[1]

The single neural network graph and the logistic function is illustrated in Fig.2.8. The circle represents neuron including two mathematical operations: (1) affine transformation of the weighted inputs $\sum_i w_i x_i + b$ (2) an logistic activation $\sigma\left(\sum_i w_i x_i + b\right)$. The arrows represent the connections between neurons, where the input feature is multiplied by the weights i.e., $w_n x_n$. Detailed mathematical derivation is illustrated in Casella and Berger (2002).

2.3.1.1 Loss/Error Function

This section introduced the training process of a neural network. The performance of the function is determined by log likelihood function (Gourieroux et al., 1993). For binary classification problem, the log likelihood function is given by:

[1] Image source: http://cs231n.github.io/neural-networks-1/

$$l(\boldsymbol{w}, b) = \sum_{i=1}^{m} \left(y^{(i)} \log a^{(i)} + (1 - y^{(i)}) \log(1 - a^{(i)}) \right) \tag{2.6}$$

where the i is the index of training set, $a^{(i)}$ and $y^{(i)}$ are the predicted and the actual results for input training set $\boldsymbol{x}^{(i)}$). The negative of log likelihood is used as the cost function, $J(\boldsymbol{w}, b)$.

$$J(\boldsymbol{w}, b) = \frac{l(\boldsymbol{w}, b)}{m} = -\frac{1}{m} \sum_{i=1}^{m} \left(y^{(i)} \log a^{(i)} + (1 - y^{(i)}) \log(1 - a^{(i)}) \right) \tag{2.7}$$

where m is the size of training set. The result is optimised by minimising the cost function of the total data set. In order to improve the learning efficiency, the costs are calculated from a small mini-batch of training examples $J_{mb}(\boldsymbol{w}, b)$, without going through the whole training set, which is given by:

$$J_{mb}(\boldsymbol{w}, b) = -\frac{1}{mb} \sum_{i=1}^{mb} \left(y^{(i)} \log a^{(i)} + (1 - y^{(i)}) \log(1 - a^{(i)}) \right) \tag{2.8}$$

where mb is the size of the mini-batch. The effect of mini-batch will be discussed in Chapter 4.

2.3.1.2 Gradient Descent

Gradient descent is the optimisation method to minimise the cost function in neural network. It is rearranged from first order Taylor expansion (Burges et al., 2005):

$$w_n := w_n - \alpha \frac{\partial}{\partial w_n} J(\boldsymbol{w}, b) \tag{2.9}$$

$$b := b - \alpha \frac{\partial}{\partial b} J(\boldsymbol{w}, b) \tag{2.10}$$

In the optimisation process, the parameters are updated with the new value in each iteration. α is the learning rate, which is applied to damp out the step of each update to achieve numerical convergence. The effect of learning rate will be discussed in Chapter 4.

2.3.2 Feedforward neural network (FFNN)

In this section, a feedforward neural network is introduced. It consists of a set of neurons (SNNN), commonly referred to as nodes or units here. Fig. 2.9 shows a 3-layer neural network. For any neural networks, the information, $\boldsymbol{x}$, propagates from the input layer (LHS) to the ouput layer (RHS) $\hat{\boldsymbol{y}}$. The number of hidden layers in between are dependent on the complexity of the model. The effect of layers will be discussed in Chapter 4.

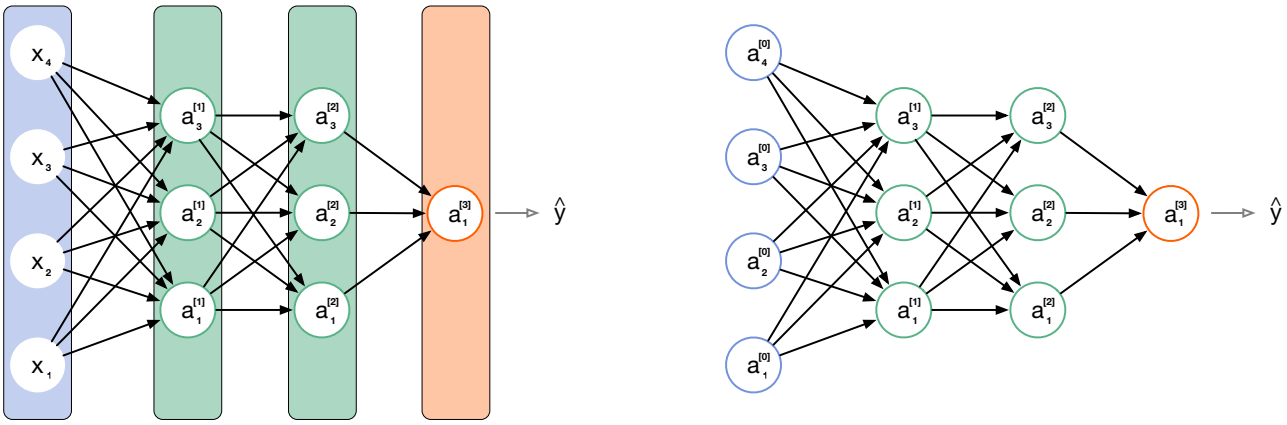


Figure 2.9: 3 Layer Neural Network (the two diagrams represent identical neural network)

2.3.3 Recurrent neural network (RNN)

A recurrent neural network are feedforward neural networks with the added notion of time to the model. In recent years, improvement on RNN system, such as long short-term memory (LSTM) (Hochreiter and Schmidhuber, 1997) architectures have demonstrated ground-breaking performance on leaning task with the sequential data, such as natural language process (Papineni et al., 2002), handwriting recognition (Graves, 2012) and music classification (Choi et al., 2017).

2.4 Characterisation of boundary condition for sheet metal forming processes

During the last two decades, computer-aided Finite Element (FE) analysis has been developed in the sheet metal forming industry for process optimisation to reduce the costs involved in the sheet metal forming industry for process optimisation to reduce the costs involved in the trial-and-error prototyping. The accuracy of FE simulations is the most significant requirement, which is influenced by the flow stress data and the assignment of boundary conditions, such as coefficient of friction (COF) and interfacial heat transfer coefficient (IHTC). Research in these subjects has followed the convention of validating hypotheses with repeatable experimental trials. This section introduced the COF and IHTC characterisation in the literature.

2.4.1 Characterisation of coefficient of friction (COF)

A tribological characterisation in sheet metal forming process has been comprehensively reviewed by Dohda (2015), Bay (2008) and Podgornik (2004). Bay (2008) concludes two main classes of tribological testing method in sheet metal forming process:

- process tests
- simplified tests

Process tests are referring tests through typical metal forming operations using the same process kinematics, while simplified tests are those that replicate the contact conditions at the workpiece-tool interface with the attempt to investigate the tribological behaviour in a controlled way. Process tests can always represent the real forming conditions, however, through which the scientific investigations sometimes are difficult in practice. One of the reasons is the high cost involved in the tool usage. The measurement of friction coefficient during the process, and the followed in-depth topography analysis are also difficult to conduct due to the complex geometry and large size of tools and workpieces. As a result, simplified test have been a more preferred approach in the research of tribological behaviour in sheet metal forming processes.

Based on the literature, it was found that although various simplified testing methods has been designed to simulate the contact condition at tool-workpiece interface during the sheet metal forming process, the testing conditions or experimental parameters are still experience oriented, which results in that simplified tests can only provide a limited or improper testing window for real metal forming process. Fig. 2.10 illustrates the overview of the most commonly used

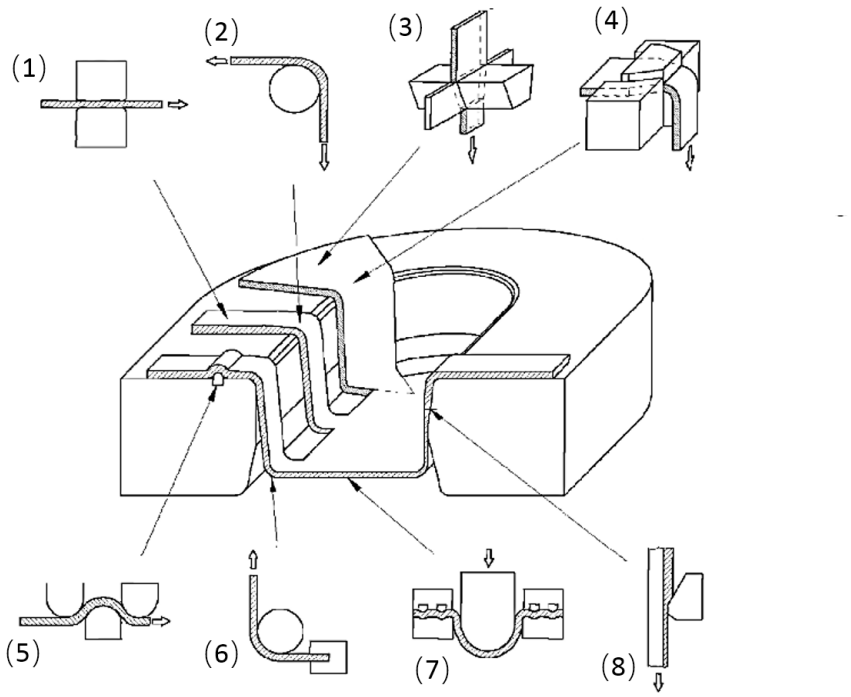


Figure 2.10: Schematic illustration of simplified tests for sheet meta forming Bay et al. (2008), including (1) Strip drawing with flat dies, (2) Bending under tension, (3) Drawing with tangential compression, (4) Bending with tangential compression, (5) Draw bead testing, (6) Strip -tension testing, (7) Hemispherical stretching, (8) Strip reduction testing
(Bay et al., 2008)

simplified tests for sheet metal forming process which is developed by Bay (2008). The blank holding area with different conditions can be represented by three different simplified tests, strip drawing with a flat die in Fig. 2.10 (1), drawing with tangential compression test in Fig. 2.10 (3) and draw bead testing in Fig. 2.10(5). Yanadiga Yanagida et al. (2010) conducted a hot flat strip drawing test to examine the friction coefficient in high temperature metal forming at different drawing speeds, drawing pressures and temperatures, which provided a more realistic representation of the contact condition at the blank holding region of a hot stamping process.

Masters 2013 also conducted the strip drawing test for pre-stretch high strength aluminium alloys. Bending under tension in Fig. 2.10 (4) reproduces the die curvature condition, and bending with tangential compression (4) in Fig. 2.10 reproduces the combined conditions in the blank holding and on the die curvature. Gali (2013) conducted a bending under tension test, where a strain was applied to provide indirect sliding. Strip reduction testing in Fig. 2.10 (8) represents ironing in a conical die, while strip - tension testing in Fig. 2.10 (6) and hemispherical stretching in Fig. 2.10 (7) simulates stretching over the punch radius of curvature and under the punch nose, respectively. In addition, to evaluate galling behaviour during metal forming processes, a load-scanning test was developed Heinrichs and Jacobson (2009, 2010), where the load was continually increased to determine the critical sliding length and contact pressure at which galling initiates.

Another typical simplified test is pin-on-disc test (Chowdhury et al., 2011; Wang et al., 2010; Ghiotti et al., 2013), The simplified friction test schemes and corresponding testing conditions are summarised and listed in Table 2.2. It is found constant testing conditions were used in most the previously research. However, in the acutal forming condition, the contact pressure, sliding distance and sliding speed vary spatially and historically (Pereira et al., 2012).

Table 2.2: Contact conditions of different tribological testing methods in sheet metal forming

Test Types	Authors	Material Pairs	Temp (°C)	Cont. pressure	Sliding velocity	Sliding distance
Pin-on-disc	So(1996)	Die steel/ AA6082	Room	2.2 MPa	1 m/s 2 m/s 3 m/s	1800 m 3600 m 3600 m
	Chowhury(2011)	stainless steel/ Al alloy	Room	10 N 15 N 20 N	500 rpm 1000 rpm 1500 rpm 2000 rpm 2500 rpm	2500 cycles 5000 cycles 7500 cycles 10000 cycles 12500 cycles
	Ghiotti(2013)	Tool steel/ Boron steel	800	7 MPa	15 mm/s	75 mm per cycle
	(Ghiotti2016)	HTCS/ Usibor1500P	600(disc)/150(pin) 700(disc)/120(pin) 800(disc)/90(pin)	10 MPa	15 mm/s	75 mm per cycle
	Wang(2010)	H11 steel/ AA7075	350 to 500 each 50	90 MPa 110 MPa 140 MPa 200 MPa	2 m/s	18.8 - 188 mm
Flat-on-flat	Hanna(2009)	H11 steel/ AA5083	450	50 N	16.5 mm/s	15 mm per pass
Strip drawing	Yanagida(2010)	SPHC steel/ SKD61	100 to 800 each 100	16MPa 32 MPa 45 MPa	5 mm/s 10mm/s 20mm/s	500 mm
	Ghiotti(2011ïijL	Coated tool steel/ strainless steel	Room	1 MPa 3 MPa 5MPa 25MPa	1 mm/s 5mm/s 10mm/s 50 mm/s	100 mm
bending-under -tension	Gali(2013ïijL	P20 steel/ AA5083	25-450 each 50 or 100	0.22 N	strain rate $4x10^{-2}s^{-1}$	14.3-32.5 μm

2.4.2 Characterisation of interfacial heat transfer coefficient (IHTC)

Researchers haven made great efforts to investigate the value of interfacial heat transfer coefficient (IHTC) during metal forming process, such as with aluminium alloy (Ilkhchy et al., 2012), boron steel (Caron et al., 2014) and titanium alloy (Bai et al., 2012). At higher contact pressure condition, where the real contact area between the contacting solids is larger, lead to an increase in IHTC values. Liu (2017) determined the IHTC values for different tool materials, and found that higher thermal conductivity of tool material resulted in an increase in the IHTC. Tang 2015 investigated the effect of surface roughness on IHTC, and proved that a higher surface roughness led to a decrease in the IHTC values.

Constant contact pressure were used in most the previous research. However, the contact pressure varies in actual hot stamping processes, especially for complex-shaped components (Pereira et al., 2010). The change in contact condition leads to variable IHTC value during the

process. The research on IHTC under variable contact pressure conditions is still limited.

Chapter 3

Data Collection and pre-processing

3.1 Introduction

Regardless of the specific problem to be investigated, a prerequisite in this work is the existence of past finite element simulation data that has been experimentally verified. Thus, an effort has to be put in place upfront for the creation of clean, curated and reliable data related to the problem. An example data set should contain a verity of materials that deform at different forming conditions with the relevant output and computed evolutionary thermo-mechanical properties of those materials during the process (see Fig. 3.1a). Within the data processing framework, the finite element is referred to as 'input' and the the property of interest is referred to as the 'target' or 'output'. The learning problem (Fig.3.1b) is defined as follows: Given a element - property data set, to estimate the property for a new element not in the original data set.

The data-driven strategy includes two steps. The first step is to represent numerically the various elements in the data set. Each input would then have been reduced to a series of numbers i.e fingerprints (see Fig. 3.1b), which is a step of vital importance, requiring significant knowledge of the forming technique. The second step is to establish a relationship between the fingerprint and the target element properties. The schematic of fingerprinting and modelling are both illustrated in Fig. 3.1. Several algorithms, ranging from elementary (logistic regression

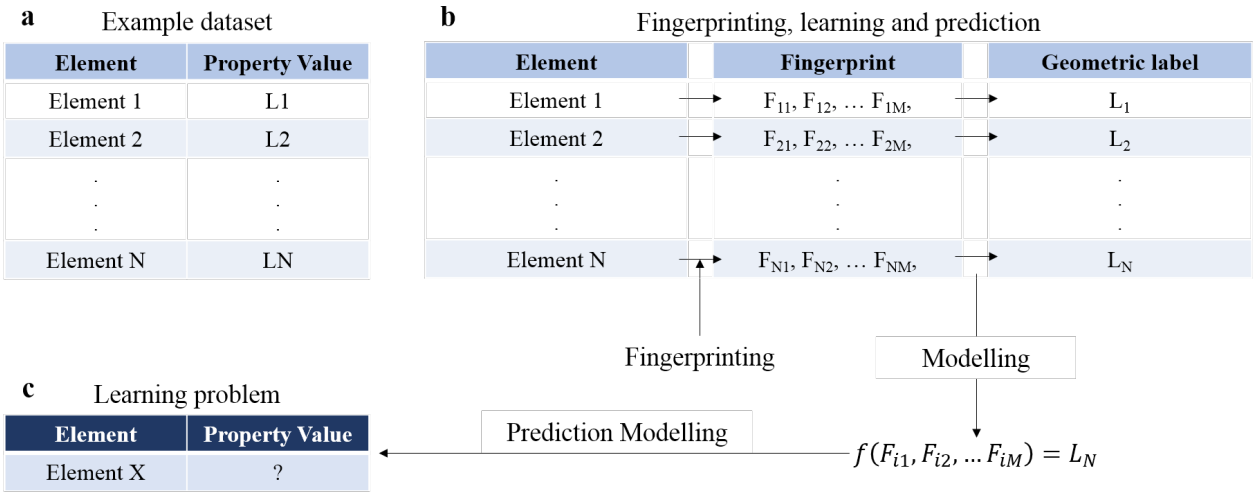


Figure 3.1: Key elements of machine learning based data classification technique. **a** Schematic view of an example data set, **b** creation of a prediction model via the fingerprinting and learning steps. N and M are the number of training examples and the number of fingerprint components, and **c** problem solving by prediction model

classifier) to highly sophisticated (artificial neural network classifier and deep recurrent neural network classifier) are available to establish this prediction modelling, a physics-based model, to establish the quantitative relationship between element and corresponding thermo-mechanical behaviour, is also one of the options.

3.2 Data collection

The data set was collected from two main source: in-house data and online data. The in-house data includes the FE simulation results from Imperial College London and the industrial partner including Schuler and PAB. The online data are collected from a cloud-based online platform SmartForming®, which has the ability to remotely perform the multi-objective FEA to simulate not only the deformation of the materials, but also the formability, tool life, tool design and post-form strength of the materials. In the current internal test, the remote users from over 20 worldwide industries and institutes generated the data set containing 146,000,000 data points, including the information of the material characterisation, processing parameters and geometric features. All the finite elements simulation results have been experimentally validated through the strain/thickness distribution, and the temperature evolution.

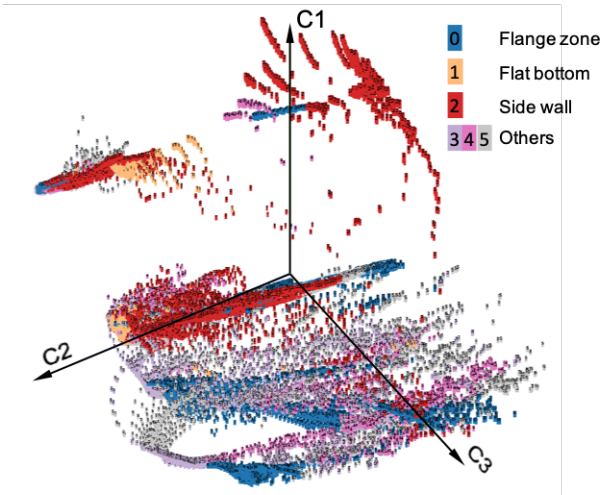


Figure 3.2: Through a preliminary principal component analysis, the dimensionality (parameters) of the raw data reduces from 132 to 3. The three most important parameters are initial temperature, final temperature and final strain, indicated as C1, C2 and C3, respectively. A sample of the raw data is illustrated in a 3D scatter plot. The colour indicates the geometric region of the element, suggesting that simple data processing technique did not work well on these datasets.

3.3 Data pre-possessing

3.3.1 Data clearing and weighting

An initial pre-processing of raw data is needed to identify missing or spurious elements. For example, elements haven been found having extremely high contact pressure. Identifying and removing such errors is essential to avoid the prediction model to being misled. Since the data set consists of various combinations of complex shapes and forming conditions, the number of finite elements used in each simulation would vary dramatically across different simulation files, where problems arise in this situation. Consequently, the sampling bias exists in the combined results, where some certain collected simulation files with more data are more likely to be dominated in data analysis. Therefore, the sample weighting is required, allowing adjustment of data to account for sample bias before data integration. Normally, each element in the dataset will carry equal weight i.e 1. In this work, a weighting parameters is assigned to each data point based on the size of the simulation file. The given weight is multiplied by the error

of each elements, to adjust the general performance of algorithms.

$$w^i = \frac{1}{\text{no of elements in ith simulation}} \tag{3.1}$$

3.3.2 Data standardisation and normalisation

Different finite element simulation models in the training set have observable differences in the range of physical parameters, because the models were formed using differnt materials at different forming conditions, such as forming temperature, T and forming speed, v_f. Consequently, proper data normalisation is required to find data correlation over a broad range of values Therefore, a data scaling is applied within each simulation model

The most important parameter of a material is the flow stress during the forming process, which represents the instantaneous value of stress required to plastically deform the material. The flow stress is mainly dependant on the material properties, but affected by temperature and strain rate, from the macroscopic view, i.e. forming temperature and forming speed. The material also can be formed at different temperatures, so that the temperature values were normalised with regards to initial forming temperature, the strain rate is adjusted by the forming speed. All the stresses were normalised by the flow stress.

$$T_n^{(i)<t>} = \frac{T^{(i)<t>}}{T^{(i)<0>}} \tag{3.2}$$

$$\varepsilon_n^{(i)<t>} = \frac{\varepsilon^{(i)<t>}}{\max(\varepsilon) - \min(\varepsilon)} \tag{3.3}$$

$$\sigma_n^{(i)<t>} = \frac{\sigma^{(i)<t>}}{\sigma_{fs}(T^{(i)<t>}, \dot{\varepsilon}^{(i)<t>})} \tag{3.4}$$

$$\dot{\varepsilon}_n^{(i)<t>} = \frac{\dot{\varepsilon}^{(i)<t>}}{[\max(\dot{\varepsilon}) - \min(\dot{\varepsilon})] \cdot v_f} \tag{3.5}$$

Due to the different requirements for accuracy and computational efficiency as well as actual practices for difference researchers and engineers, the finite element models were simulated in different time steps, varying from just a few steps to hundreds. In order to ensure the

performance of the data processing technique, the dimension in time had to be standardised. To balance the accuracy and computational efficiency, in this work, the time step was set to 10, and the forming time was normalised from 0 to 1 with a 0.1 interval, i.e. 0, 0.1, 0.2... 0.9, 1.

3.3.3 Data labelling for geometric features

The geometric information is one of the most important parameters in this project, so that the data set had to be labelled by detailed geometric feature. For the simulation data with available geometric data. The features are defined as Blank holding area, flat bottom, vertical wall, inclined wall, shoulder zone and corner zone. An algorithm for feature labelling was developed, which can successfully label the region of finite element data by their geometric features.

First of all, in each finite element model, the vertical orientation was standardised as the z-direction based on punch movement. Consider the the sheet blank as a curved surface, the geometry of one single element was determined by the orientation and convexity (curvature) of that local surface which contains that elements and the neighbouring elements in the Cartesian coordinate planes. The data set does not including the connecting information, so that the neighbouring elements are the 8 closest elements by calculating distance between this element to all the other elements. In this case, the hypothesis is that the element surface function is a secondary polynomial function. By using the the coordinates of 9 elements, the surface function is fitted as illustrated in Fig.3.3.

The normal vector $\mathbf{n}$ and unit normal $\hat{n}$ at the centre of the surface $z = f(x, y)$ can be calculated as:

$$n = \begin{bmatrix} \delta z/\delta x \\ \delta z/\delta y \\ 1 \end{bmatrix} \tag{3.6}$$

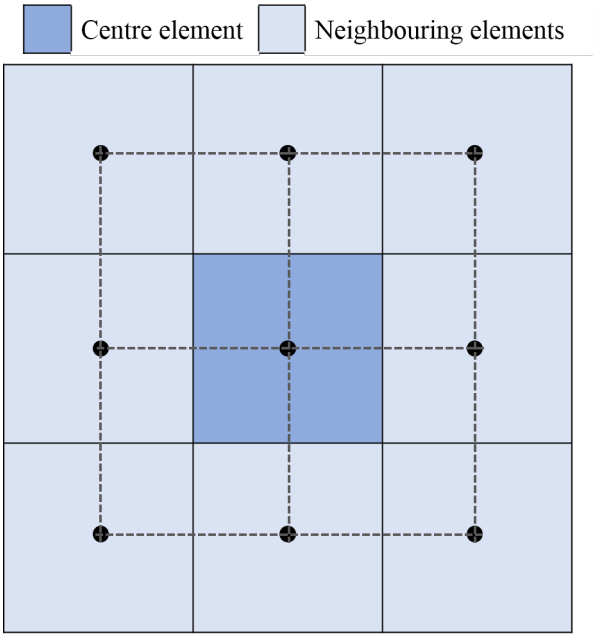


Figure 3.3: Secondary polynomial surface function fitting by using the x,y coordinates of 9 elements, one centre element and 8 neighbouring elements

$$\hat{n} = \frac{n}{|n|} \tag{3.7}$$

The angle Θ between the tangent plane of the element and the horizontal plane is equivalent to the angle between the normal vector $\hat{n}$ and the z-axis $\hat{k}$, which can be calculated as:

$$cos\Theta = \frac{\hat{n} \cdot \hat{k}}{|\hat{n}| \cdot \left|\hat{k}\right|} \tag{3.8}$$

The convexity C for each element is an indicator to determine whether the surface is concave or convex, and the flatness of the surface, which is given by the second derivative of surface:

$$C = \frac{\delta^2 z}{\delta x^2} + \frac{\delta^2 z}{\delta y^2} + \frac{\delta^2 z}{\delta x \delta y} \tag{3.9}$$

The detailed criterion is shown in Table 3.1, and Fig.3.4 illustrate the labelling results on a sample component.

Table 3.1: Labelling criterion for finite element models with known geometric information

Feature	Orientation	Convexity
Flat bottom	$\Theta < 15$	$\|C\| < 0.05$
Vertical Wall	$\Theta < 70$	$\|C\| < 0.05$
Inclined Wall	$15 \leqslant \Theta \leqslant 70$	$\|C\| < 0.05$
Shoulder	$15 \leqslant \Theta \leqslant 70$	$C \geqslant 0.05$
Corner	$15 \leqslant \Theta \leqslant 70$	$C \leqslant 0.05$

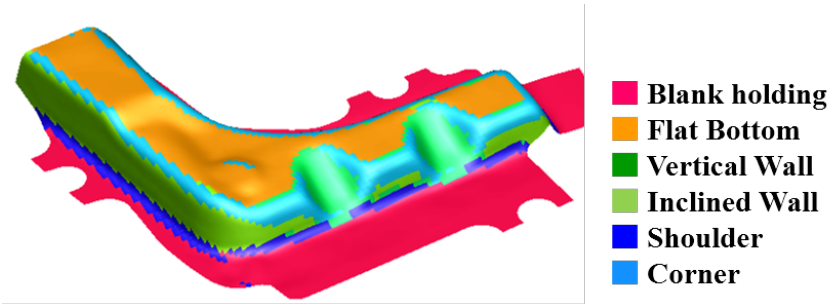


Figure 3.4: Labelling results on a sample component, illustrating the Blank holding, Flat bottom, Vertical wall, Inclined wall, shoulder and Corner areas respectively

Chapter 4

Development of machine learning based data classifier

4.1 Summary

This chapter describes the investigation on the applications of machine learning techniques to classify the input finite elements by geometric feature for sheet metal forming processes. In this project, several algorithms were constructed, ranging from elementary, such as logistic regression, to highly sophisticated, such as Feedforward neural network (FFNN) and deep recurrent neural network (RNN). This section covers the detailed methodology of establishing and improving the machine learning models and the results of these models applying on the prepared data set. A comparative study was carried out comprehensively from various perspectives, including detailed accuracy, training time, interpretable, etc, which suggested that deep recurrent neural network classifier had the best performance, with an overall accuracy over 90%.

4.2 Introduction

Resistance to the utilisation of machine learning techniques in the mechanical engineering field always exists. The relatively low interpret-ability of machine learning technique brings many questions and scepticism from researchers and engineers. However, a machine learning algorithm is a rigorous mathematically defined operation. The model parameters updating involved in the optimisation strictly follows the mathematical algorithm imposed. For example, when solving the classification problem shown in Fig. 4.1 below (i.e. try to draw a line separating the blue and red dots). The key of machine learning is to generalise how humans 'learn' from data and make certain decision.

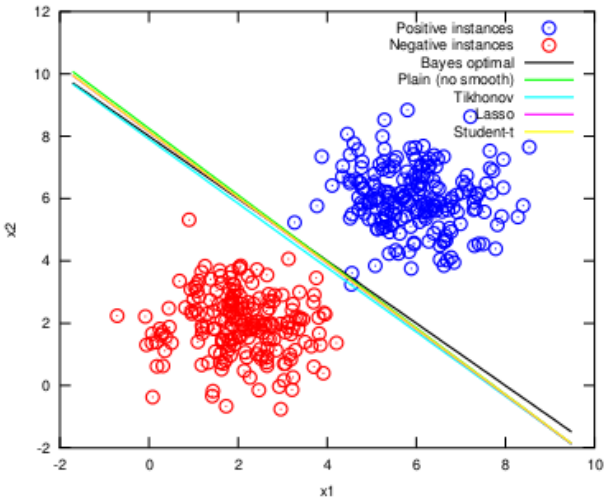


Figure 4.1: Binary classification problem with 2-dimensional input feature [1]

The key problem to solve in this project is to identify **the geometric feature of a element** on a workpiece **without geometric information**. When clients use the advanced simulation module on SmartForming® platform, only non-geometric data is uploaded. However, geometric information is of vital importance in information chain in future manufacture industry. So it is critical to have a classifier to identify the geometric information.

[1] Image source:http://atrilla.net/index.php?article=blog&bcount=2

4.3 Methodology

4.3.1 Preparation of training set

4.3.1.1 Input data of training data set

The input data contains seven physical parameters: (1)temperature, (2)major strain, (3)minor strain, (4)strain rate, (5)major stress, (6)minor stress and (7)contact pressure at all stamping stages. A 2D matrix $\boldsymbol{x}^{(i)}$ was constructed to capture entire material history of the ith finite element. Each row in the matrix refers to a physical forming parameter, and the index $^{<t>}$ indicates the number of steps, which were normalised to 11. The input data are then stacked to form a 3D tensor $\boldsymbol{X}$,which is represented below.

$$\boldsymbol{x}^{<t>} = \begin{bmatrix} x_1^{<t>} \\ x_2^{<t>} \\ x_3^{<t>} \\ x_4^{<t>} \\ x_5^{<t>} \\ x_6^{<t>} \\ x_7^{<t>} \end{bmatrix} => \begin{bmatrix} \text{Temperature} \\ \text{Major Strain} \\ \text{Minor Strain} \\ \text{Strain Rate} \\ \text{Major Stress} \\ \text{Minor Stress} \\ \text{Contact Pressure} \end{bmatrix} => \begin{bmatrix} & & & & \\ \boldsymbol{x}^{<1>} & \boldsymbol{x}^{<2>} & \boldsymbol{x}^{<3>} & \dots & \boldsymbol{x}^{<T>} \\ & & & & \end{bmatrix} \tag{4.1}$$

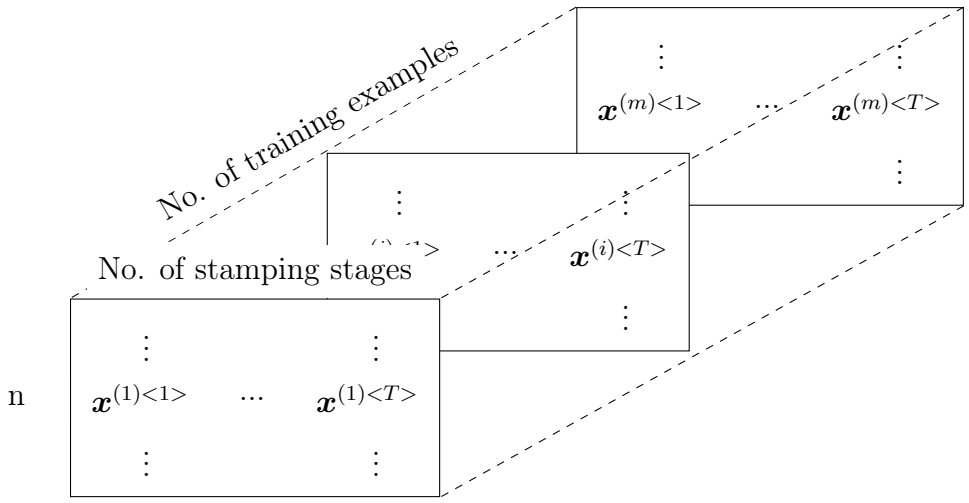


Figure 4.2: Matrix of input data of all training elements

4.3.1.2 Ouput of training data set

In addition, a scalar label $y^{(i)}$ is assigned for $\boldsymbol{x}^{(i)}$ to represent the geometric feature of the finite element. There are six classes of geometric locations, so $y \in 0, 2, ..., 5$. The correspondence physical geometric location of each number is list in Table 4.1:

Table 4.1: Scale label for each geometric feature

Feature	flange zone	Flat bottom	Vertical Wall	Inclined Wall	Shoulder	Corner
Label	0	1	2	3	4	5

A one-hot coding is transforming a categorical data to a group of data data among which the combinations of values are only those with a single '1' value and all the others are '0', for the ease of compute cross entropy loss function when solving multi-class classification problem. One-hot encoding is applied on the label data y, which transforms the scalar label y to a vector $\boldsymbol{y}$. The examples of such transformation is illustrated below.

$$\text{OH}(y=0) = \begin{bmatrix} 1 \\ 0 \\ 0 \\ 0 \\ 0 \\ 0 \end{bmatrix}, \quad \text{OH}(y=1) = \begin{bmatrix} 0 \\ 1 \\ 0 \\ 0 \\ 0 \\ 0 \end{bmatrix}, ... \quad \text{OH}(y=5) = \begin{bmatrix} 0 \\ 0 \\ 0 \\ 0 \\ 0 \\ 1 \end{bmatrix} \tag{4.2}$$

4.3.2 Model architecture

Figure 4.3 shows the model architecture for logistic regression, feed-forward neural network and deep recurrent neural network used in this chapter. The architecture (a) is the single neuron network (SNNN) using logistic function (see section 2.3.1). The architecture (b) is the feed forward neural network (see section 2.3.2. The architecture (c) is the deep neural network design with multiple recurrent layers (see section 2.3.3. LSTM is a special kind of neural network, capable of learning long-term dependencies. Dropout is a technique to randomly drop

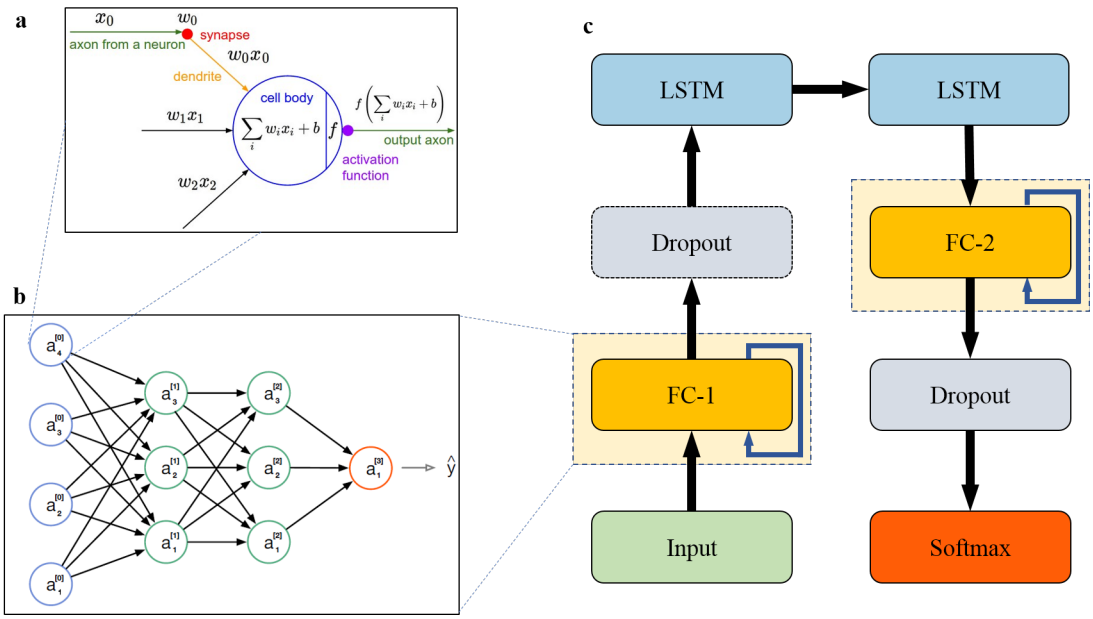


Figure 4.3: Model architecture for (a) logistic regression (b) feed-forward neural network and (c) deep recurrent neural network

units from the neural network during training to prevents units from co-adapting too much. LSTM were used and Dropout layers were also added to prevent the over-fitting/variance issue, followed by a final softmax layer.

The fully connected layers (FC) is the feed-forward neural network. The input layer is a vector with dimension of 7-by-1. The information is input to FC-1 and output activation with dimension of 32-by-1. The number of LSTM layers is studied in the results section. Softmax layer has the same dimension as the number of classes k, i.e. 6.

$$\sigma_{softmax}(z_j) = \frac{e^{z_j}}{\sum_1^k e^{z_k}} \tag{4.3}$$

Cross-entropy is the cost function used in all the machine learning models. Minimizing the cross entropy is to make the predict label $\hat{\boldsymbol{y}}$ to be more resemble the actual label $\boldsymbol{y}$.

$$J(\boldsymbol{y}, \hat{\boldsymbol{y}}) = -\frac{1}{m}\sum_{i=1}^{m} \boldsymbol{y}^{(i)} \bullet \log \hat{\boldsymbol{y}}^{(i)} = -\frac{1}{m}\sum_{i=1}^{m}\sum_{j=1}^{k} y_j \log \hat{y}_j \tag{4.4}$$

Optimization method used in this process is achieved by gradient update of weights and biases. The Adam optimiser, developed by (Kingma and Ba, 2014), is used in this project, which has

shown excellent performance in training on various neural networks.

4.3.3 Model evaluation methods

4.3.3.1 Cross Validation

In development of neural network models, the dataset is randomly split into two different groups: a training dataset and a test dataset. The training dataset contains 90 % of the data while the test one contains the remaining 10 %. The training dataset is used to optimise the weights and bias of machine learning model, and it is common for a well trained machined model to have an excellent performance in the training data, and performs significantly worse on new data due to the over-fitting problem. The purpose of the test dataset is to validated the actual performance of the model when it is exposed to independent unknown input $\boldsymbol{x}$.

All the results in this section are based on the model performances in test dataset. Accuracy is the most important evaluation metric, which is essentially in the number of tested samples how many samples the model is able to make correct predictions. Precision, recall and F1-score are the other three important evaluation metrics of model accuracy, which are introduced and explained in the following section.

4.3.3.2 Confusion Matrix

] A confusion matrix is a table that is used to describe the performance of a classification model. A confusion matrix for a binary classification problem is illustrated as an example in this section (as shown in Fig. 4.4. This confusion matrix has a dimension of 2-by-2, namely true positive, false negative, false positive and true negative. The number in the true positive box represent the percentage of true label is correctly predicted. False negative represents the percentage of ture label is predicted wrongly. False positive means the percentage of false label is correctly predicted. True negative means the false label is wrongly predicted.

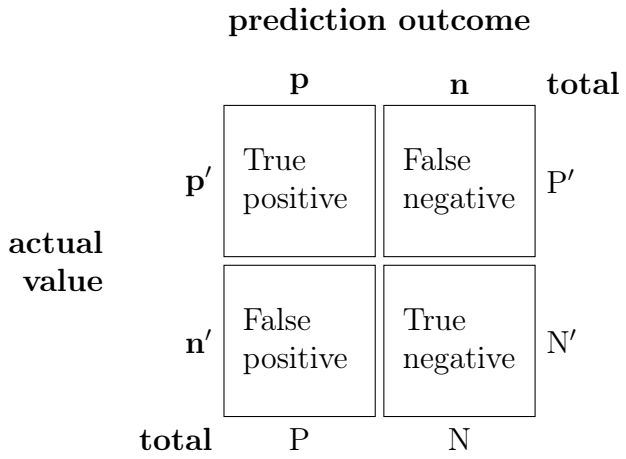


Figure 4.4: Example of a confusion matrix for describing the performance of a classification model

The precision, recall, and F1-score is determined as:

$$\text{Precision} = \frac{TP}{TP + FP} \tag{4.5}$$

$$\text{Recall} = \frac{TP}{TP + FN} \tag{4.6}$$

$$\text{F1 Score} = \frac{2}{\text{Precision}^{-1} + \text{Recall}^{-1}} \tag{4.7}$$

where precision is the ratio of correctly predicted positive observations to the total predicted positive observations, and recall is the ratio of correctly predicted positive observations to the all observations in actual class. F1 Score is the weighted average of Precision and Recall.

4.3.3.3 Overfitting issues

Overfitting could lead to bad performance of the neural network model, and three different methods in solving these problems is used in this section (1) dropout, (2) small batch size (3) regularization. The details of the three methods in reducing variance will be presented in the result section instead.

4.4 Results of logistic regression model for binary classification

In this section, a logistic regression model was developed to identify whether the element is in the die cavity region. The most significant difference between the element in the die cavity region and in the blank holding region is the strain level. The logistic regression classifier was then trained by two different data sets. The first only used strain related parameters, i.e. major strain, minor strain, strain rate, while the second used a full data set. The classifier was trained at 4 different learning rates for 30,000 iterations, and the results are shown in Table 4.2. The best accuracy by using the strain data set was 82.89%, and it increased to 87.7% by introducing temperature and contact pressure data in the data set.

Table 4.2: Accuracy of logistic regression classification using different data set at different learning rate

	Accuracy			
Learning rate	0.05	0.1	1	3
Strain data set	82.43%	82.89%	73.06%	67.20%
Full data set	87.39%	**87.70%**	71.61%	69.68%

A confusion matrix shows how the model performs on classification in detail. For the model trained by the strain data set, 84% of the element from blank holding area are correctly recognised as blank holding area, while the rest 16% are wrongly identified as the die cavity region. 82% of the elements from die cavity region are recognised as the right region while the rest 18% had the wrong geometric output. The accuracy of the logistic regression model was improved when it was trained by the full data set, 90% of the blank holding elements and 86% of the die cavity elements were correctly filtered out, and 14% of the die cavity elements and 10% of the die cavity element were wrongly recognised. Using both data sets, the model with learning rate of 0.1 always gave the highest accuracy, respectively. The learning curve of logistic regression model is illustrated in Fig. 4.5. The learning process converged very fast, and reach a stable cost value at 100 iterations when the learning rate is 0.05 and 0.1, while the curve did not converge when learning rate is larger than 1.

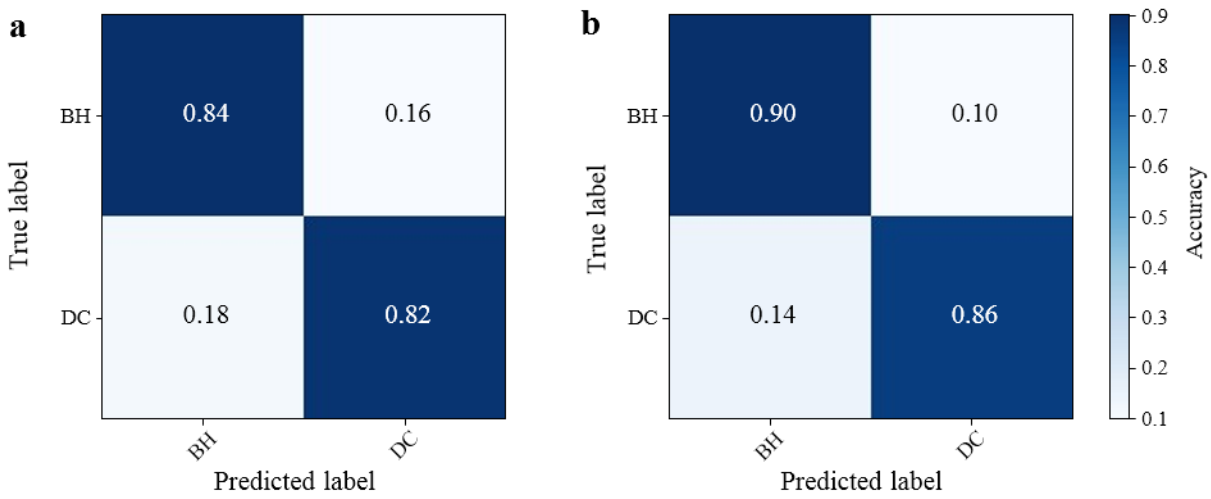


Figure 4.5: The confusion matrix of logistic regression model using (a) strain data set and (b) full data set at optimised learning rate

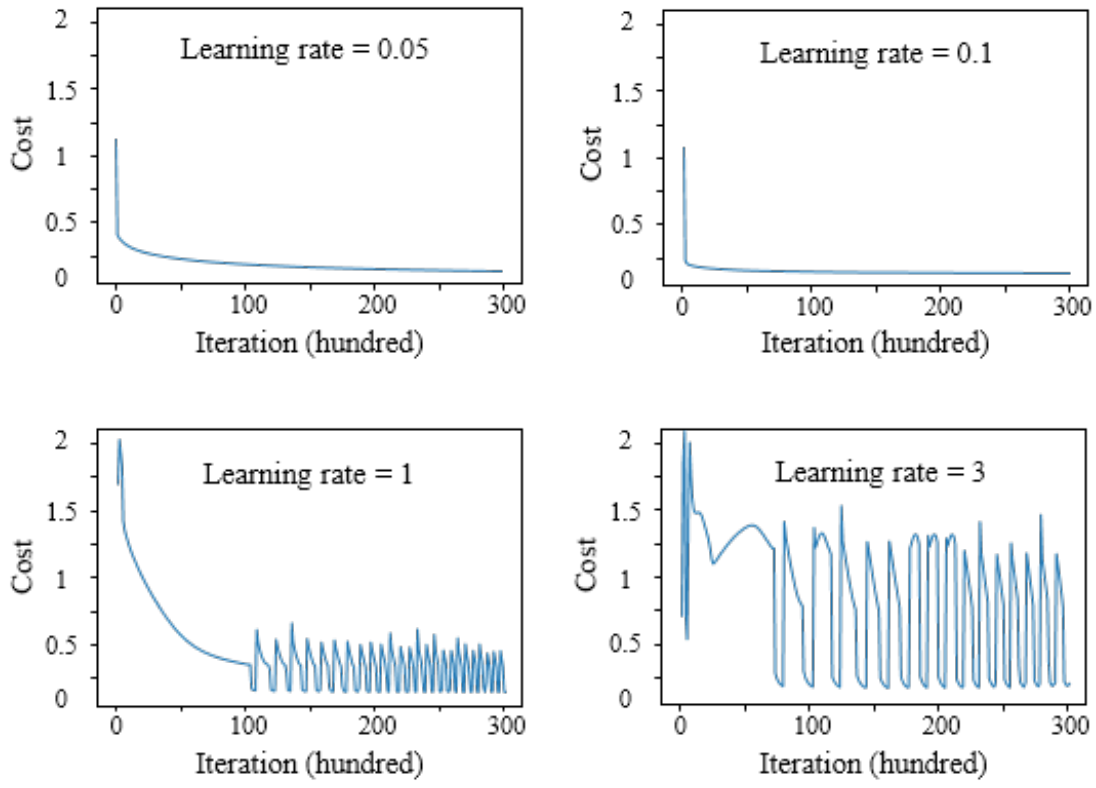


Figure 4.6: The learning curve of logistic regression classification with different learning rate, 0.05, 0.1, 1 and 3 respectively

4.5 Results of Feedforward neural network

4.5.1 One-hidden layer FFNN

Feedforward neural network is a more advanced machine learning algorithm that allows more complex feature extraction from training data. This section introduced the development of feedforward neural network model using full data set. An FFNN model with one hidden layer was firstly developed in this section. FFNNs with 4, 8, 12 and 20 neurons in hidden layer were trained and tested, at learning rate of 0.000005 in 2500 iterations. The performance of the neural networks are shown in Table 4.3. Accuracy increases when the number of neurons increases, and the over-fitting can be negligible. When the neuron increases, the size of matrix increase proportionally, the computational power required is thus much larger. The optimised overall performance is 12 neurons. Fig. 4.7 shows the confusion matrix of test data sets using 4, 8, 12, 20 neurons, respectively. The FFNN model with 12 neurons has the highest accuracy on recognising BH region elements, 98% but lowest for DC elements. Models with 8 and 20 neurons have similar ability to detect element in both regions.

Table 4.3: Accuracy of data filter for different neurons in a one hidden layer FFNN

Neurons in hidden layer	Train accuracy	Test accuracy
4	90.03%	88.64%
8	91.93%	91.78%
12	92.18%	92.26%
20	90.99%	91.78%

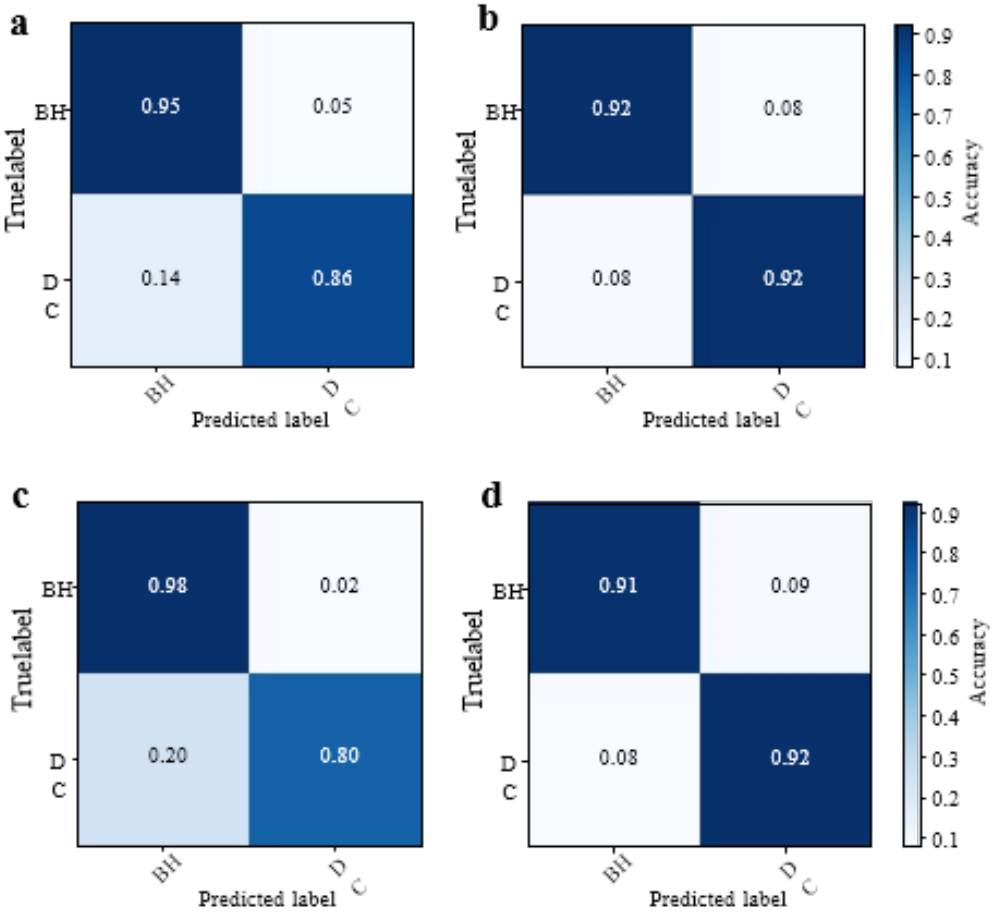


Figure 4.7: The confusion matrix of test data sets of one hidden layer FFNN model of (a) 4, (b) 8, (c) 12, (d) 20 neurons, respectively

4.5.2 Multi hidden layer feedforward neural network

In order to process a more complex classification problem, i.e. to separate the data into six regions, FFNN with a multiple hidden layer structure was developed in this section. For each layer, the number of neurons (dimension) can be altered. Instead of only choosing one parameter, multiple parameters could be set, also, this process would use trial-and-error. If it is a 3-layer network, the selection of dimension of hidden layers could be [i,j,k] where i,j,k could be any integer. Although in convention the dimension is preferable smaller than input dimension. Therefore, FFNN filter model with 3, 4 and 5 hidden layers were developed and trained, and filter model with 1 hidden layer was also trained for comparison.

FFNN with 3 hidden layers were also trained for BH and DC region classification. The accuracy for training set and test set after convergence (3,500 iterations trained) are 92.83% and 92.30%, which is nis similiar to one hidden layer model, however, the computational power required in training is much higher. The confusion matrix is shown in Fig. 4.8, and accuracy is 97% for BH elements and 87% for DC elements.

By increasing the number of layers, it is expected to have positive impact on the model performance. However, one more layer leads to a huge increase in computational power required. Also, it will make the neural network more difficult to tune. As shown in Fig.4.9, the FFNN with 4 hidden layers has produced the best result. Also, accuracies from both training and test sets are close to each other, which means over-fitting is negligible. Comparing 5-layer FFNN with 4-layer FFNN, not only did the overall accuracy drop, but more importantly, it became unable identify the elements in the Upward Bending (UB) region. The 3-layer FFNN has lower overall accuracies than 4-layer and 5-layer FFNN, but it performs better than 1-layer FFNN on feature classification. They were able to identify elements in BH, Flat Bottom and Vertical Wall regions with relatively acceptable accuracies. Accuracy on Inclined Wall and Downward Bending is not high enough, and accuracy on Upward Bending region is too low.

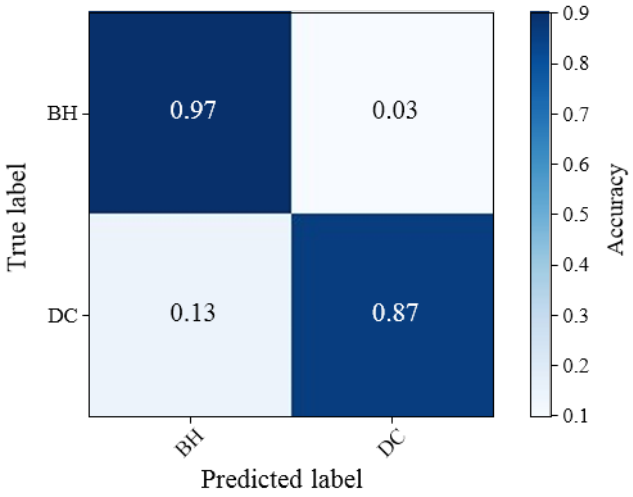


Figure 4.8: The confusion matrix of three layer FFNN model

Table 4.4: Accuracy of FFNN models with multiply hidden layer

Number of hidden layers [Neurons in hidden layer]	Train accuracy	Test accuracy	Convergence iterations
3 [40, 20, 15]	68.66%	68.6%	8,000
4 [45, 35, 25, 15]	72.51%	72.71%	12,000
5 [40, 30, 30, 20, 15]	67.54%	67.49%	8,000

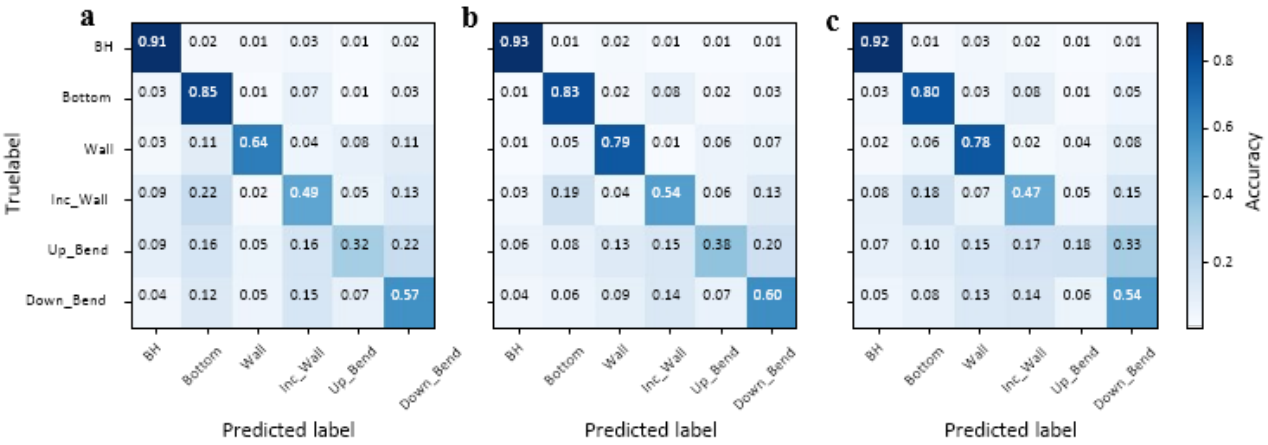


Figure 4.9: The confusion matrix of test set of FFNN models with (a) three hidden layers, (b) four hidden layers and (c) five hidden layers

4.6 Recurrent neural network

4.6.1 Effect of learning rate and use of non-linearity in FC-1

The study on learning rate in FC-1 was conducted with batch-size of 4096 over 2000 iterations, and the results are illustraed in table 4.5. The RNN model has the best performance at a learning rate of 0.005, where all performance metrics are higher than other conditions. A unit that implements linear ramp function is referred to as a rectified linear activation unit, or ReLU for short. Networks that use the rectifier function for the hidden layers can significantly improved the performance of feedforward networks. In this workm when the learning rate reaches approximately 0.01, the model did not converge. Furthermore, by introducing ReLU nonlinearity, the model accuracy increased by 2.8% .

Table 4.5: Effect of learning rate and nonlinearity in FC-1 layer on RNN model performance, using batch size of 4096 at 2000 iterations

LR	Non Linearity	Train CrossEnt	Train Acc (%)	Dev Acc (%)
1E-04	N/A	1.35	69.1	68.1
	ReLU	1.35	69.0	69.3
5E-04	N/A	1.33	70.9	70.5
	ReLU	1.29	75.1	75.1
1E-03	N/A	1.28	75.7	74.7
	ReLU	1.26	78.2	77.5
5E-03	N/A	1.21	83.3	81.7
	ReLU	**1.18**	**86.4**	**84.5**

4.6.2 Effect of layer number in LSTM

The study on layer number in LSTM unit was conducted with batch-size of 4096 for 5000 iterations, and the reults are illustrated in in Table 4.6. The RNN models with 2 or 3 LSTM layers have the best performance. Increasing the number of layers requires longer training time and leads to more over-fitting problems.

Table 4.6: Effect of number of LSTM recurrent layer on RNN model performance, using batch size of 4096 at 5000 iterations

Model	Train CrossEnt	Train Acc(%)	Dev Acc(%)
1 Layer	1.18	86.30	84.40
2 Layer	**1.15**	**89.10**	**86.60**
3 Layer	**1.17**	**89.12**	**86.27**
4 Layer	1.16	88.10	85.84

4.6.3 Methods of reducing classifier variance

Deep RNN was able to achieve training accuracy of 89.1%, and issue of over-fitting becomes severer with deeper models. In order to solve over-fitting, the dropout method was used. Figure 4.10 shows the mechanism of dropout for a feed-forward NN, where an neural will assign a probability of being dropout during the forward propagation. It can decrease the dependency of subsequent layers, leading to a more average weights to be assgined to prevent the RNN over-fitted to specific data points. On the other hand, the dropout reduces the number of neurons, and its ability in capturing higher order nonlinearity is also reduced.

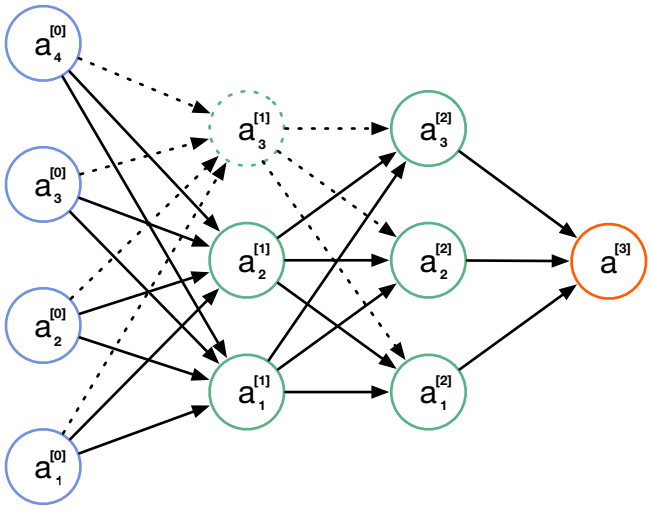


Figure 4.10: Dropout of Neural Network

4.6.3.1 Dropout in fully connect layers

The study of dropout in RNN layers was conducted with 4096 batch size for 5000 iterations. As shown in the Fig. 4.10 dropout is designed between layers of recurrent unit to reduce the variance problem of the model (Gal and Ghahramani, 2015)), where the recurrent unit has

a probability of dropout at every time-step ((Zaremba et al., 2014)). Leaky ReLU was used instead of ReLU for improving the model performance.

Table 4.7: Study of dropout in fully connected layers

Non Linearity	Dropout Prob. (%)	Train CrossEnt	Train Acc (%)	Test Acc (%)	Test-Train Diff (%)
ReLu	0	1.14	89.12	86.58	2.5
	5	1.18	85.20	84.76	0.44
	10	1.20	83.13	82.28	0.85
Leaky ReLU	0	1.17	87.53	85.71	1.82
	5	1.16	88.54	87.24	1.3
	10	1.16	88.43	86.27	2.16
	15	1.16	87.91	86.25	1.66
	20	1.17	84.43	86.01	1.58

The dropout in FC layers reduced the variance issue of the model. 5 percent dropout had the best performance in balancing the bias and variance trade-off. By introducing the leaky ReLU, the model with 5 percent had better performance than the model without dropout in training accuracy, which is resulted from the additional randomness involved during training that helps the NN finding global optimal points.

4.6.3.2 Effect of L2 Regularization in Fully Connected Layers

TL2 regularization is another technique used for solving variance issues in an RNN model. The L2 regularization is the modification of the cost function, where an additional term is introduced:

$$J(\boldsymbol{W}, \boldsymbol{b}) = J_{unreg}(\boldsymbol{W}, \boldsymbol{b}) + \lambda \sum_{l=1}^{N} \boldsymbol{W}^{[l]} : \boldsymbol{W}^{[l]} \tag{4.8}$$

The effect of L2 regularization was conducted at 5000 iterations, and the results are shown in Table 4.8. L2 regularization reduced the train-dev accuracy difference less than 1%, but increased the bias issue. Therefore, a good range of selecting λ will be around 0.00001.

Table 4.8: Investigation on the effect of L2 regularization

LR	Train CrossEnt	Train Acc(%)	Dev Acc(%)	Dev-Train Diff (%)
1E-06	1.23	79.54	76.91	2.75
5E-06	1.21	82.87	80.84	2.03
1E-05	1.14	89.21	87.28	1.93
5E-05	1.21	81.87	80.08	1.79
1E-04	1.16	87.12	85.91	1.21
5E-04	1.23	80.20	79.74	0.46
1E-03	1.22	81.18	80.07	1.11
5E-03	1.37	66.55	65.87	0.68
1E-02	1.28	75.97	75.02	0.95
2E-02	1.38	65.56	65.16	0.40
5E-02	1.41	62.69	62.51	0.18

4.6.3.3 Effect of batch size

In this section, the effect of batch size on the model performance was investigated. A Large batch size was used in the previous training process. A small batch size means that less data is fed in the training process at a time, which could improve the statistical efficiency, Wilson and Martinez (2003). Consequently, 5 different batch sizes were tested under 3 different learning rates at 10000 iterations

Table 4.9: Investigation on the regularisation effect of batch size at different Learning Rates

LR	Batch Size	Train CrossEnt	Train Acc(%)	Dev Acc(%)	Dev-Train Diff (%)
5E-03	256	1.23	80.72	80.46	0.19
	512	1.19	81.84	80.83	1.01
	1024	1.18	85.09	83.42	1.71
	2048	1.20	83.73	82.81	0.95
1E-03	256	1.19	86.00	85.65	0.35
	512	1.18	86.54	83.89	2.65
	1024	1.25	78.74	76.22	2.52
	2048	1.21	82.43	80.22	2.21
5E-04	256	1.195	84.86	84.43	0.42
	512	1.23	80.88	79.61	1.27
	1024	1.30	74.66	74.54	0.14
	2048	1.20	84.74	82.93	1.82

Batch size has considerable effect on the accuracy of the models, as shown in Table 4.9. Small batch size trended to have both higher train and development accuracy within a 0.5% differnece. Consequently, such hyper-parameter setting is use in the final model.

4.6.4 Comparison of final models

This section presented the final versions of various architecture of RNN model, The dimensions of FC-2 and FC-3 is set as 32 with a 5% dropout rate. The learning rate is 0.01 with a batch size of 256. Regularization was not necessary in this project. The final models have achieved the accuracy over 90%.

Table 4.10: Performance of various fined tunned models

Model	Dev CrossEnt	Dev Acc(%)	Recall(%)	Precision(%)	F Score(%)
2 Layer	0.2929	87.78	87.78	88.06	87.86
3 Layer	0.2148	90.06	90.06	90.09	90.07
2 Layer Leaky	0.2762	88.52	88.52	88.63	88.56
2 Layer Bi-D	0.1912	92.74	92.74	92.74	92.74

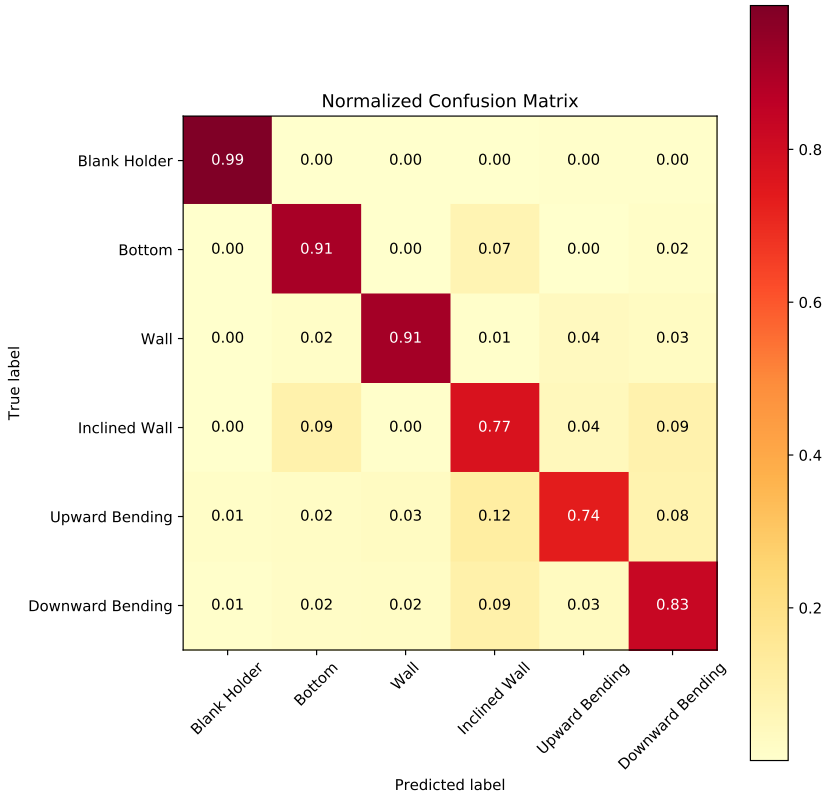


Figure 4.11: The confusion matrix for final 2 layer LSTM model

This chapter developed a machine learning based model, providing a reliable tool to classify the finite element data by their geometric information from the thermo-mechanical behaviour. To discover the scientific meaning behind, several physical based models are developed in the next chapter.

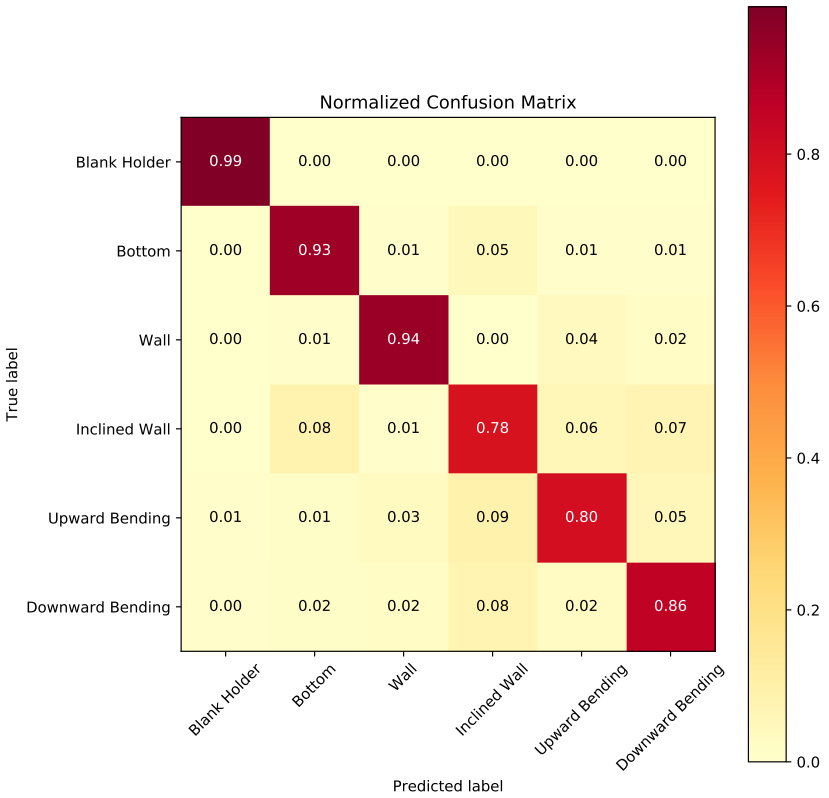


Figure 4.12: The confusion matrix for final 3 layer LSTM model

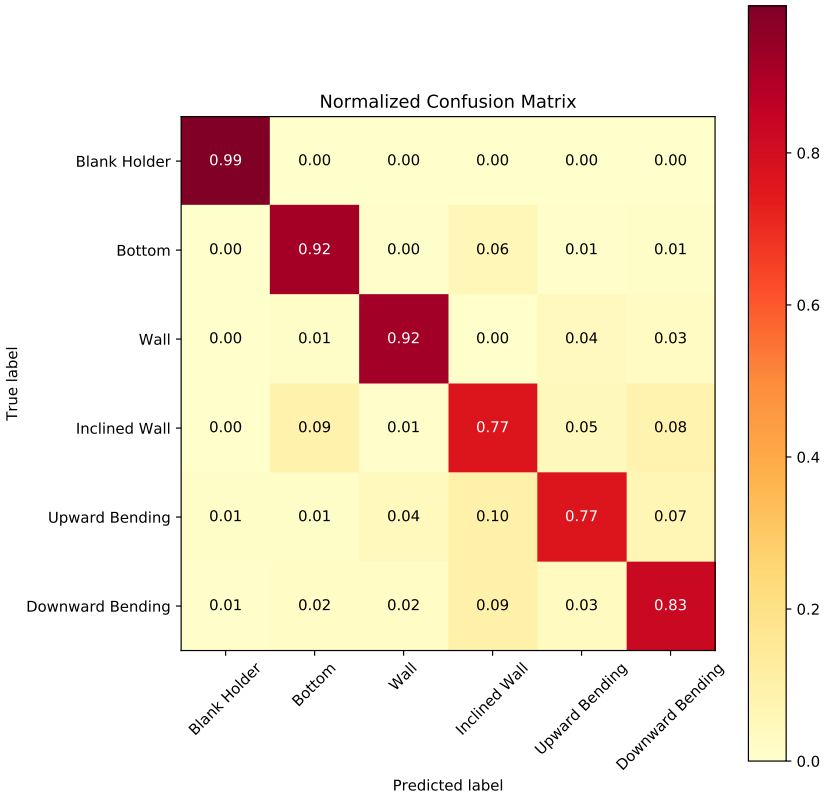


Figure 4.13: The confusion matrix for final 2 layer with leaky-ReLU activation LSTM model

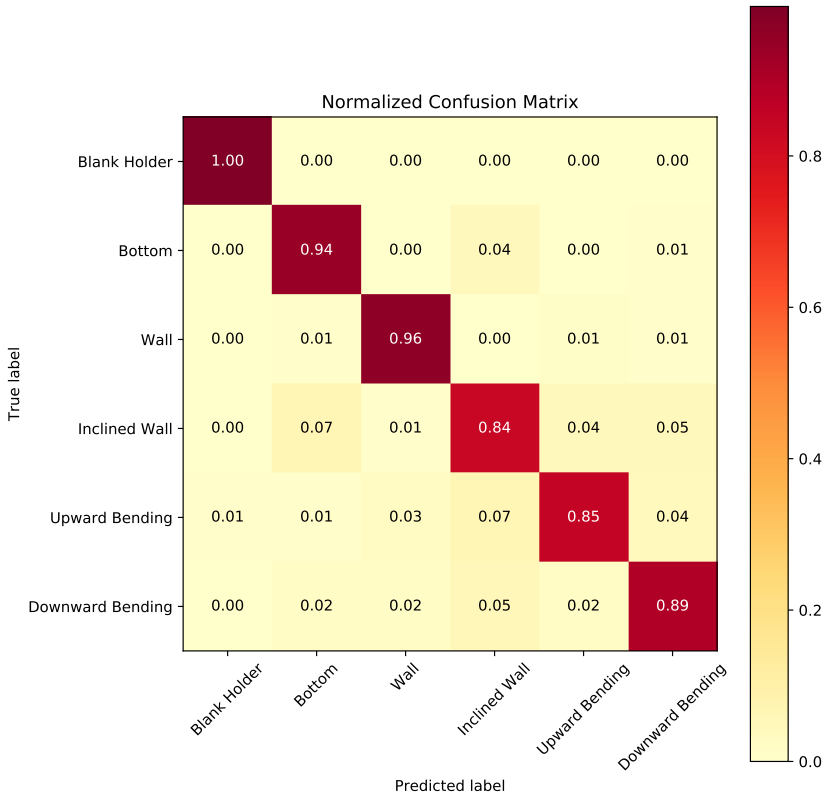


Figure 4.14: The confusion matrix for final 2 layer bi-direction LSTM model

Chapter 5

Development of physics based data filtering technique

5.1 Summary

This section dedicates into the investigation on the development of physical-based data filtering technique in the sheet metal forming processes based on the evolutionary thermo-mechanical behaviour. In this project, a strain-based filter, a temperature drop filter and a thermo-mechanical evolutionary algorithm were constructed. This section covers the detailed methodology and results of the physical-based filter.

5.2 Strain-based filter

Strain is one of the most important parameters in the sheet metal forming process. During the forming process, the elements in the blank holding area usually experience little deformation and at a very low level of strain value. A strain filter was then developed for identifying elements in the blank holding (BH) region and in the die cavity (DC) region. This filter was developed to generate a more representative dataset for a specific sheet metal forming process by eliminating

the elements in blank holding area from the dataset. The criteria for this filter were determined by analysing trends and the distribution of the strain related data during process.

5.2.1 Strain related parameters preparation

In the dataset, the available data related to strain are major strain, minor strain and strain rate. Thickening and β are derived from these values, which providing more information for strain filter. Firstly, the constant volume assumption is applied,

$$\varepsilon_1 + \varepsilon_2 + \varepsilon_3 = \frac{\Delta V}{V} = 0 \tag{5.1}$$

and the thickening, ε_3, is calculated by

$$\varepsilon_3 = -\varepsilon_1 - \varepsilon_2 \tag{5.2}$$

and β is calculated by

$$\beta = \frac{\varepsilon_1}{\varepsilon_2} \tag{5.3}$$

The vector of input training set with 5 dimension is constructed, and each element in the vector corresponds to a physical forming parameter during the stamping stage:

$$\boldsymbol{x}^{<t>} = \begin{bmatrix} x_1^{<t>} \\ x_2^{<t>} \\ x_3^{<t>} \\ x_4^{<t>} \\ x_5^{<t>} \end{bmatrix} => \begin{bmatrix} \text{Major Strain} \\ \text{Minor Strain} \\ \text{Strain Rate} \\ \text{Thickening} \\ \beta \end{bmatrix} => \begin{bmatrix} | & | & | & & | \\ \boldsymbol{x}^{<1>} & \boldsymbol{x}^{<2>} & \boldsymbol{x}^{<3>} & \dots & \boldsymbol{x}^{<T>} \\ | & | & | & & | \end{bmatrix} \tag{5.4}$$

5.2.2 Filter Mechanism and criterion

The filter mechanism is illustrated in Fig.5.1. The filter consists of 3 main algorithms to filter out the element in the die cavity region. The 1st layer of the filter based on strain rate data,

thickening value is then applied to the remaining data. A strain filter is applied to give the final results.

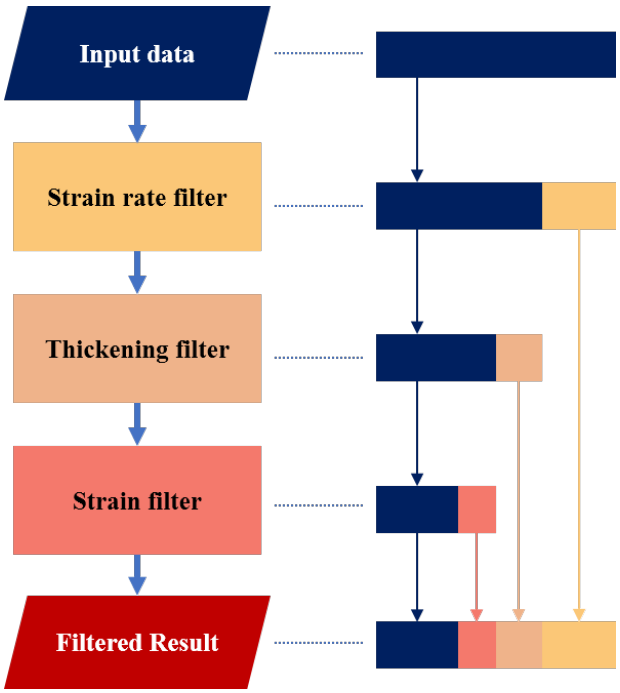


Figure 5.1: Schematic of the strain-based filter, dark blue part represents left-over elements, and the remaining parts are filtered elements for die cavity region, and each step the left-over is sent into the next level of filter

Strain rate filter:

$$\dot{\varepsilon}^{i,9} - \dot{\varepsilon}^{i,3} > c_1 \sum_{i=1}^{n} \frac{(\dot{\varepsilon}^{9} - \dot{\varepsilon}^{3})}{n} \tag{5.5}$$

where i is the element number, n is the total number of element in simulation models.

Thickness filter:

$$\dot{\varepsilon}^{m,3} - \dot{\varepsilon}^{m,9} > 0.9 \times \dot{\varepsilon}^{m,3} \tag{5.6}$$

Strain filter:

$$\varepsilon_{1,f} < c_3 \tag{5.7}$$

5.2.3 Strain filter results

By applying the weighting, the overall accuracy are calculated by:

$$W = \frac{n_m}{n_{total}} \tag{5.8}$$

$$a_{overall} = \sum_{m=1}^{n_m} \frac{n_m}{n_{total}} a_m = 78.3\% \tag{5.9}$$

where W represents the weight of each model which is calculated by the element number of each model, n_m and the total number of element, n_{total}. a_m is the accuracy of each model, and $a_{overall}$ is the overall accuracy. For simply geometry, the accuracy can be 95% while for complex geometry, the accuracy is only 70%. This indicates that this preliminary strain filter was effect by the geometry of the components.

5.3 Temperature drop filter

Therefore, a temperature filter was developed to identify the formed part in the raw data of the FE simulation. A key feature of the blank holding region is that it is usually kept double-side contact to blank holder and die, while the formed part will undergo a process of single-side contact with the punch. Therefore, the differences of temperature evolutions between the FE simulation and a calculated temperature drop based on double-sided condition can be used as a criterion to determine the contact condition of the blank. The energy balance equation for heat transfer analysis is expressed as:

$$kA\Delta T + V\dot{r} - mc\dot{T} = 0 \tag{5.10}$$

where $kA\Delta T$ is the heat transfer rate, k denotes interface heat transfer coefficient, A is the area of the element in FE simulation and ΔT denotes temperature gradient between the surface, $V\dot{r}$ is the heat generation rate, and $mc\dot{T}$ is the internal energy-rate, c is the specific heat capacity.

Table 5.1: Parameters in heat transfer filter

h_T m	h_B m	c_T $J/(gk)$	c_B $J/(gk)$	ρ_T g/m^3	ρ_B g/m^3
0.006	0.0015	0.473	0.891	2.7	7.85

The heat generation in the deforming body is only due to plastic deformation:

$$\dot{r} = \kappa\sigma\dot{\epsilon} \tag{5.11}$$

where the heat generation efficiency, κ, represents the fraction of mechanical energy transformed into heat and is usually assumed to be 0.9. The internal heat transfer coefficient is a function of contact pressure, P.

$$k = f(P) \tag{5.12}$$

The time-based internal heat transfer between the surfaces can be determined by:

$$\dot{T_T} = \frac{k(P)A(T_B - T_T)}{m_T c_T} \tag{5.13}$$

$$\dot{T_B} = \frac{k(P)A(T_T - T_B)}{m_B c_B} + V\dot{r} \tag{5.14}$$

where $\dot{T_T}$ and $\dot{T_B}$ the temperature change at the current stage for tool and blank, respectively.

$$\dot{T}_{T,i+1} = \dot{T}_{T,i} + \frac{k(P_i)(T_{B,i} - T_{T,i})dt}{h_T c_T \rho_T} \tag{5.15}$$

$$\dot{T}_{B,i+1} = \dot{T}_{B,i} + \frac{k(P_i)(T_{T,i} - T_{B,i})dt}{h_B c_B \rho_B} + Ah_B\kappa\sigma_i\dot{\epsilon}_i \tag{5.16}$$

where $\dot{T_{T,i+1}}$ and $\dot{T_{B,i+1}}$ the temperature change at the next stage for tool and blank, respectively.

Therefore, the evolution of theoretical double-side based temperature drops of elements is obtained, which is then compared to the simulative results. Those elements with much less temperature drop are identified. A B-pillar and a limited height dome shape are tested as examples. The parameters used in heat transfer calculation are listed in Table 5.1. A refined

location filter is carried out for comparison. For the B-pillar, the remaining elements in blue are almost the same as the location filter, about 96.3% in similarity. It is worth mentioning that at the blank holder area there is a region which should be filtered out but remained. Looking into this area, it is found that in the original simulation the contact pressure of this area is relatively higher than the remaining part of the blank holder area, resulting in a larger temperature drop. Due to the heat conduction, the heat from surrounding elements transferred into this area and thus the simulated temperature drop is higher than analytical calculation, leading to the error in the filter process. Same problem is found in the dome shape simulation, the sheet blank in dome simulation is clamped by the die and blank holder in the drawbead region. The heat in this region transferred into the surrounding elements, leading to the blank holder part remained but the elements close to it is filtered out. The similarity of temperature filter and location filter is still above 86%, which is acceptable. In summary, the problem of this method is that the internal conduction within the sheet metal itself is ignored, therefore, those elements that are filtered out due to higher temperature drop can be close to blank holder area rather than on the blank holder area.

$$a_{overall} = \sum_{m=1}^{n_m} \frac{n_m}{n_{total}} a_m = 81.3\% \tag{5.17}$$

5.4 Unified thermo-mechanical evolutionary algorithms

In this work, thermo-mechanical evolutionary algorithms were developed to enable geometrical characterisation of finite elements from high temperature sheet metal forming process simulations in the absence of spatial or visual data. Comparative studies were conducted focusing on a dataset comprising vast volumes of experimentally verified FEA data from different part geometries. It was found that an equivalent strain uni-variate algorithm was rigorous in recognising the blank holding area with an accuracy of 94.5%. By utilising the evolution of strain, strain rate and temperature, a time-dependent multivariate algorithm was able to successfully identify the side wall and die bottom areas with accuracy of 92.3% and 95.1%, respectively.

Moreover, the performance of the multivariate algorithm was further increased by introducing stress states, such as the Lode parameter and stress triaxiality. The utilisation of these algorithms thus enables the visualisation of high temperature metal forming processes from the analysis and processing of digital deformation history data.

5.4.1 Thermo-mechanical data review

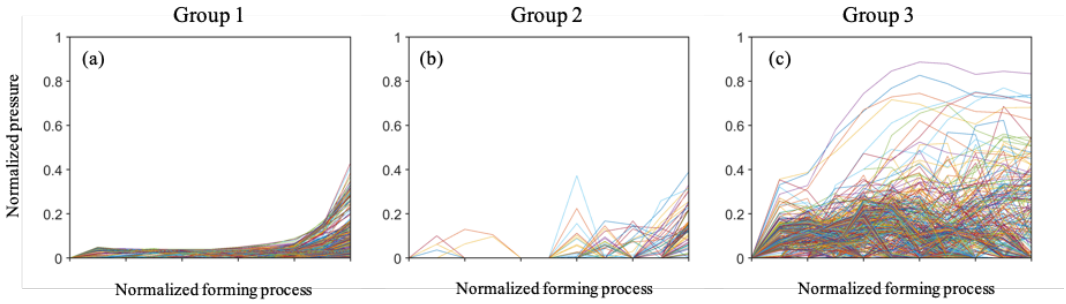


Figure 5.2: Example of data used in physical-based classification model research. Normalized pressure of raw data are illustrated along the normalised forming process, showing different patterns with various geometric locations.

The benchmark data have been labelled as three groups with distinct features, suggesting the three distinct geometric origins of these data. Fig. 5.2 (a), (b) and (c) show the evolution of contact pressure of the three features against forming time. As shown in Fig. 5.2 (a), at the initial stage from 0 to 0.8 forming time, the contact pressure of the data in this region is approximately 10% of the flow stress of the material, indicating that the material in this region is loaded elastically at the beginning of the forming process. The contact pressure of the data in this region increases by 3 times at the end of the forming process from 0.8 to 1, which might be caused by plastic deformation at this stage. Fig. 5.2 (b) shows the evolution of contact pressure of data group 2. The contact pressure of the data in this region is found to be a discontinuous mode, i.e. none of the data from this region is loaded in the middle of the forming process, which could be caused by the discontinuous contact between the workpiece and die. Fig. 5.2 (c) shows the evolution of contact pressure of data group 3. The contact pressure of the data in this region is up to 0.8, showing a severe oscillation pattern from 0.1 to 1 forming time, suggesting that the data in this region could be involved into the plastic deformation in a transient manner.

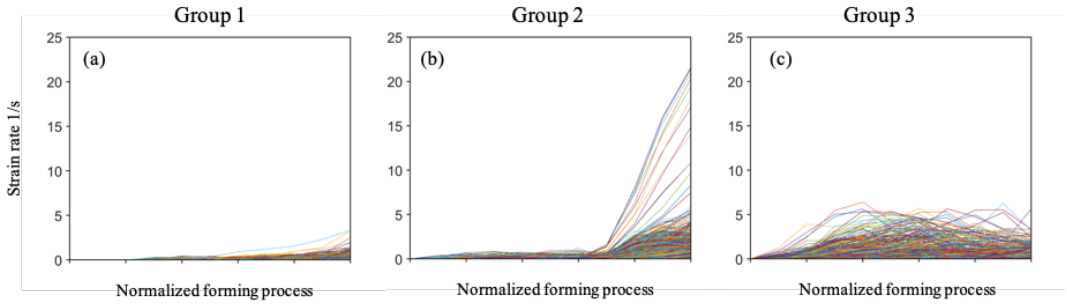


Figure 5.3: Example of data used in physical-based classification model research. Strain rate of raw data are illustrated along the normalised forming process, showing different patterns with various geometric locations.

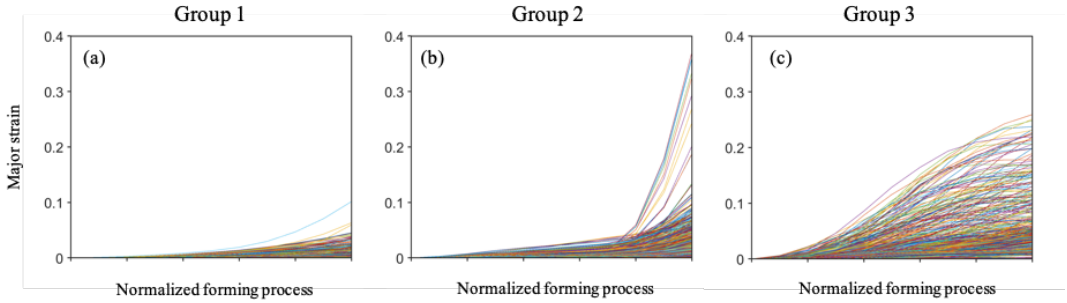


Figure 5.4: Example of data used in physical-based classification model research. Major strain of raw data are illustrated along the normalised forming process, showing different patterns with various geometric locations.

Evolutions of plastic strain rate against forming time are presented in Fig. 5.3 (a), (b) and (c), and the accumulated plastic strains are presented in Fig. 5.3 (a), (b) and (c). The strain rate of the data group 1 ramps up gradually from 0 at the forming time of 0.2 to 5 s-1 at the forming time of 1, as shown in Fig. 5.3 (a). It results in a similar trend of the corresponding plastic strain, which also increases from 0 at the forming time of 0.2 to 0.1 at the forming time of 1, as shown in Fig. 5.4 (a). The low strain/strain rate values indicate that the data from this region is not plastically deformed severely. In addition, the plastic strain in this region occurs at the late stage after the forming time of 0.2. As shown in Fig. 5.3 (b), for the data from this region, the strain rate ramps up to 1 s-1 between the forming time of 0 and 0.7, followed by a sharp increase to almost 20 1 s-1 at the end of forming. As shown in Fig. 5.4 (b), the elements thus experience low strain level that is less than 0.05 before the forming time of 0.7, and a sharp increase up to 0.4 at the end of forming. This indicates that most of the plastic deformation of the material from this region occurs at the end of the forming process, and high rate loading may occur in these elements. As shown in Fig. 5.3 (c), the strain rate of the elements in group

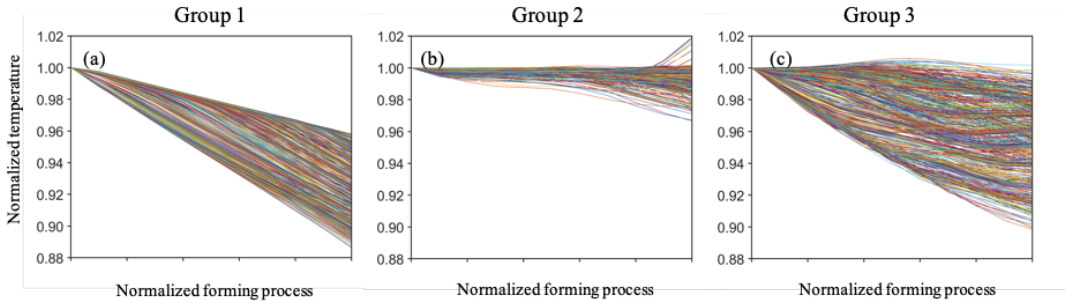


Figure 5.5: Example of data used in physical-based classification model research. Normalized temperature of raw data are illustrated along the normalised forming process, showing different patterns with various geometric locations.

3 increases from the initial stage, keeps at the plateau of approximately 5 s-1 at the end of the forming process. The plastic deformation of these elements thus occurs from the initial stage, showing a smooth ramp-up to a plastic strain of 0.25 and suggesting that most of the plastic loading uniformly distributed from the forming time of 0.2 to 1.

Fig. 5.5 (a), (b) and (c) show the evolution of normalised temperature against normalised forming time, and the normalised temperature of all elements decreases from the normalised temperature of 1. In data group 1, as shown in Fig. 5.5 (a), the temperature of the data from this region shows a relative steady-state decrease during the whole process and drop into a normalised temperature range between 0.88 and 0.96. It indicates that the elements in this region are under a relative stable contact condition. For group 2, the temperature data only have a slight drop, and the main temperature drop happens from the forming time of 0.7, which indicates that the heat transfer in this region is low. Accounting for the large deformation at the end of the process, the normalised temperature of some data shows a sharp increase from 1.0 at the forming time of 0.8 to 1.02 at the forming time of 1. The temperature data of the group 3 is illustrated in Fig. 5.5 (c), the normalized temperature drops to a range between 0.9 and 0.99. The various final temperature levels result from the different starting points of temperature. The data drop either at the beginning or after a stable stage, which indicates that the transit stage exists in this region during the process.

Evolutions of normalised major stress against forming time are presented in Fig. 5.6 (a), (b), (c). In the data group 1, the stress state of the data shows a near-axisymmetric distribution,

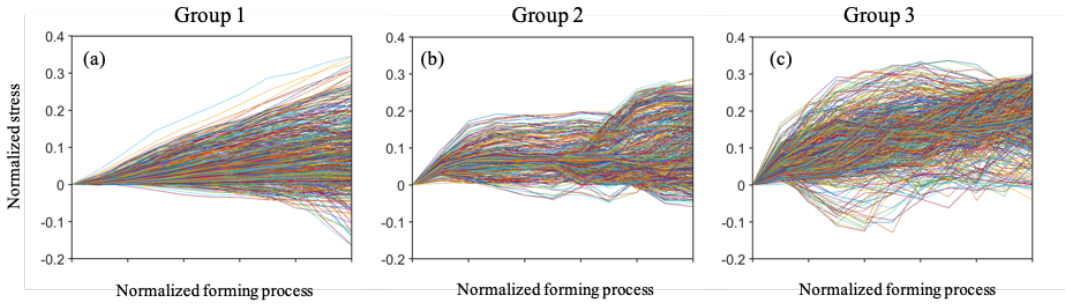


Figure 5.6: Example of data used in physical-based classification model research. Normalized major stress of raw data are illustrated along the normalised forming process, showing different patterns with various geometric locations.

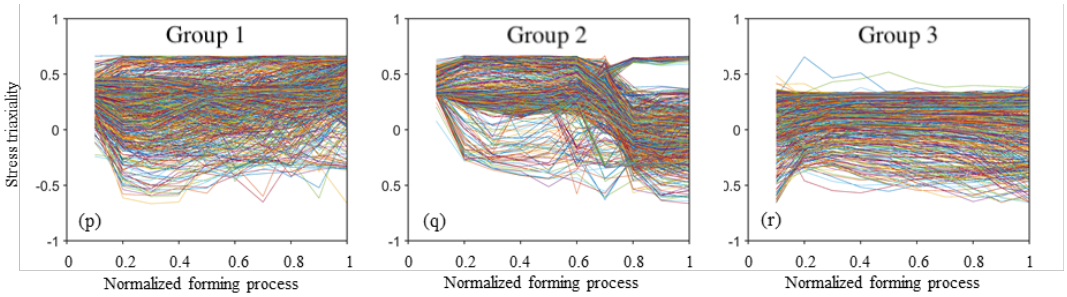


Figure 5.7: Example of data used in physical-based classification model research. Stress triaxiality stress of raw data are illustrated along the normalised forming process, showing different patterns with various geometric locations.

i.e. 30% of the data are negative up to -0.5, indicating a near-linear compressive loading state, whilst 70% of the data are positive up to 1.5, suggesting a near-linear tensile loading state. The deviation between the compressive and tensile stress states becomes pronounced at the end of the forming process, leading to a triangular-shaped data distribution. Fig. 5.6 (b) shows a steady tensile loading with a major stress between 0 and 1 at the initial stage of forming from 0.1 to 0.8, followed by a wider spread tensile loading at the final stage of forming from 0.8 to 1. The stress data in group 3 exhibit a phenomenon opposite to that in group 2. The major stress has a wide spread at the initial stage of forming from 0.1 to 0.8, ranging from -0.5 to 1.5 of the normalised value, followed by a steady tensile loading that 91% of the data has a major stress from 0.5 to 1.5.

Evolutions of stress triaxiality against forming time are presented in Fig. 5.7 (a), (b) and (c). As shown in Fig. 5.7 (a), the stress triaxiality data in the group are mainly retained in the range of 0 to 2/3, indicating that the elements are under the bi-tensile condition or tensile-dominated tensile-compressive condition. For data group 2, the stress triaxiality illustrates a

significant transit stage from the range between 1/3 and 2/3 to another range between -2/3 and 1/3, as shown in Fig. 5.7 (b). It suggests that the elements change from the bi-tensile condition to (bi-)compressive-dominated tensile-compressive condition. As shown in Fig. 5.7 (c), the stress triaxiality data in this region indicate a near-axisymmetric distribution in the range from -0.5 to 0.4, indicating that the elements are at various stress states, including bi-tensile, tensile-compressive and/or bi-compressive condition. 70% of the data are positive from 0 to 0.4, indicating a tensile-dominated condition, while 30% of the data are negative from -0.5 to 0, indicating a compressive-dominated condition.

The origin of the data group 1 is the blank holding area. The contact pressure at the initial stage of forming is stable and low due to that the sharp increase of the blank holding force at the final stage of forming is caused by the tendency of wrinkling leading to localized thickening and increase in pressure. All these characteristics are shown in Fig. 5.2 (a) with clear evidence of plastic deformation caused by wrinkling shown in Fig. 5.3 (a) and Fig. 5.4(a). The radial stress data in the blank holding areas are at the tension state while the hoop stress data in the blank holding areas are at the compressive state, leading to potential wrinkling in this region, which becomes more pronounced at the end of the forming process. In addition, the near-linear temperature drops shown in Fig. 5.6 (a) is caused by the constant interfacial heat transfer between the workpiece and the die. At the end of the forming process, a more pronounced deviation in temperature distribution is caused by greater differences in contact pressure.

The origin of the data group 2 is the die bottom area. This could be identified from the data distribution, showing double-peak features (Fig. 5.2 b) in the contact pressure, i.e. the first peak of contact pressure could be attributed to the initial contact being made between the punch and workpiece, and the second peak could be caused by the forming of embossed/deep pocket features and the die closing force. The discontinuous contact pressure at the intermediate stage could be caused by the insufficient blank holding forces. Moreover, the data from this region show large plastic strain and strain rate at the final stage of forming. This could be corresponding to the forming of the embosses/deep pockets, as shown in Fig. 5.3 (b) and Fig. 5.4(b). Fig. 5.5 (b) shows the evolutions of equivalent stress.

The origin of the data group 3 is be the side wall area. This can be identified by the wide spread distribution of major stress shown in Fig. 5.6 (c) and uniform distribution of strain rate shown in Fig. 5.3 (c) at the forming process from 0.2 to 0.8. The side wall area experiences bending and unbending processes when it is drawn into the die cavity, which determines the starting point of this deformation process. Once the forming process starts, the side wall elements are continuously drawn into the die cavity, leading to various stress evolutions. This transient contact condition also proves the phenomena found in Fig. 5.7 (c), i.e. severe oscillation pattern of contact pressure. As shown in Figure l, the temperature drop also are in between the blank holding area and die bottom area. The complex stress states are due to the curvature of the die shoulder. A convex curvature could lead to a tensile-dominated stress-state on the side wall, while a concave curvature results in a compressive-dominated condition. The comprehensive analysis of these thermo-mechanical behaviours of the elements from three different data group showed that the temperature, major strain and stress triaxiality are the most pronounced features, which are used as the dominant parameters in the modelling work. Fig. 5.8 shows the detailed stress state evolution data of finite element, the x-axis and y-axis representing the load parameter and stress triaxility, respectively.

With a large number of features, the filtering model can be computationally expensive and tends to overfit, resulting in their performance degenerating. Some features cause the noise and potentially damage the model. To address the problem of the curse of dimensionality, dimensionality reduction techniques have been studied. Feature important analysis is widely employed technique for reducing dimensionality among practitioners. A small subset of the relevant features from the original ones according to linear model regression. By removing those unimportant features, the model may generalize better with lower computational cost and better model interpretability. One such approach-based on the random forest feature importance analysis was demonstrated to be highly effective for determining key physical factors that control the complex phenomenon through the identification of simple thermo-mechanical behaviour. The random forest feature importance analysis has been shown to be enormously effective at predicting the preferred parameters during the hot stamping process, as shown in Fig. 5.9. For all the stress regions, major strain, normalised temperature and stress triaxiality

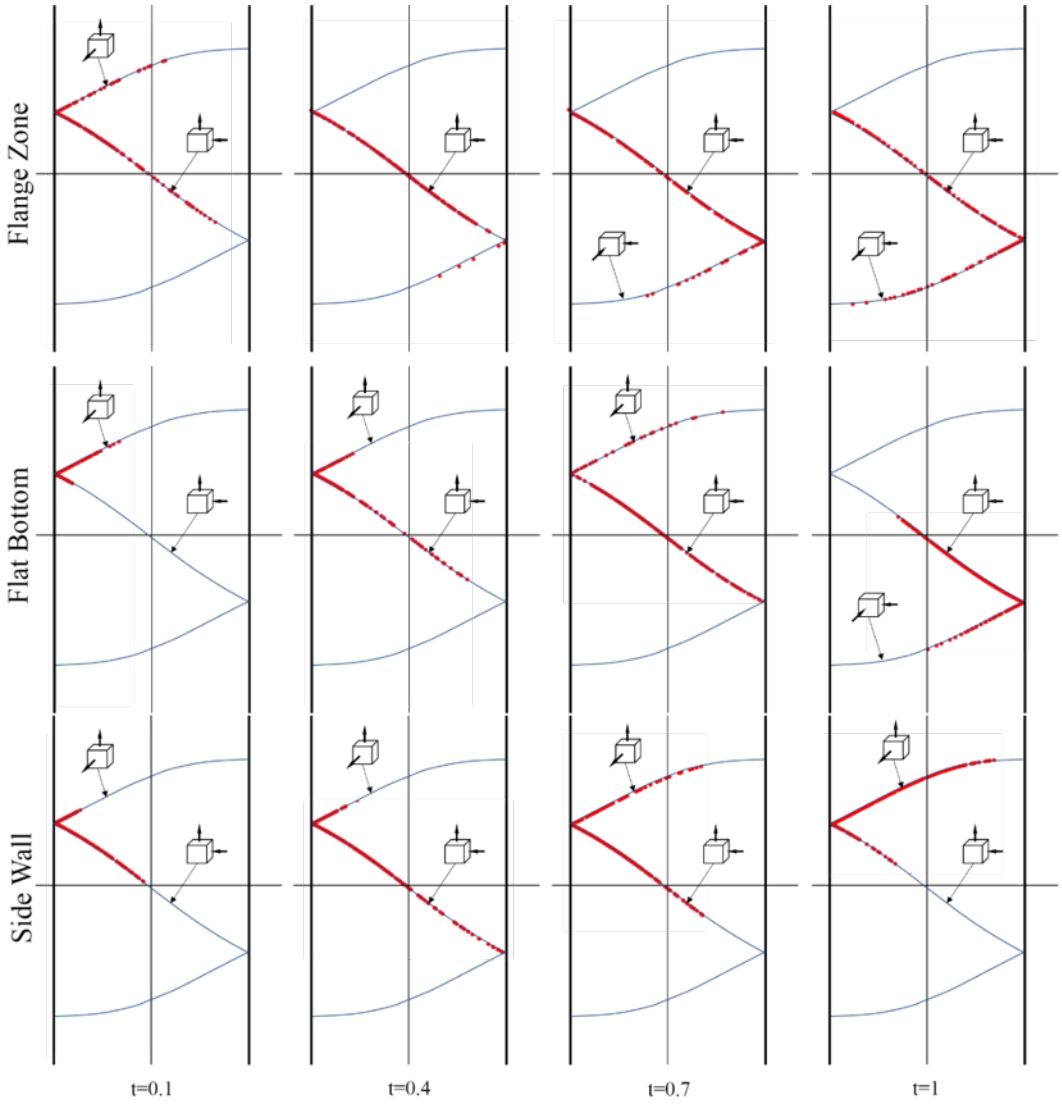


Figure 5.8: Stress state evolution data of finite element used in physical-based classification model research, showing the load parameters and stress triaxiality with different geometric features in sheet metal forming processes

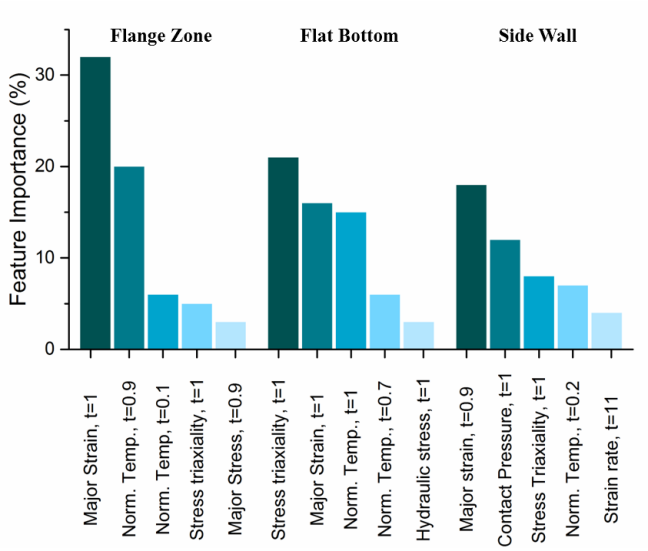


Figure 5.9: Random forest based feature importnace analysis

are the most important parameters among all the features.

5.4.2 Development of model

A governing model is used to develop the evolutionary algorithm, as shown below:

$$\int G_t F_t dt = 0 \tag{5.18}$$

where G_t, F_t are functions depending on the normalised time of the stamping process. G_t is the process which is given by:

$$G_t = \frac{1}{A\sqrt{2\pi}} e^{-\frac{(t-t_f)^2}{2A^2}} \tag{5.19}$$

F_t is the criteria factor shown as:

$$F_t = f - f_c \tag{5.20}$$

It is then rearrange into

$$\int \frac{1}{A\sqrt{2\pi}} e^{-\frac{(t-t_f)^2}{2A^2}} (f - f_c) dt > 0 \tag{5.21}$$

f_c and t_f are the two key parameters to separate the data from the desired region, parameter factor and time indicator, respectively, by maximizing the information gain (IG). Information gain is the entropy reduction when transforming a dataset, which is calculated by comparing

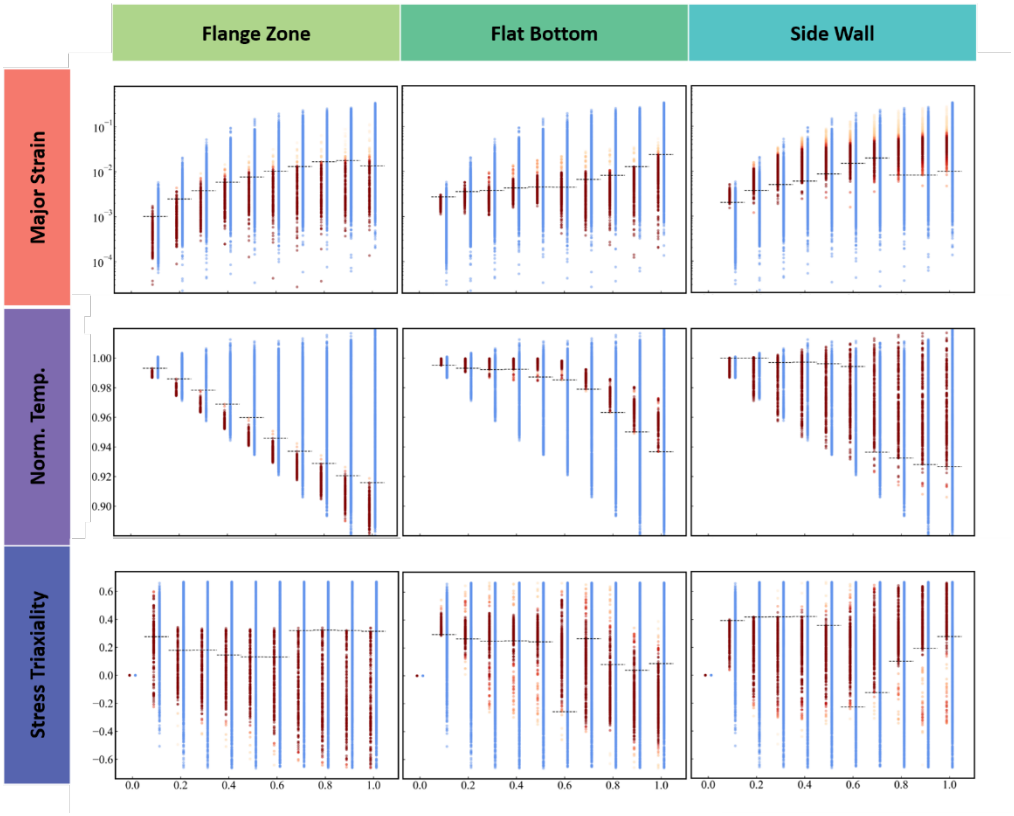


Figure 5.10: Discrete fitting result of major strain, normalised temperature and stress triaxility for blank holding area, flat bottom and side wall region, respectively

the entropy of the dataset before and after a transformation, which is defined as follows:

$$IG = IG - \frac{N_{cut}}{N} I(D_{cut}) - \frac{N_{rem}}{N} I(D_{rem}) \tag{5.22}$$

where I is the gini impurity, which is the probability of incorrectly classfying a randomly chosen element in the data set. D, D_{cut} and D_{rem} are the full part, cut part, and remaning part of the data set.

$$G = \sum_{i=1}^{n} p(i)\,[1 - p(i)] \tag{5.23}$$

where c is the total class, $c = 2$, in this case, $p(i)$ is the probability of picking a datapoint with class i. Minizing the gini impurity after cutting. Discrete fitting results were obtained by maximizing the information gain from three important features: normalised temperature, major strain, stress triaxiality. In Fig. 5.10 red dots represent the target zone, blue dots represent the remaining of the data.

From time step 2, t2, from each time step, the criteria fc is determined by maximizing the

information gain. To summarize the accuracy for each step, a best- univariate combination is obtained. A bi-univariate combination is also calculated to maximizing the total information gain through 2 individual variables.

5.5 Results and discussion

Fig. 5.10 shows the discrete fitting results of major strain, normalised temperature and stress triaxility for the blank holding area, the flat bottom and the side wall region, respectively. For the blank holding area, uni-variable algorithms using temperature at 0.9 normalised time, major strain at 1 normalised times and stress triaxiality at 0.1 normalised time, with an accuracy of 85.6%, 79.8%, 66.7% and 63.75% respectively. For flat bottom, uni-variable algorithms using stress triaxiality at 0.9 normalised time, temperature at 0.9 normalised time, major strain at 1 normalised time, with an accuracy of 71.6%, 79.2% and 71.5%. For side wall, uni-variable algorithms using major strain at 0.7 and 0.2 normalised time, stress triaxiality at 1 normalised time, with an accuracy of 80.2%, 71.1% and 65.0%. For multi-variable algorithms, the blank holding area was filtered by using final temperature, temperature drop ratio and major strain with an accuracy of 95.4% Flat bottom is filtered by using final stress triaxiality, initial major stress and temperature drop ratio with an accuracy of 92.3%. Side wall is filtered by using the final variation of stress, temperature at 0.2 normalised temperature and final stress triaxiality with an accuracy of 85.1%.

Table 5.2: Model parameter obtained from uni-variate model

Geometric location	No	Variable	tf	fc	Single-variate accuracy	Multi-variate accuracy
Blank holding area	1	Temperature	0.9	0.9205	85.6%	95.4%
	2	Major strain	1	0.014	66.7%	
	3	Stress triaxility	0.1	0.287	79.3%	
Flat bottom	1	Stress triaxility	0.9	0.0788	71.6%	92.3%
	2	Temperature	0.9	0.9539	79.2%	
	3	Major strain	1	0.0597	71.5%	
Side wall	1	Major strain	0.7	0.0201	80.2%	85.1%
	2	Major strain	0.2	0.0031	71.1%	
	3	Stress triaxility	1	0.246	65.0%	

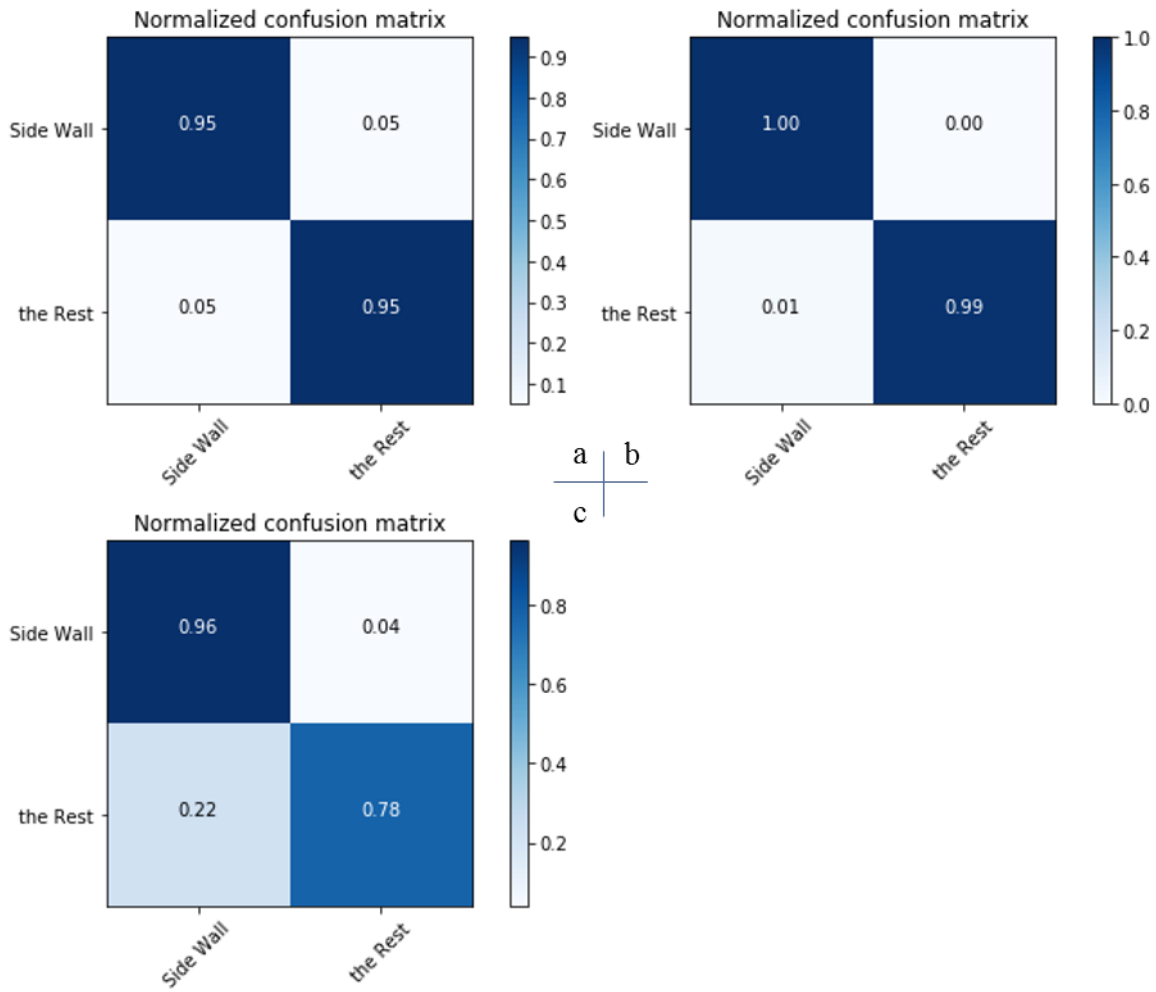


Figure 5.11: Confusion matrix results of classification algorithms for (a) blank holding area, (b) flat bottom and (c) side wall regions, respectively

In this section, a theoretical framework was developed for data processing for the extraction of insightful information from vast volumes of information-absent finite element data of high temperature sheet metal forming processes. The framework is consisted of data pre-processing, data filtering and data visualization algorithms. The proposed data processing framework is an efficient tool for analysing vast volumes of information-absent finite element data, providing insightful information with respect to different regions of the product. The following conclusions can be drawn:

- Three main typical thermo-mechanical features were found in a high temperature sheet metal forming process, representing three typical geometrical features of the components, blank holding area, side wall and flat bottom area. Three thermo-mechanical evolutionary algorithms were developed to enable geometrical characterization of these geometrical

features in the absence of spatial or visual data.

- It was found that a strain univariate algorithm was rigorous in recognizing the blank holding area with an accuracy of 95.4%. By utilising the evolutions of strain, strain rate and temperature, a time-dependent multivariate algorithm was able to successfully identify the side wall and die bottom areas with accuracies of 85.1% and 92.3%, respectively. Moreover, the performance of the multivariate algorithm was increased by introducing stress states, such as the Lode parameter and stress triaxiality. Furthermore, the modelling framework and methodology in this research could be used as a protocol to analyse other forming processes.

Chapter 6

Development of a data visualisation technique

6.1 Summary

Research in metal forming processes has traditionally followed the convention of validating hypotheses with repeatable experimental trials. The accuracy of FE analysis is significantly dependent on the material characterisation, as well as definitions of boundary conditions, and the reliable characterisation of boundary conditions remains challenging, which can be partly explained by the fact that the real boundary conditions in metal forming processes are not well understood. The variables of coefficient of friction (COF) and interfacial heat transfer coefficient (IHTC) were studied as these are two of the most important boundary conditions in finite element analysis for sheet metal forming processes. COF affects the variation in stress distributions, lubricating conditions, die surface characteristics and homogeneous deformation across the contact area between die, punch and blank. IHTC is also a parameter of vital importance in sheet metal forming at elevated temperature to determine the cooling rate and the post-form strength when optimising the forming condition. For both of these variables, throughout the tool surfaces, the contact pressure, relative sliding velocity and distance, and experienced temperature vary over the duration of forming process thus presenting significant

challenges in modelling this behaviour using conventional mathematical models. The workpiece-tool interfaces at different regions, such as the blank-holding area, die radius and die cavity areas, also have different friction coefficient and wear conditions. Therefore, there is a clear need for analyses of the evolution of these boundary conditions to establish a relationship between fundamental tests and metal forming processes to improve the effectiveness of experimental testing and wear modelling.

6.2 Introduction

The data processing technique to optimise a process and to understand large data sets are widespread in industries such as manufacturing engineering (Kwon et al., 2014; Lee et al., 2013), healthcare(Khoury and Ioannidis, 2014) and finance(Preis et al., 2013), but their utility in the metal forming research has been limited. Finite Element (FE) analyses have been widely used in the automotive and aerospace industries to simulate material behaviours of the products during forming processes and to design optimal metal forming strategies by utilising constitutive equations, boundary condition models, which creates an opportunity for the vast amounts of data generated in FE simulations to be processed in a variety of forms. Mining the information generated from experimentally verified FE models can be a promising approach to obtain a deeper and broader analysis and understanding of the real metal forming processes. It also enables data-driven decision making, which refers to the practice of basing decisions on the analysis of data rather than purely on intuition. Data-driven approaches can therefore be used to build testing matrices for experiments based on the analysis of data from FE models. Figure 6.1 shows how data may be processed in the context of closely related sheet metal forming processes. Such an approach could be used to more accurately determine characteristics of boundary conditions during forming processes such as aluminium hot stamping.

Based on a database of experimentally verified finite element simulations, this chapter introduces tribo-maps presenting the distributions and variations of the contact conditions at workpiece-tool interfaces of hot aluminium stamping processes. The complexity of a physical

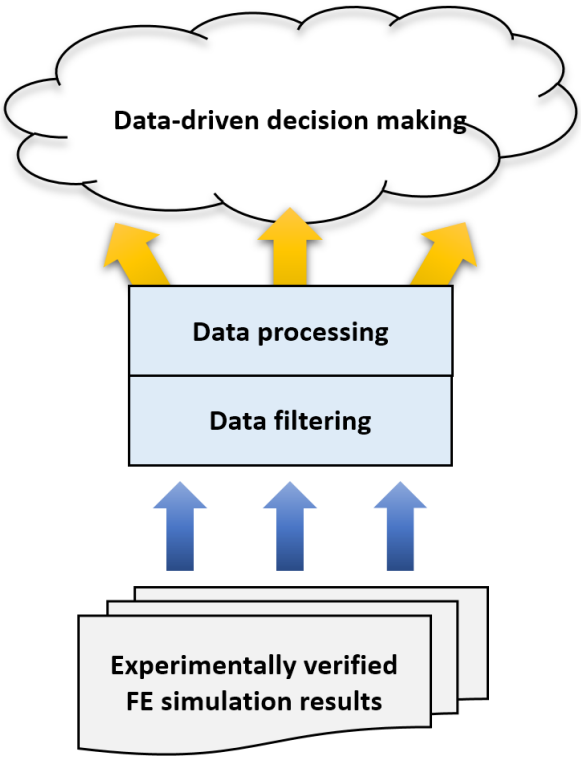


Figure 6.1: Data processing in the context of closely related processes of in data-driven decision making in sheet metal forming research

model describing the interaction between the tool and blank material, contact pressure, temperature, sliding velocity and sliding distance for each region of a component necessitates these data-driven methods to be adopted to identify correlations and characterise materials, and thus to propose specific test conditions for conducting experimental work. Exploiting and analysing the existing data on stamping processes would increase the effectiveness of experimental testing, the accuracy of friction and wear tests and subsequently developed models.

6.3 Tribological Data processing for hot stamping of aluminium alloys

The data processing technique is introduced in this chapter, which reveals the contact condition evolution for a large database of experimentally verified sheet metal forming processes, which is expected to provide a clear guideline for tribological tests for this technique. The basis for understanding the tribological behaviours of hot stamping processes include the contact pressures,

relative sliding velocity, relative sliding distance, and temperature differences between tool and workpiece, quantifying the uneven distribution of the contact conditions in space and time. Thus, the first stage involves extracting the related data of the stamping process from each experimentally verified FE simulation. The database comprises existing FE simulation results from previous studies at Imperial College London and the partners from various projects. The FE models developed in PAM-STAMP and AUTOFORM were verified by the real components formed by in-house forming facilities at Imperial College London and industrial partners by the thickness distributions or strain distribution, and blank temperature drop evolution. The tribology-related database includes the X, Y, and Z coordinates, contact pressure and temperature of each element on the blank and the forming tools, at each computational step of the stamping processes. The forming parameters including the stamping speed, blank holding force, stroke, initial blank temperature as well as the computational time step for each simulation were also obtained. The processing method is introduced in detail in the following section. The processed data were used to generate the probability distributions to provide an overview of the interfacial conditions, and comprehensive contact condition evolution, including the probability and temperature difference as a function of the relative sliding distance, are presented.

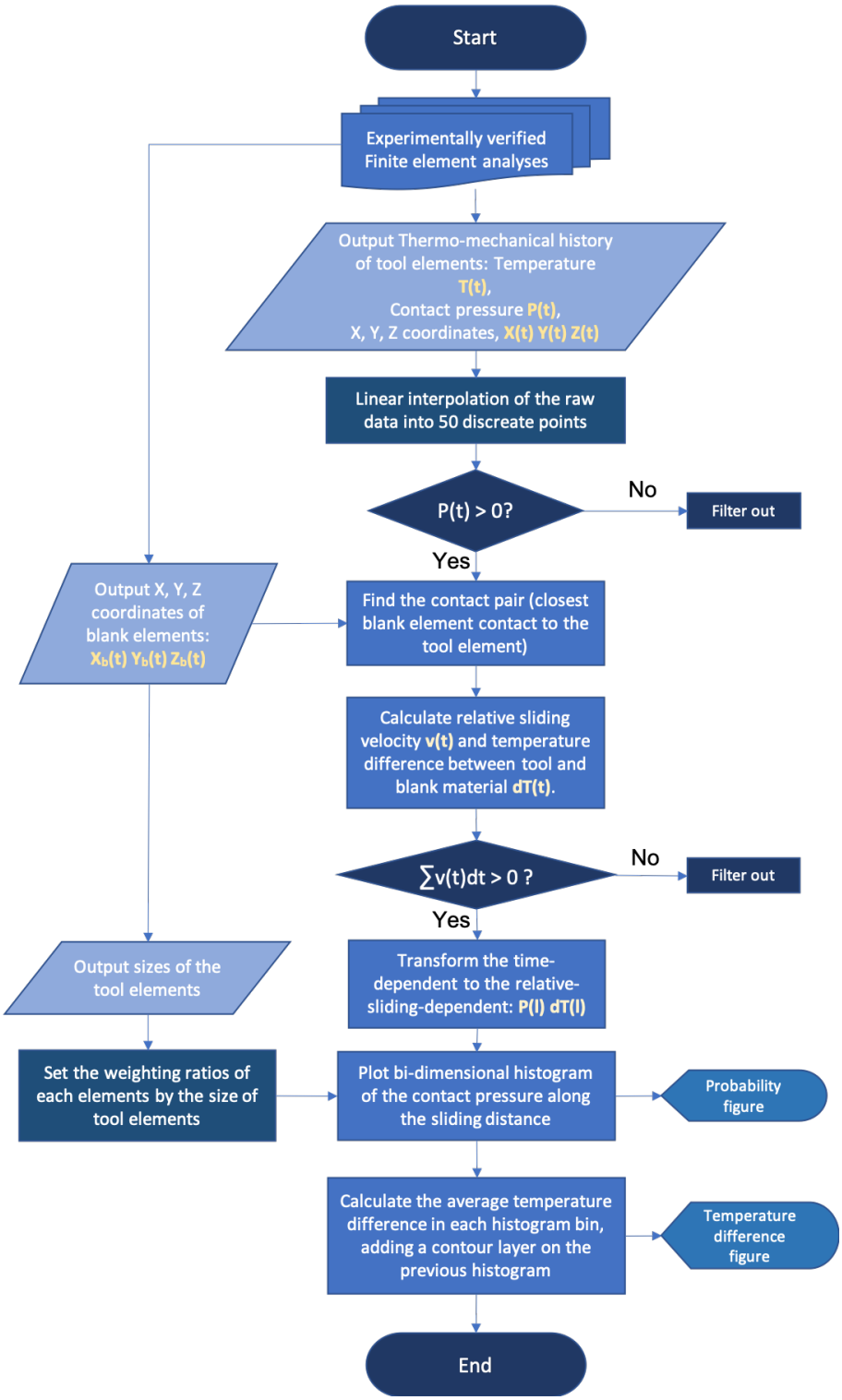


Figure 6.2: Tribological data processing procedure

6.3.0.1 Temperature difference and relative sliding

Contact pressure, relative sliding velocity/distance and temperature difference are the most important information for tribological characterisation of a sheet metal forming process. However, unlike contact pressure, which can be directly output from the FE simulation software, the relative sliding velocity/distance and the temperature difference between the tool and blank elements required further calculations. In order to obtain this information, this chapter provides a simple method to identify the contact relationship between the blanks and the forming tools during the hot stamping process. For each tool element at any stage of the stamping process (excluding the first and final stages), if its contact pressure is non-zero, the distances to all of the blank elements are calculated to determine its nearest blank element. The tool element and the corresponding nearest blank element can then be regarded as a contact pair (Eq.6.1. As shown in Figure 6.3, at Stage N, the two elements from the tool and blank, respectively, is a contact pair.

$$minf(e,b,nearest) = \sqrt{(x_{b,e} - x_{t,n})^2 + y_{b,e} - y_{t,n}))^2 + (z_{b,e} - x_{t,n})^2} \tag{6.1}$$

subject to

$$n \in \{1, 2, 3, 4, ...\text{tool element number}\}$$

where e is the number of the blank element, x, y, z are the X, Y, Z coordinates and the subscripts b and t refer to the blank and tool. *f(e,b,nearest)* denotes the vector $(x_{b,e}, y_{b,e}, z_{b,e})$.The temperature differences between the blank and each tool element can subsequently be obtained:

$$\begin{cases} \Delta T_{t,n} = T_{e,b_{nearest}} - T_{t,n}, & \text{if } P_{t,n} > 0 \\ \Delta T_{t,n} = 0, & \text{if } P_{t,n} = 0 \end{cases} \tag{6.2}$$

By using the X, Y, Z coordinates of the blank and tool elements, the relative position changes between the contact pair from one stage to another can be used to calculate the corresponding relative sliding velocity and relative sliding distance, shown in Figure 6.3, and Eq. 6.3 and Eq.6.4.

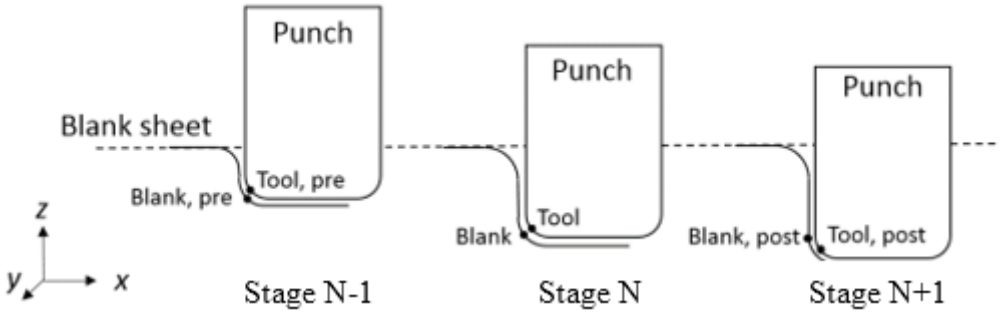


Figure 6.3: Schematic of relative sliding velocity calculation

$$\begin{cases} v_s = \frac{1}{2} v_{post}, & \text{for } s = s_i \\ v_s = \frac{1}{2}(v_{pre} + v_{post}), & \text{for } s_i < s < s_f \\ v_s = \frac{1}{2} v_{pre}, & \text{for } s = s_f \end{cases} \tag{6.3}$$

$$l_{t,n} = \sum v_{t,n} dt \tag{6.4}$$

where s is the normalised time step, s_i is the initial time step, s_f is the final time step.

6.3.0.2 Filtering and weighting technique

Due to the existence of noisy data in each FE simulation, filtering is required to select the most relevant results for tribological characterisation of the forming process. For example, there may be regions of the material that do not experience any sliding and that could skew the data analysis. Furthermore, if the FE results are analysed without weightings, each element from every FE simulation would have the same level of contribution to the data analysis as any other element. This assumes that each element has an equal probability of existing in a hot stamping process, whilst in reality the data size of each simulation file varies dramatically across different studies. When the distortion caused by a large simulation file affects the combined dataset significantly, then weighting is necessary to account for sample bias before the integration of it with the dataset.

6.3.0.3 Sliding-based database and normalised wear distance

Using the two data processes above, the contact pressure, temperature difference, relative sliding velocity and accumulated relative sliding distance of each tool element at each stage of the entire hot stamping process could be obtained. However, the time-based contact data does not reflect a tribological process correctly as not all of the tool elements slide against the blank throughout the whole forming process. The elements at the edge of the blank-holding area may only undergo sliding at the initial stages of stamping, while the elements in the die cavity may only experience sliding at the final stages. In order to have a deeper understanding of the contact condition evolution of the tool elements, the contact conditions were studied in relation to the accumulated relative sliding distance. The time-based contact condition was thus transformed into a sliding-based one, where the contact pressure and temperature difference of the tool elements were interpreted according to the sliding distance.

However, due to the large range of stamping speeds and strokes used in each study, the investigation could not be conducted with absolute values. A normalised wear distance(NWD) is therefore introduced, which is the ratio between the sliding distance and punch stroke, and is proposed to eliminate the effect of stroke on the wear distance and to also indicate the extent of stretching and drawing in each element (see shown in Eq. 6.5). The closer the NWD value is to 1, the closer the sliding distance experienced by a tool element is to the stroke length, representing the increased material draw-in taking place.

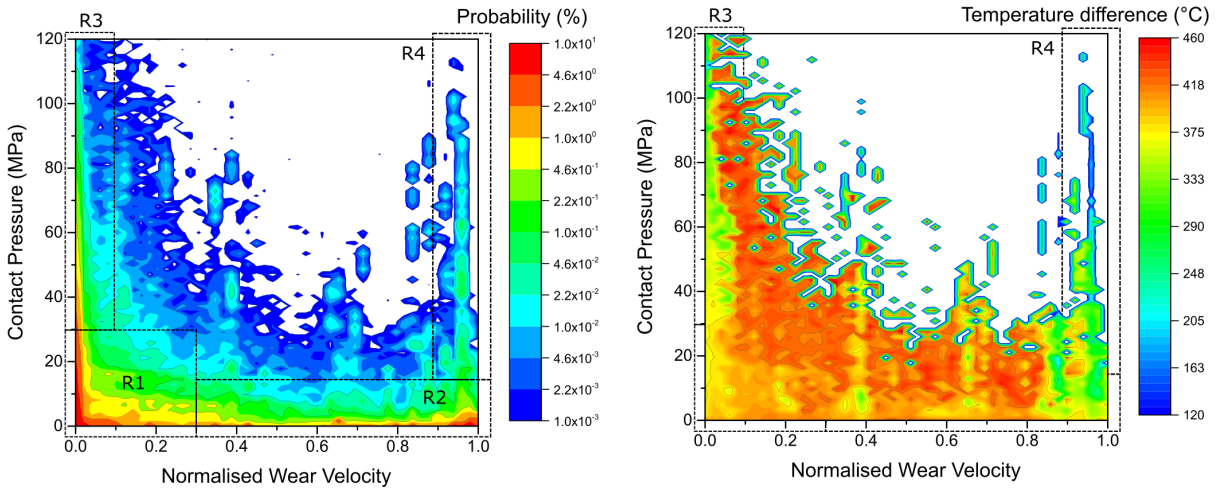
$$\begin{aligned} \text{normalised wear velocity} &= \frac{\text{relative sliding velocity}}{\text{stamping speed}} \\ \text{normalised wear distance} &= \frac{\text{relative sliding distance}}{\text{stroke}} \end{aligned} \tag{6.5}$$

6.4 Results and discussion

6.4.1 Overall contact conditions at tool surface

To standardise the data, the FE simulation results used in the study were all for AA6xxx aluminium alloys under hot stamping conditions, with different configurations. AA6xxx formed under hot stamping processes exhibits complicated contact pressures, relative sliding velocities and temperature differences. Figure 6.4a summarises all the local contact pressure and instant relative sliding velocity in the current database, and shows the probability distribution of the contact pressure and normalised wear velocity on the die surface. The contact pressure varies from 0 to 120 MPa, and 75.1% of the contact conditions were in the range of 0 to 10 MPa. Although the most frequent occurrence can be used to define appropriate friction test conditions, the maximum contact pressure of 120 MPa encountered during hot stamping must also be considered. Figure 6.4b shows the temperature difference as a function of the contact pressure and normalised wear velocity, from which it was found that most of the contact conditions during hot stamping tended to have high temperature differences. 64.8% of the elements experienced a 430-460 °C temperature difference, and the minimum temperature difference was found to be around 120 °C. The average temperature difference in region 3, high-pressure-low-velocity region, and region 4, high-pressure-high-velocity region, was also found to be lower than that in the other two regions.

The distribution can be divided into four main parts. Regions 1 (R1), 2 (R2) and 3 (R3) account for 94.9% of the total interfacial conditions, showing an exponential distribution along the normalised wear velocity, from which it was found that the contact pressure and normalised wear velocity were inversely proportional to each other. The elements experiencing a high contact pressure mostly had a small contact pressure (R3) and vice versa (R2), and this was due to the high frictional forces resulting from the high contact pressures restricting the material flow. An exception to this occurs in the high-speed region at a normalised wear velocity greater than 0.9, where the contact pressure is over 10 MPa and up to 116 MPa, and accounts for 2.5% of the total conditions. This phenomenon typically exists at the die radius area and the



(a) Probability distribution

(b) Temperature difference distribution

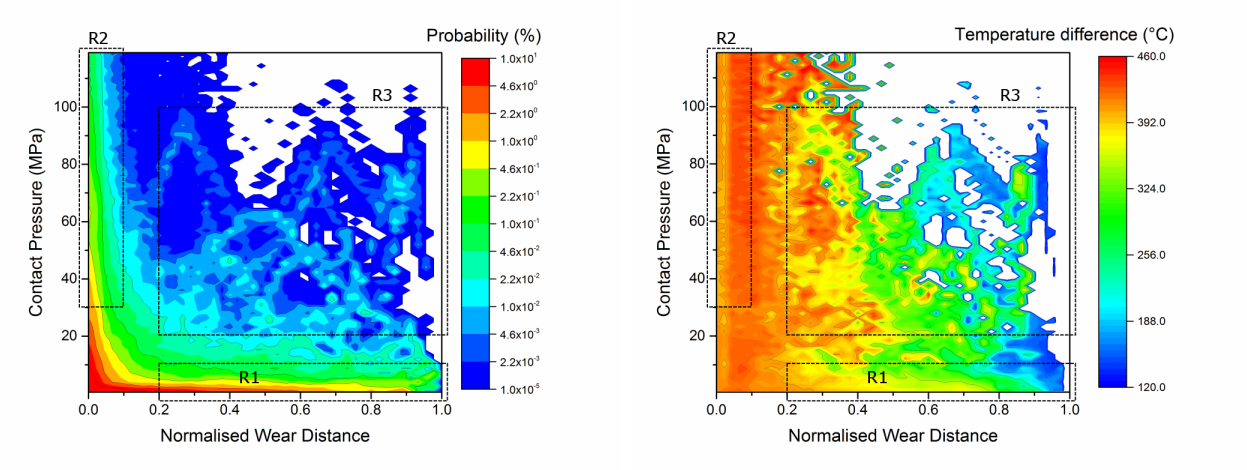
Figure 6.4: (a) Probability and (b) temperature difference distributions as a function of the contact pressure and wear velocity on the tool surface during hot stamping of AA6xxx aluminium alloys

radii of key features, where the relative sliding velocity is close to the stamping speed and the continuous bending process requires a large contact pressure. The temperature difference in Regions 1 and 2 are found to be higher than Regions 3 and 4, which indicates that Regions 3 and 4 usually happened at the later stage of the stamping process.

6.4.2 Contact condition evolution during the wear process at the tool surface

6.4.2.1 Die

Figure 6.5 shows the characteristics of the contact conditions during hot aluminium stamping, in which the contact pressure evolution of all the sliding elements on the die surfaces was plotted against their normalised wear distances. The contour in Figure 6.5a presents the probability distribution and that in Figure 6.5b presents the average temperature difference distribution experienced by the cold die in contact with the hot blank. Most of the elements are located in the L-shape region formed by R1 and R2, where the contact pressure and normalised wear distance are inversely proportional to each other. As described previously, elements with low contact



(a) Probability distribution (b) Temperature difference distribution

Figure 6.5: (a) Probability and (b) temperature difference distributions as a function of the contact pressure and wear distance on the die surface during hot stamping of AA6xxx aluminium alloys

pressures usually experience long wear distances and vice versa, and some elements undergo both high contact pressures and wear distances simultaneously, resulting in the most severe friction and wear conditions. Additionally, the temperature difference between the die and blank reduces during the forming process, and that is increases with increasing contact pressure. Above 20MPa, the temperature difference reduction rate is almost constant, indicating that the interfacial heat transfer coefficient (IHTC) reached its peak value, which was also found by Liu et al. (2017). The contact pressure is a critical parameter determining the heat transfer between the aluminium blank and tool during hot stamping processes. The IHTC gradually increase with increasing contact pressure and reaches a steady-state value at approximately 20 MPa.

The contact condition distribution can be divided into 3 different parts: the draw-in contact region(R1), the tool strike region (R2) and the transient contact region (R3). Region 1 accounts for 64.8% of all the contact conditions. Elements in this region undergo a low and stable contact pressure up to 10 MPa within the NWD range from 0.1 to 0.98, with the blank flowing along the tool surface relatively freely. The contact pressure increases slightly, while the temperature difference experienced by the elements in this region decreases at a relatively low rate due to the low contact pressures. The draw-in contact conditions are typically located on the blank holding area and slide walls. For the elements in the blank holding area, the contact pressure is highly dependent on the blank holding force, while the wear distance is related to the level of

draw-in at different locations in the blankholding area. If the size of the blank is smaller than the tool, the distance to the die edge will affect the wear distance. For the elements on the side wall, the clearance between the punch and side walls determines the contact area and the magnitude of the contact pressure. The contact area will also shift as the blank flows from the blank holding area into the die cavity, causing elements to undergo relative wear intermittently.

Region 2 accounts for 5.1% of all the contact conditions, with elements in this region having relatively high contact pressures from 30 to 120 MPa, but an extremely short NWD of up to only 0.1, with over 90% of the elements having a NWD of less than 0.02. This part of the tool only has extremely short relative wear with the hot blank. For the elements undergoing a contact pressure higher than the flow stress of aluminium at elevated temperatures, the material flow was locally restricted, with some of the element experiencing hydrostatic pressures. The temperature difference between the elements also remained at a high level in this region due to the high contact pressures. The high contact pressures may have been caused during the forming of complex features in the die, such as pocket regions, leading to high levels of localised deformation and local work hardening of the material. These elements only experience wear at the very end of the stamping process. In addition to the die cavity, the blank material at the punch radius would also show this type of tribological behaviour.

Region 3 accounts for 10.1% of all contact conditions, where the elements experienced both a large contact pressure and a long normalised wear distance. In this region, the normalised sliding distances of the elements are slightly shorter than the draw-in contact region, and the contact pressures are lower than tool stroke region, varying from 20-100 MPa and always lower than the material flow stress. According to Pereira et al. (2009), s steady-state contact pressure response exists for the deep drawing of steel at room temperature. However, here the contact pressure gradually increases during the process. This is mainly caused by the temperature decrease and consequent strength increase of the aluminium sheet blank, and is determined by the forming speed and blankholding force used in the forming process. For example, at a low forming speed, usually below 100 mm/s, the temperature drop is much more significant. This typical tribological behaviour usually occurs at the die radius area, where the material flow relatively freely and intensive bending and straightening occur, which also makes this the most

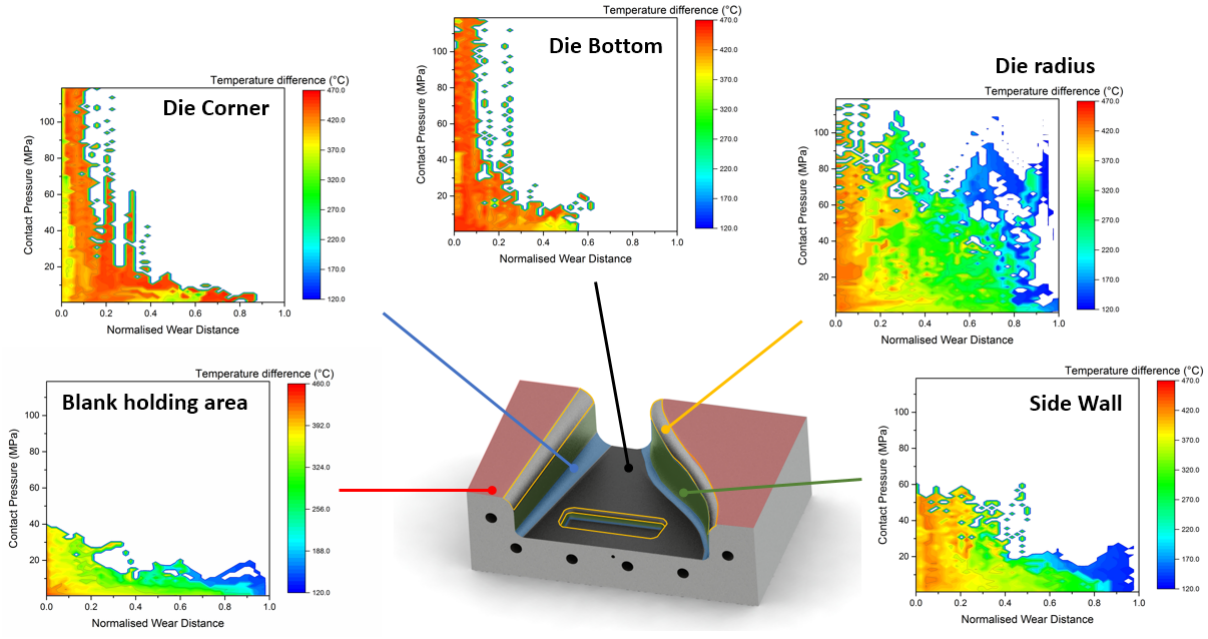
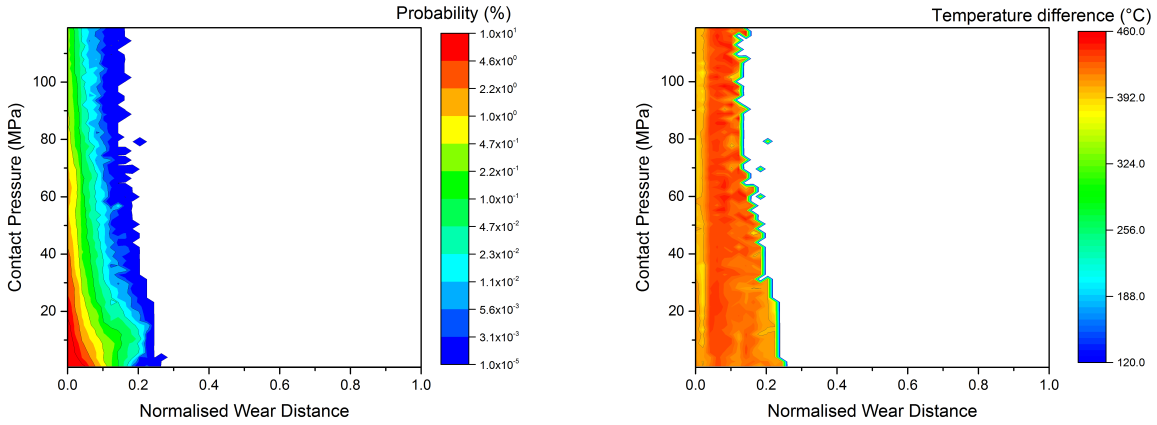


Figure 6.6: filtered visualisation of tool life prediction

worn region of the tool. The variation of the contact pressure range is mainly caused by the design of the die geometry Eriksen (1997). Fig. 6.6 summarised all the sliding conditions on the die surface.

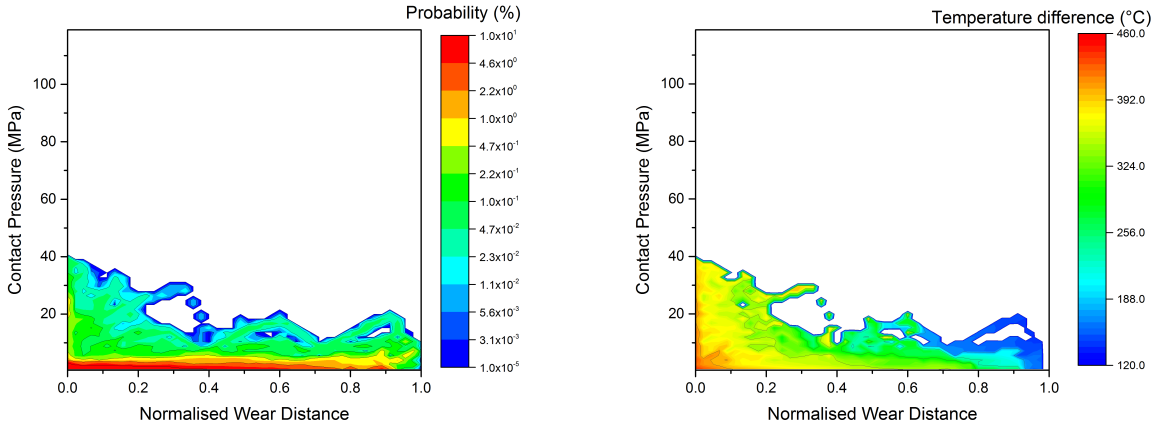
6.4.2.2 Punch, blankholder, and die with drawbeads

Figures 6.7 and 6.8 illustrate the contact pressures of all sliding elements on the surfaces of the punch and blankholder, respectively, as a function of the normalised wear distance, with contours representing the probability and temperature difference distributions. It can be seen from Figure 6.7 that for the punch, most of the elements are located at the short normalised wear distance region, where the contact pressure varied from 0-120 MPa, and the temperature difference remained at a high level of approximately 460 °C. For some of the elements with a normalised wear distance of less than 0.02, the sliding process occurs with relatively low temperature differences. Those elements typically occur at two parts of the punch; the flat end, where during the stamping process the material is bent by the punch radius and the flat end of the punch does not fully contact the blank material until the die is fully closed. The second part is located at the regions of the punch furthest from the blank, and only experiences sliding



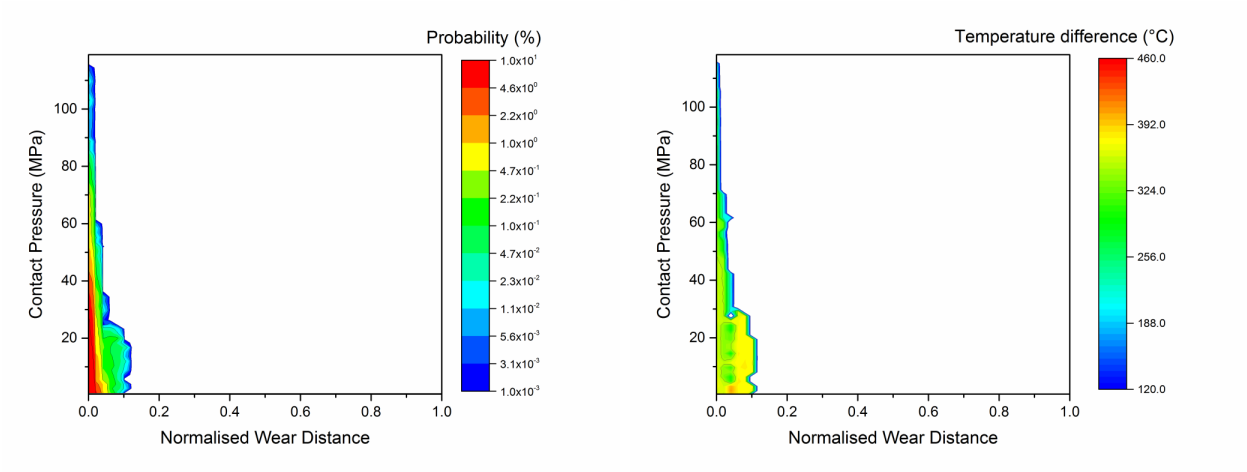
(a) (b)

Figure 6.7: (a) Probability and (b) temperature difference distributions as a function of the contact pressure and normalised wear distance on the punch surface



(a) (b)

Figure 6.8: (a) Probability and (b) temperature difference distributions as a function of the contact pressure and normalised wear distance on the blankholder surface



(a) Probability distribution (b) Temperature difference distribution

Figure 6.9: (a) Probability and (b) temperature difference distributions as a function of the contact pressure and wear distance on the die surface with the drawbead during hot stamping of AA6xxx aluminium alloys

at the very end of the stamping process.

For elements on the blank holders, Figure 6.8 shows that most of them experienced a relatively long normalised wear distance between 0-0.98, and a very small contact pressure of less then 5MPa. The temperature difference also decreased to approximately 300 °C with increasing wear distance. For some of the elements with a normalised wear distance over 0.8, the longer sliding process results in very low temperature differences of about 120 °C, and are typical of low speed stamping processes. The relatively high contact pressures at lower wear distances is caused by thickening and wrinkling at the edge of the blank due to high circumferential compressive stresses.

Figure 6.9 illustrates the distribution of contact conditions on the die surface with a drawbead, showing that with the existence of the drawbead, which effectively restricting the material flow, the normalised wear distances drop to less than 0.1. The contact pressure varied from 0-120 MPa, which is similar to the results obtained from all the other files. The temperature difference is about 380 to 200 °C. This is because that the sliding velocity is slow, while the temperature difference experienced on the die surface kept dropping during the sliding, and an average temperature difference is obtained. For a very slow sliding velocity, the temperature contour can not show the evolution of the temperature in this method.

Chapter 7

Development of data-driven experiment for variable contact conditions

Experiments at realistic test conditions are of vital importance to investigate the boundary conditions in sheet metal forming processes, such as coefficient of friction (COF) and interfacial heat transfer coefficient (IHTC). Constant boundary conditions have been typically applied in the previous studies. However, the boundary condition may actually vary over an extremely short period of time in practical hot stamping processes. This chapter presents a data-driven experimental method developed from the obtained visualisation results, to study the evolutionary process of boundary conditions between aluminium alloy and tool materials in sheet metal forming processes. The experimental setup and key procedures are also included in this chapter.

7.1 Experimental methods of the tribology test

7.1.1 Test material

Aluminium alloy 7075 and tool steel P20 were mainly used in this project. Aluminium alloys 7075 have considerable industry application due to its high strength-weight ratio. P20 tool steel

was a ideally suitable material for production of aluminium die. The lubricant used for the test was provided by Novelis, specially developed for the high temperature stamping process.

7.1.2 Test equipment and setup

This test used a pin-on-disc setup, and Fig. 7.1 illustrates the schematic of a typical pin-on-disc setup, where a pin with a flat or radiused tip subjected to a vertical load slides against a flat circular disk. By applying the concept, a high temperature tribometer has been designed by Anton Paar, as shown in Fig. 7.1(b). The operating temperature range of the tribometer is from room temperature to 1000°C. Independent measurement of normal load and friction force is designed to avoid crosstalk between different force signals. The thermal drift error is minimised by two friction sensors on the friction measurement. Surrounding heating elements combined with water cooling was designed to provide precise and homogeneous sample temperature control. The controllable variables include temperature, contact load, sliding speed and sliding distance. Other technical specifications are listed in Table 7.1.

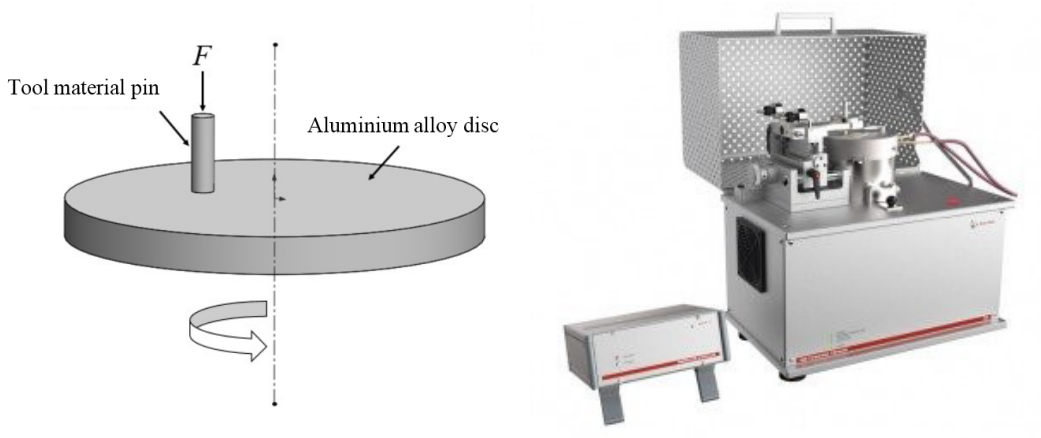


Figure 7.1: Schematic illustration of a pin-on-disc test (left) and Anton Paar pin-on-disc test setup (right)

In order to reproduce the relative sliding condition during the sheet metal forming process, a tool material pin and a workpiece material disk were used, where the tool material always slid against a fresh blank material surface. An aluminium pin is easily worn during sliding process leading to a contact pressure drop. The pin made of tool material can keep its geometry within the controlled sliding distance, allowing a relative controllable contact pressure.

The testing method followed the concept of ASTM G99 *Standard Test Method for Wear Testing with a Pin-on-Disk Apparatus* (2016). No cleaning work is conducted for the pin or disk to reproduce the real forming condition in manufacturing process. In the experimental setup, the disk was rigidly held by the disk holder horizontally, and the pin was secured by a pin holder. Through a adjustable level, the pin is set perpendicularly to the disk. For the lubricant application, a dedicated rig was designed and manufactured allowing precise control of lubricant applied on the pin. The pin specimen was loaded by standard weights. The test machine drives the disk specimen to revolve about the disk center horizontally, causing a circlular sliding path on the disk surface. The coefficient of friction was calculated from the friction force measurement and the normal load.

Table 7.1: Technical Specifications for the Anton Paar high temperature tribometer

Rotation speed	0.3 to 600 rpm
Maximum torque	450 mNm
Friction force range	up to 10N
Friction force resolution	0.03 mN

7.1.3 Results and discussion

The experiments the were performed with a linear sliding speed of 50 mm/s at a wear track radius of 10 mm. Sliding speed was 50 mm/s. Normal loads, 5N and 8N, were used to investigate the effect of contact pressure on the tribological behaviour, and a load increase condition, from 5N to 8N, a load decrease condition from 8N to 5N were tested.

An examination of the effect of contact pressure at 250°C, as shown in Fig. 7.2, demonstrates that the coefficient of friction at full film lubrication did not change while the lubricant breakdown distance decreased from 46 mm to 27 mm when the contact load increased from 5N to 8N. According to the generalised Stribeck curve and the Sommerfeld number, an increase in the contact pressure will lead to a thin lubricant film. In addition, the lubrication mode transfers from full film lubrication to boundary lubrication with the increase in normal loads, which leads to a decrease in load-carrying capacity and early onset of lubricant breakdown. The variable load condition perfectly fit the prediction results from interactive friction model developed by

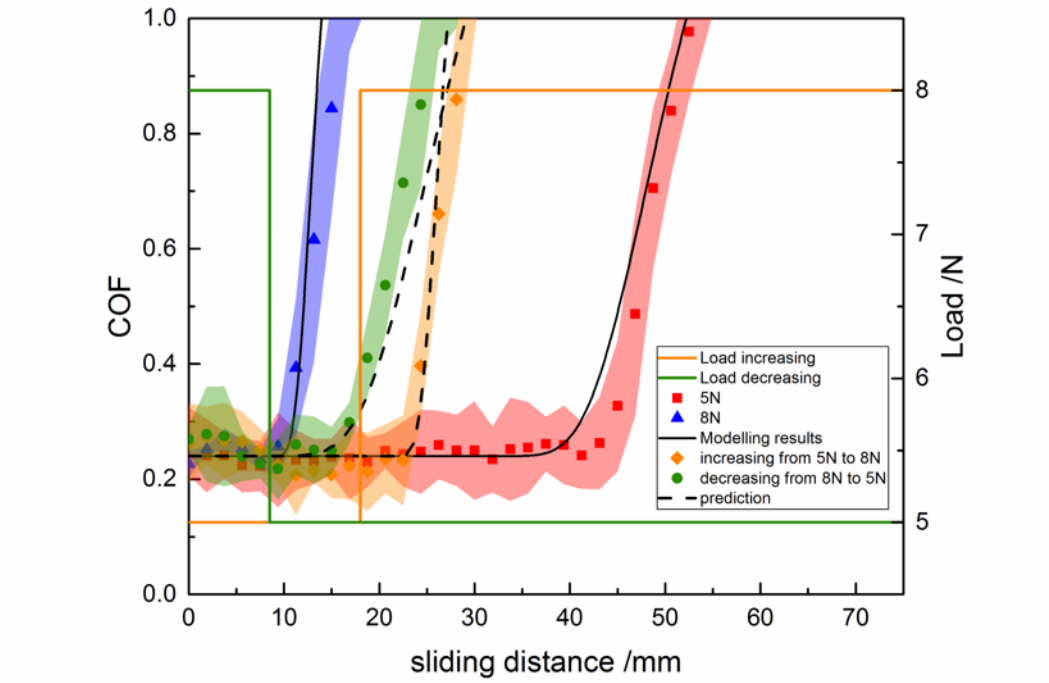


Figure 7.2: Friction test with load jump condition

(Hu et al., 2019).

7.2 Experimental setup of the interfacial heat transfer test

7.2.1 Test material

Aluminium alloy 7075 were mainly used in this project. For the tool material, AlCrN-coated tool substrate sponsored by Schuler was used.

7.2.2 Test equipment

Fig.7.3 illustrates the schematic of the IHTC test facility, which was dedicated designed and manufactured to simulate the stamping processes in a Gleeble 3800 thermo-mechanical simulator (Liu et al., 2017). The left pedestal (1 in Fig.7.3) and the testing frame (3 in Fig.7.3) were fix in the Gleeble 3800 thermo-mechanical chamber as illustrated in Fig.7.4, and the right pedestal was also attached to Gleeble but can move freely in horizontal direction. The die material (2 in Fig.7.3) and punch material were connected to the left and right pedestals, respectively. Two guide pillars (6 in Fig.7.3) were connected to the testing frame, and a insulating block (7 in Fig.7.3) was designed to freely move along the pillars. Two blankholers (5 in Fig.7.3) were then fixed on the insulating sliding block, allowing the workpiece blank (4 in Fig. 7.3) attached to freely move horizontally with the punch stroke. Workpiece blanks were electrical resistance heated up at a heating rate of 10 °C/s through two blank cables attached to the blankholders, as shown in Fig.7.4. The temperature distribution in the workpiece were homogeneous during the heating process. In order to measure the temperature evolution, thermocouples were attached to the die, the punch and the workpiece (3 mm distance to the surface, 12.5 mm deep holes at tool material, center of the workpiece, as shown in Fig.7.4).

Table 7.2: Technical Specifications for Gleeble 3800 thermo-mechanical simulator

Maximum compressive force	20 tons
Maximum stroke distance	125 mm
Minimum stroke rate	2000 mm/sec
Maximum temperature	3000 °C
Maximum heating rate	10000 °C/s

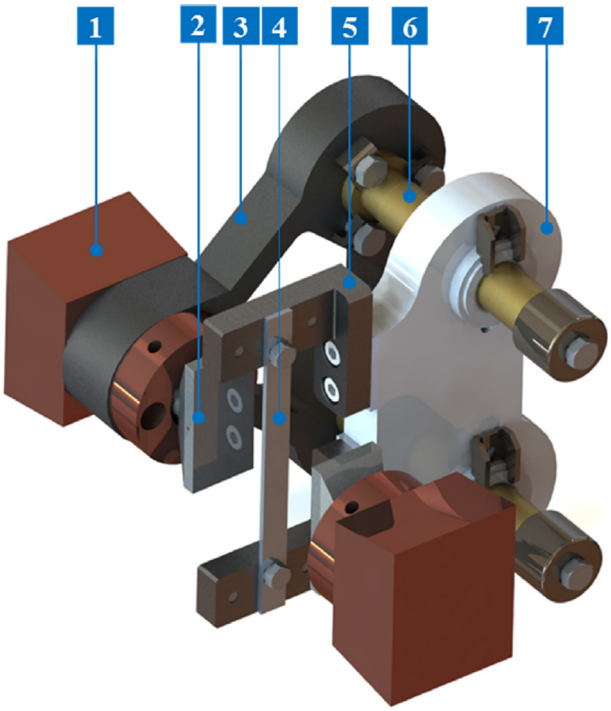


Figure 7.3: Schematic of the IHTC test facility, including (1) a pedestal, (2) a die, (3) a frame, (4) a workpiece, (5) two blankholders, (6) two guide pillars and (7) insulating sliding block

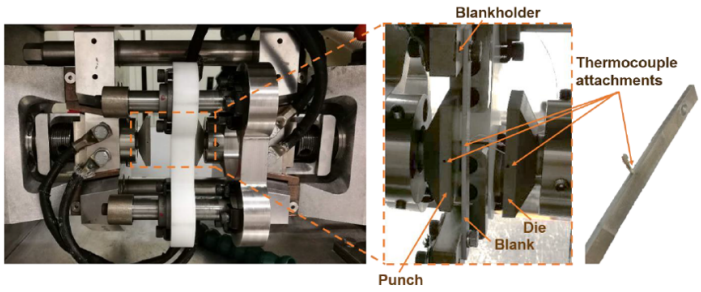


Figure 7.4: IHTC experimental setup in Gleeble

7.2.3 Results and discussion

By using the data-driven approach, distributions of the contact pressure and contact area between workpiece and tool during the stamping process were generated as shown in Fig.7.5. The progression of the hot stamping process from 0 to 0.4 represents the holding stage, where a contact pressure of 0.7 MPa has the highest probability. Only the blank holding region of the blank is contacting to the tool, showing a small contact area. In the following stamping process from 0.4 to 0.75, a contact pressure of 4 MPa has the largest probability with a dramatic increases in contact area. The blank is then continually deformed and quenched, where the contact area of the blank reaches 100% and the contact pressure with the largest probability is 15

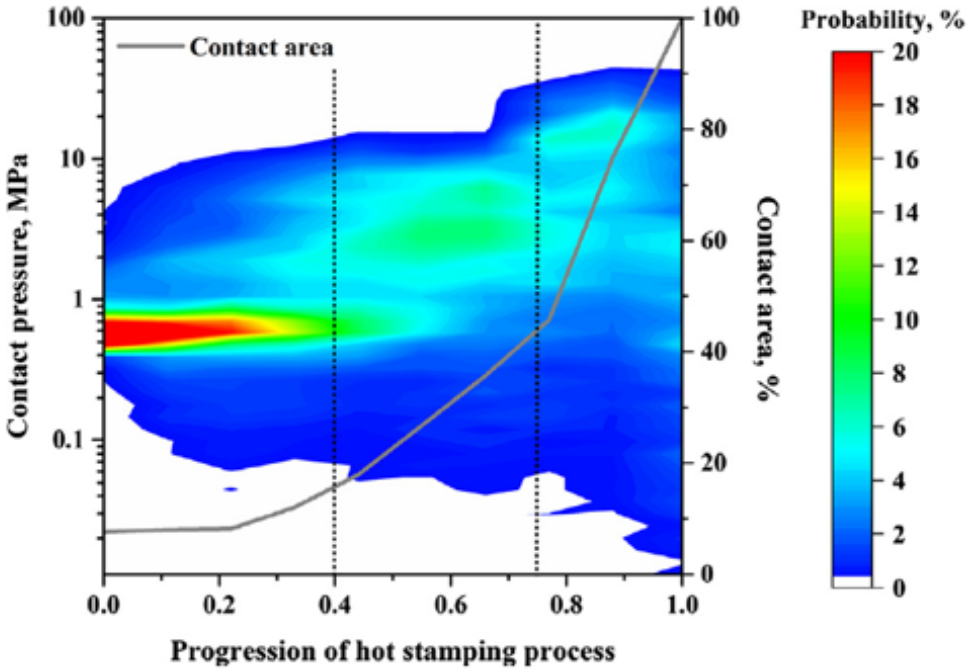


Figure 7.5: Contact pressure and contact area distributions in the progression of the hot stamping process

MPa. The contact pressure trend determined could therefore represent the 3-stage evolutionary variable contact pressure during hot stamping processes.

As shown in Fig. 7.6, when the contact pressure increased from 0.7 to 4 MPa at 0.43 s, the pressure-dependent parameter increased from 0.183 to 0.684, leading to the increasing overall IHTC value from 1.4 to 4.6 kW/m^2K, as shown in Fig. 7.6 (b). Consequently, the temperature decreasing rate was enhanced suddenly at 0.43 s. When the contact pressure increased from 4 to 15 MPa at 1 s, the pressure-dependent parameter and thus the overall IHTC value increased further from 0.684 to 0.987, and from 4.6 to 6.5 kW/m2 K respectively. The decreasing rate of the workpiece temperature was therefore increased suddenly again at 1 s.

In order to represent the complex nature of a hot stamping process, IHTC tests were also conducted with a 3-stage evolutionary variable contact pressure, identified using a data-driven approach. The abrupt changes in the IHTC and consequently the temperature evolutions of the workpiece were successfully captured and agreed well with the results predicted by the developed IHTC model. This indicated that the IHTC model was able to accurately predict the IHTC evolutions as a function of variable contact pressures. It was also verified that the IHTC

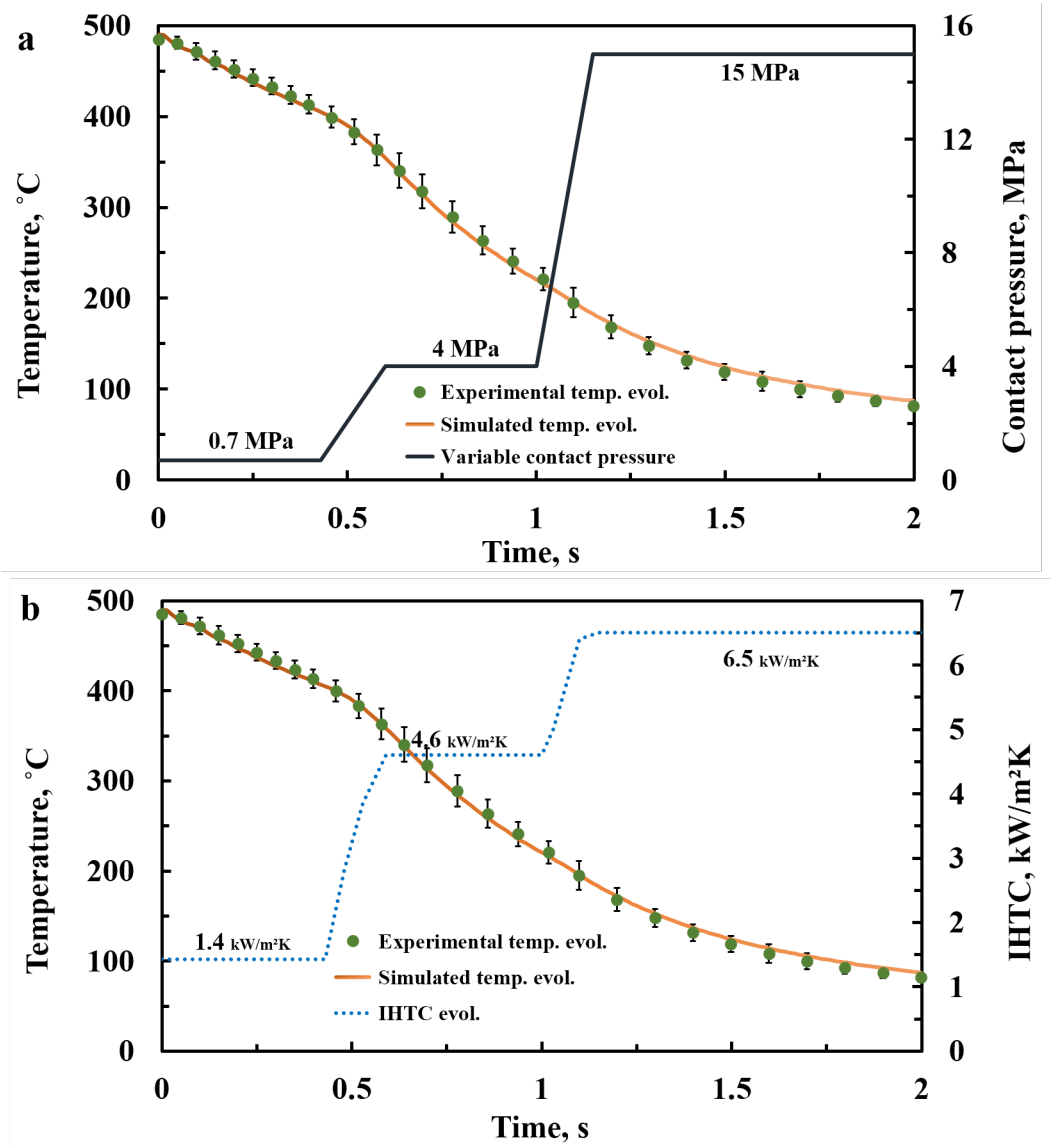


Figure 7.6: (a) Variable contact pressure evolution (b) IHTC evolution, and the comparison between the experimental and simulated temperature evolutions with data-driven IHTC test

test facility was capable of conducting IHTC tests with variable contact pressure conditions and measuring the consequent temperature evolution of the workpiece with abrupt pressure changes. The model and simulation work were conducted by Liu 2019.

Chapter 8

Conclusion

8.1 Thesis review

This thesis focuses on the emergence of a unique research field in sheet metal processing, and introduced a data processing framework and its applications in the research and industry. By studying several FE simulation novel FAST forming technique of lightweight material, data clearing, data standardisation, data normalisation, data classification have been used to develop several algorithms to extract the insightful information from a sheet metal forming process. Data visualisation was proposed to characterise the range of the boundary conditions, which enables corresponding systematic data-driven testing schemes, i.e tribo-map and IHTC map. Experiments verified the effectiveness of the testing scheme. The work presented in this study will enable this traditional industry to be networked in a cooperative environment making the most of industrial resources and increasing manufacturing and modelling efficiency.

8.2 Summary of thesis achievements

In this thesis, a theoretical framework was developed for data processing of vast volumes of information-absent finite element data from high-temperature sheet metal forming processes.

The framework consists of data pre-processing, data filtering and data visualization algorithms. The following conclusions can be drawn:

- Three main typical thermo-mechanical features were found in a high-temperature sheet metal forming process, representing three typical geometrical features of the components, namely a blank holding area, a side wall and a flat bottom. Three thermo-mechanical evolutionary algorithms were developed to enable geometrical characterization of these geometrical features in the absence of spatial or visual data.

- It was found that a strain univariate algorithm was rigorous in recognizing the blank holding area with an accuracy of 95.4%. By utilizing the evolutions of strain, strain rate and temperature, a time-dependent multivariate algorithm was able to successfully identify the side wall and die bottom areas with an accuracy of 92.3% and 85.1%, respectively. Moreover, the performance of the multivariate algorithm was increased by introducing the stress states, such as the Lode parameter and stress triaxiality.

- The utilization of classification algorithms enables the visualization of high-temperature metal forming processes, allowing data-driven research to be conducted.

Simplified laboratory tribological tests are widely used to evaluate the coefficient of friction and interfacial heat transfer coefficient. However, the selection of testing conditions are mainly based on researchers' experience and constant contact conditions are used in most of the previous research, which can not represent the real forming condition during the manufacturing. In this paper, a data-driven method is proposed to generalise the contact conditions during the hot aluminium stamping process, in which the data was successfully analysed to provide a new insight into tribological behaviour during the forming process.

- Through the study of large numbers of experimentally verified finite element simulations, contact conditions at the tool-workpiece interfaces were quantified and illustrated statistically, as tribo-maps, including the contact pressure, temperature difference, wear velocity and wear distance.

- Three different tribological behaviour models are identified which mainly exist in the hot aluminium stamping process, including free-draw, restricted-draw and dynamic models, where different experiment designs and schemes are required.
- All three tribological models happens on die surface, while the punch is mainly restricted-draw model and blank holding is mainly free-draw model.
- By using the data-driven method, the simplified laboratory tribological and IHTC tests can provide realistic contact conditions as tests conducted on real forming tools and relatively lower cost.

8.3 Future work

Future work includes optimising the data processing solutions for sheet metal forming process. The data processing framework for other metal forming processes using 3D mesh, such as bulk metal forming, need further development. Only load jump condition is investigated in this project, a more dedicated friction test setup for data-driven test is required. Robotic arm, which can change speed, load, with a temperature control system is a promising solution.

Appendix A

Appendix: The galling behaviour of advanced coating contacts with aluminium alloy during sliding wear

A.1 Introduction

[1]The forming of aluminium sheets is an efficient manufacturing method for mass-producing automotive components. However there are limitations to the success of aluminium forming processes due to the materials' vulnerability to undergo galling with the forming tools. The consequences of material transfer and adhesive wear to the tool may result in severe damage to the tooling and workpiece surfaces (Hanson, 2008; Figueiredo et al., 2011). Previous studies on the surface modification of steel tooling showed that appropriate methods of polishing were effective in reducing galling (Podgornik et al., 2006; Schedin, 1994). Surface roughness was found to have a large influence on the resistance to galling of tool surfaces, and the application of hard coating provided good anti-galling properties (Podgornik and Jerina, 2012). The majority of previous studies focused on the tribological evaluation of coated tools at room temperature,

[1] This chapter is based on paper work by Hu, Y., Zheng, Y., Politis, D.J., Wang, L. and Gharbi, M.M., Investigation of galling behaviors between an aluminum alloy and metal forming tool. *International Conference on Advanced High Strength Steel and Press Hardening*, Xian, China, 2016.

and therefore it is of particular interest to study the anti-adhesive wear properties of different coating and substrate combinations at elevated temperatures. The aim of this paper is to explore the galling and friction behaviour for a combination of coatings and substrates. Experiments were conducted at room temperature and elevated temperatures, in order to identify the optimum coating and substrate combination that exhibits the lowest level of galling and friction coefficient. Due to the industrially sensitive nature of the substrate tooling materials used in the study, substrate names have been replaced with the notation 'Substrates 1, 2 and 3'

A.2 Material and experiment method

Coated tooling materials were tested through Pin-on-Disc tests using aluminium pins made from AA6082 and AA7075, with a spherical head of 2.5 mm radius and disc diameter 55mm, with materials provided by Schuler Pressen GmbH, as shown in Fig. 7.1 in Section 7.1.2. The mean contact pressure applied in the tests was 0.33 GPa, calculated from the Hertzian contact pressure model. Tooling substrate materials 1 and 2 were pin-on-disc tested with the application of three coatings: AlCrN, CrN and DLC, while substrate 3 was polished, induction heated and plasma nitrided.The coating material, substrate material, pin material and temperature were treated as the independent variables of the test, with coefficient of friction and galling effect as the dependent variables.

An Anton Paar THT tribometer was used to conduct the pin-on-disc friction tests at different testing conditions as shown in Table 1. In the table, the pin material and the temperature of the test for each substrate and coating are shown. The evolution in coefficient of friction was recorded and compared between different coatings. Morphology changes to the disc specimen and the height of the transfer layers were studied through a Veeco White Light Interferometry. The galling behaviour was observed and 3D images showing the severity of material build-up near the wear track were generated.

A.3 Results and discussion

A.3.1 Effects of coating on the evolution of friction coefficient

Fig. A.1 shows the evolution of friction coefficient between Aluminium pins and different coatings at room temperature. The value of friction coefficient between the pin and the uncoated substrates was found to be approximately 0.6. The application of AlCrN and CrN were both ineffective in friction reduction. However, the application of DLC has significantly reduced the COF between the mating materials to approximately 0.2. For substrate 1, as shown in Fig. A.1 (a) and (b), the initial value of COF between the pin and DLC had a value of 0.25, and decreased slightly as sliding distance increased. For substrate 2, as shown in Fig. A.1 (c) and (d), the DLC coating had a similar initial value of COF as the other coatings, but decreased rapidly to a steady state value of just under 0.2. This may be due to a difference in initial surface roughness. During sliding, the deformation of asperities resulted in a polishing effect on the coated surface, suggesting that a polished tool surface may be beneficial for friction reduction when a DLC coating is applied. It was also observed that the use of two different pin materials resulted in no distinct differences on the evolution of friction coefficient, indicating that the selected coatings are effective for both high strength aluminium alloys used in this study.

Fig. A.2 shows the evolution of friction coefficient between the AA6082 pins and different coatings at 300°C. For the uncoated substrates, COF started at a value of 0.6 and continued to increase rapidly as sliding distance increased, due to the galling effect. In contrast, the coated substrates were relatively more effective in controlling friction. However, at this temperature, the DLC coating had lost the advantageous characteristics it displayed at room temperature. For substrate 1, as shown in Fig. A.2 (a), the COF between the substrate and coating remained relatively stable at 0.6. For substrate 2, as shown in Fig. 3A.1 (b), the AlCrN coating showed a COF that decreased from 0.6 to 0.4, whilst the CrN coating showed a COF that remained more stable, decreasing from 0.5 to 0.4. It can be deduced that when the test was conducted at a higher temperature of 300°C, the uncoated materials suffered large amounts of galling,

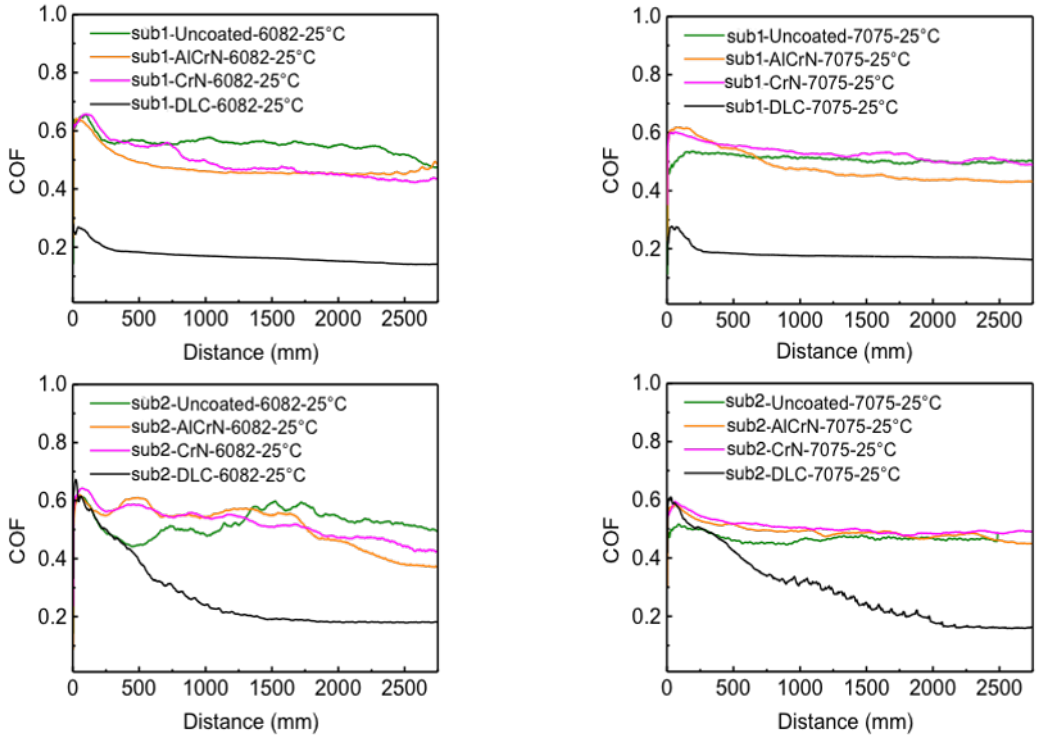


Figure A.1: The evolution of friction coefficient at room temperature of a) substrate 1 sliding with AA6082 pin, b) substrate 1 sliding with AA7075 pin, c) substrate 2 sliding with AA6082 pin and d) substrate 2 sliding with AA7075 pin under various coatings

indicated by a severe build-up of wear particles and Aluminium transfer layer, leading to an increase in surface roughness and Al-Al contacts. The application of coatings could prevent the rapid increase in surface roughness and galling, therefore effectively controlling friction. Fig. A.3 shows the evolution of friction coefficient between the AA6082 pins and different coated substrates, including the induction heated, polished and plasma-nitride treated substrate 3. Substrate 3 exhibits the lowest COF between the mating materials at both room temperature and 300°C. At room temperature, shown in Fig. A.3 (a), the three materials exhibited similar values of friction coefficient, and remained relatively stable throughout the test. The difference in average coefficient of friction between the three materials was less than 10%. At 300°C, as shown in Fig. A.3 (b), the superior characteristics of substrate 3 became more apparent, resulting in an average friction coefficient of approximately 25% lower than substrate 1 and 2. It was also found that the rate of decrease in friction coefficient was larger at elevated temperatures than room temperature. This can be reflected with substrate 1, where at room temperature, its COF decreased from 0.6 to 0.5 whereas at 300°C, COF decreased from 0.6 to 0.4. This suggests that the amount of plastic deformation of asperities at elevated temperature

could be higher, leading to a faster rate of polishing effect. As result, the worn surface may have a mirror-like finish.

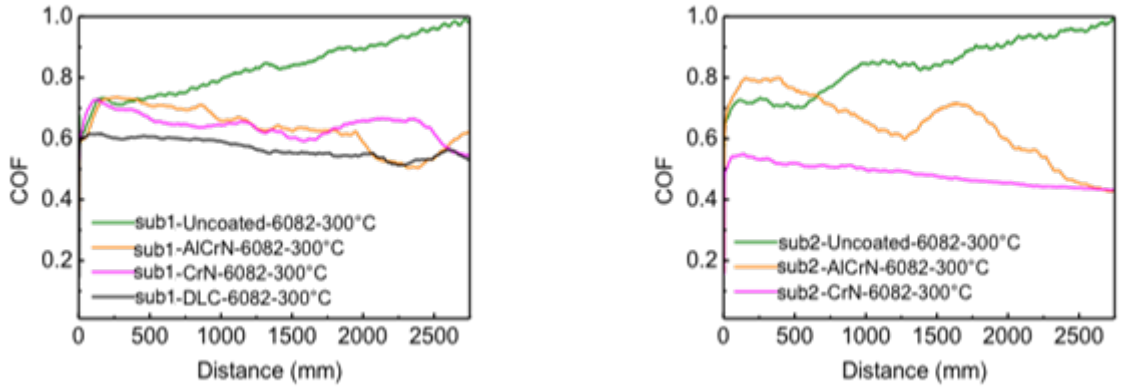


Figure A.2: The evolution of friction coefficient at 300°C of a) substrate 1 and b) substrate 2 under various coatings with AA 6082 pin

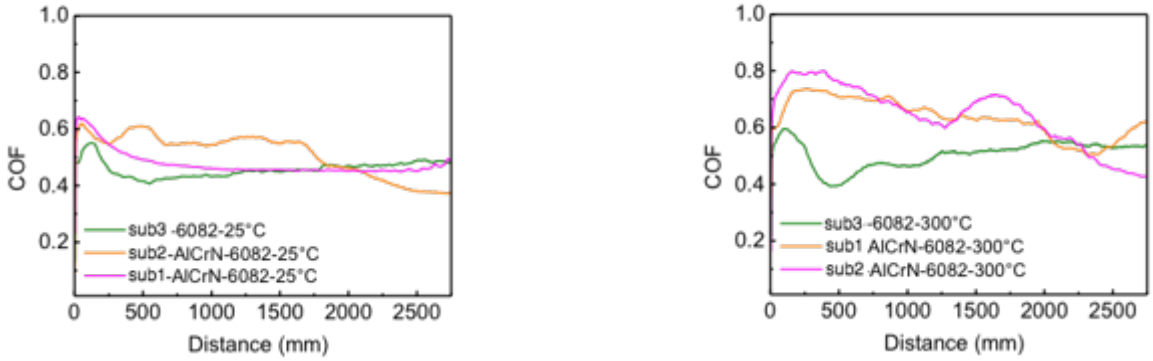


Figure A.3: The evolution of friction coefficient of substrate 3, substrate 2-AlCrN and substrate 1-AlCrN with AA 6082 pins at a) 25°C and b) 300°C

Fig. A.4 shows the evolution of friction coefficient between the AA6082 pins and coatings at room temperature and 300°C. A more apparent advantage of substrate 3 compared to substrate 1 and 2 can be found by comparing these graphs. The performance of substrate 1 and substrate 2 at two temperatures are relatively similar, whilst substrate 3 has demonstrated a good ability to maintain COF at a similar value at room temperature as well as elevated temperatures. For substrate 1, the difference in average coefficient of friction was 26.13% between room temperature and 300°C, as shown in Fig. A.4 (a). For substrate 2, the difference in average coefficient of friction was 32.32%, as shown in Fig. A.4 (b). For substrate 3, a significant difference in performance can be shown in Fig. A.4 (c), in which the difference in average coefficient of friction was 10.43%. In addition, the friction coefficient remained approximately constant at

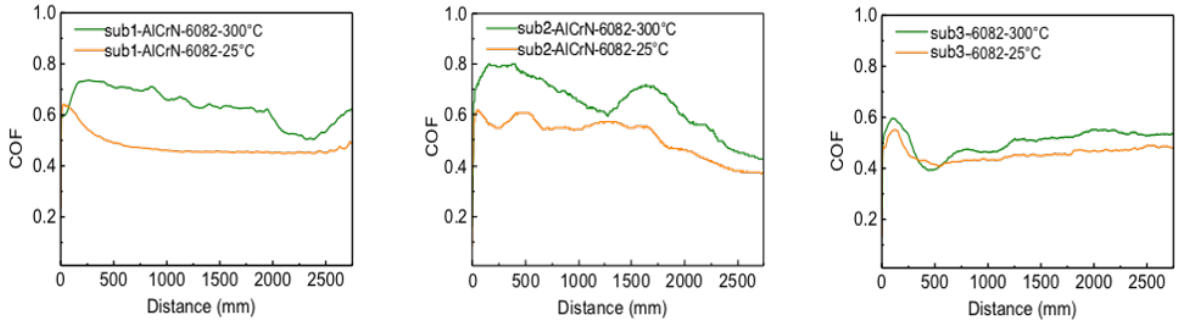


Figure A.4: Evolution of friction coefficient of a) substrate 1-AlCrN, b) substrate 2-AlCrN, c) substrate 3 at 25°C and 300°C with AA 6082 pin

0.5 throughout the duration of contact, suggesting that the asperities on the two surfaces did not undergo significant plastic deformation. The lower average friction coefficient of substrate 3 could also be explained by the induction heating, polishing and plasma-nitride treatment it has undergone, resulting in a very smooth surface since the beginning of the test. A summary of the differences in coefficient of friction at different temperatures is shown in Table 2 below.

A.3.2 Surface topography analysis: galling effect

Fig. A.5 shows the transfer layer thicknesses of substrate 3, substrate 1 - AlCrN, and substrate 1 - CrN. By comparing the surface of substrate 3 with the two other substrates, it has been significantly smooth throughout the tests, up until the test conducted at 450°C, where a significant amount of material build-up occurred. Before the test, substrate 3 started with a lower surface roughness than substrate 1 and substrate 2. At 25°C, the surface of the substrate remained relatively smooth, with a low amount of galling. On the other hand, the other substrate surfaces had already started to show some Aluminium transfer. At 300°C, the surface of substrate 1 - CrN showed severe marks of adhesive wear, and the surface has become extremely rough. The large amount of Aluminium that accumulated in the direction of relative motion suggests that ploughing has occurred. Upon the comparison between substrate 1 with AlCrN and CrN, it was apparent that AlCrN was a better coating, as the amount of galling was significantly lower. At this temperature, the surface of substrate 3 continued to remain relatively smooth. Its beneficial anti-adhesive wear characteristic could also be confirmed by

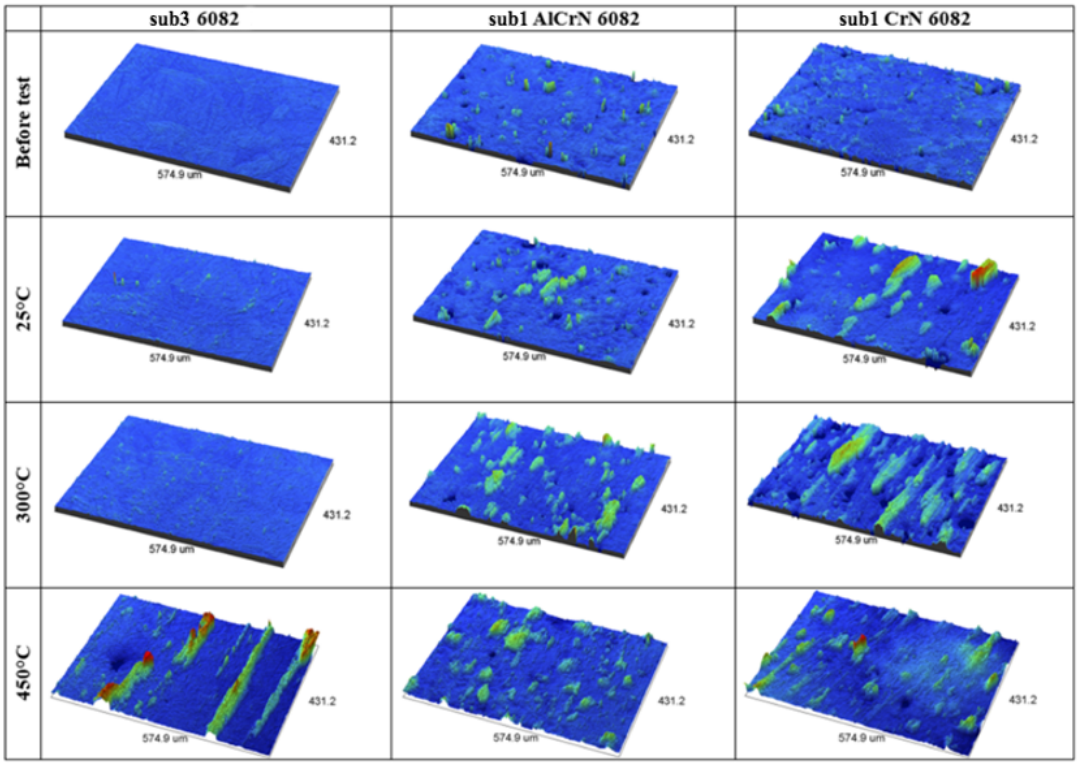


Figure A.5: Surface topography analysis of a) substrate 3, b) substrate 1-AlCrN and c) substrate 1-CrN with AA 6082 pin at 25°C, 300°C, 450°C

the relatively low coefficient of friction at this temperature. However, at 450°C, the surface of substrate 3 also showed a significant amount of material transfer. In comparison with the other substrates, the areas of material build up for substrate 3 were more concentrated in one direction and had higher peak values. For substrate 1, the build-up of material was more evenly spread across the metal surface. Although the surface of substrate 3 showed the least amount of galling at room and intermediate temperatures, at 450°C, the height of material build-up was the most severe. The superior properties of substrate 3 against galling at cold and warm stamping temperatures is also consistent with its ability to maintain a relatively low friction coefficient at these temperatures. This is mainly due to the plasma nitride, induction heating and polishing treatment carried out on it. However, its abilities are found to be limited, which was reflected in the test at 450°C, where severe galling has occurred.

A.4 Conclusion

It was clear that the severity of galling is closely linked to friction coefficient, and they both increase when temperature increases. At room temperature, no obvious distinction was found between the various substrates, either coated or non-coated, except for DLC coating. The application of this coating resulted in significantly lower coefficient of friction at room temperature, however the coating was unable to withstand high temperatures. At elevated temperatures, the application of AlCrN and CrN both resulted in better anti-adhesive wear properties, with no distinct difference between the two coatings, selection of pin material or substrate material. It can be concluded that the substrate 3 that had undergone induction heating, plasma-nitride and polishing exhibited superior anti-adhesive wear properties than all the other substrate - coating combinations. Surface topography displayed the material's high resistance to galling up to 300°C, and tribology tests displayed its low and stable evolution of coefficient of friction. All the other substrate - coating combinations can be concluded to have similar anti-adhesive wear properties that are inferior to substrate 3.

Appendix B

Appendix: FE simulation of aluminium galling inducted forming tool failures under multi-cycle loading conditions

B.1 Introduction

[1]Hard coatings have been used in the metal forming industry in order to obtain lower interfacial friction coefficient and extended tool life (Bunshah and Weissmantel, 2000). Finite element (FE) simulation has been widely used for metal forming processes to accurately predicting material behaviour as well as optimising a forming process. The reliability of FE simulation results is dependent on the accuracy of the material model, for example the flow stress data or constitutive equations; as well as the assignment of boundary conditions, such as friction coefficient and heat transfer coefficient. In the past years, advanced FE simulations have been developed via the implementation of user-defined subroutines, which have significantly broadened the capability of FE simulation software.

Current FE simulations of metal forming processes are mostly performed under single-cycle

[1] This chapter is based on paper work by Zheng, Y., Hu, Y., Gharbi, M.M., Politis, D.J. and Wang, L., Development of coating design guidelines for a sheet metal forming tool-a feasibility study. *Tool Conference*, Bratislava, Slovakia, 2016.

loading conditions, and constant friction coefficient values are assigned to represent the complex tribological nature at the contact interfaces of work-piece material and tools. However, in a real production, the friction coefficient as well as tribological behaviour at the forming tool contact interfaces will vary with the number of forming cycles due to wear(Hu et al., 2015). It is of vital importance for engineers to understand the wear behaviour and the impacts on coating and tool life under multi-cycle loading conditions. However, due to the complexity of multi-cycle loading conditions, it is computationally very expensive to predict tool life using conventional FE simulation software.

This paper introduces an alternative solution to the tool life prediction, namely a multi-objective FEA technique. This technique is based on the application of functional modulus in a cloud computing environment and can provide an efficient and effective method to model the advanced forming features in conjunction with the conventional FE simulation (Wang et al., 2016). In this technique, the data obtained from the FE software is processed within each separated functional module, and is then imported back into the FE software in the relevant consistent format for visualisation and post processing. The structure of the multi-objective FE simulation is shown in Fig. 1.1. The tool life prediction module is one of the 'objectives' in this cloud computing platform. This module is based on an advanced interactive friction model (Ma et al., 2015) to predict the evolution of friction and wear of coatings in a coating tribo-system.

Such an efficient approach enables the prediction of coating wear of forming tools in metal forming industries, and provides guidance for engineers and designers to define the coating life of forming tools. Once the wear of coating is predictable, the thickness of coating to forming tools could be designed based on the actual conditions used in industries. To produce a certain number of products, the required coating thickness can be obtained via the 'tool life prediction' module, ensuring the effectiveness of applied coating during the fabrication and reducing the waste of coating itself. Coating design guidelines for a sheet metal forming tool have been proposed in this paper. A U-shape bending process will be used as a case study to illustrate this technique. The coating design for different forming conditions has been carried out.

B.2 Interactive friction model

In the interactive friction model presented by Ma et al. Ma et al. (2015), the coefficient of friction and wear are two interactive responses of a coating tribo-system, and two origins contribute to the coefficient of friction, the initial friction coefficient $\mu\alpha$ and ploughing friction coefficient μPc, respectively (Eq.B.1). Through a series of ball-on-disk friction tests, the typical evolution of friction coefficient is shown in Fig. B.1 (Hu et al., 2015). It is indicated that the evolution of friction can be divided into three stages by values of friction coefficient as well as the types of wear mechanics. Initially, the friction is mostly generated between the ball and the coating surface. At this stage, the coefficient of friction is relatively low, equal to initial friction coefficient, $\mu\alpha$. Only loose-power like wear particles are produced, having negligible effects on the ploughing friction, μPc. Following this stable stage is the wear stage, where more large-size wear particles accumulated and debris is generated gradually due to localised coating spallation. In this stage, the size of debris is sufficient to be entrapped between the surface asperities and begin ploughing through the coating. In the final stage, the coating is worn out and the coefficient of friction keeps steady at a plateau, μPs (Podgornik et al., 2002, 2011).

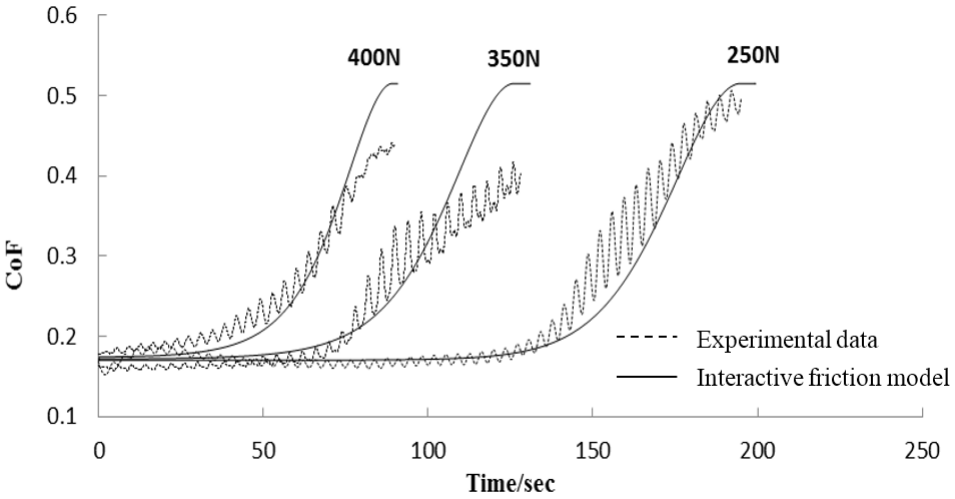


Figure B.1: Evolution of friction coefficient by experimental data and friction model under different loads

$$\mu = \mu_{\alpha} + \mu_{pc} \tag{B.1}$$

$$\mu_{pc} = \mu_{ps} exp\left[-(\lambda_1 h)^{\lambda_2}\right] \tag{B.2}$$

$$h = h_0 - \dot{h}dt \tag{B.3}$$

$$\dot{h} = \frac{KPv}{H_c} \tag{B.4}$$

$$H_c = H_s(\frac{\alpha^2 + h\beta^2}{\alpha + h\beta^2}) \tag{B.5}$$

$$\lambda_1 = k_{\lambda_1} P^{N_{\lambda_1}} \tag{B.6}$$

$$K = k_K P^{N_k} \tag{B.7}$$

In this interactive friction model, the ploughing friction between the ball and substrate is dependent on the instantaneous coating thickness, h (Eq. B.2). The parameters λ_1 and λ_2 are the physical constants of the wear process. Time based integration algorithm is used to capture the remaining coating thickness (Eq. B.3), so that the accumulated wear under varying contact conditions can be modelled, e.g. metal forming operations. The classic Archard law is modified and adopted to predict the wear of the coating (Eq. B.4), which asserts that the instant wear rate $\dot{h}$ is directly proportional to the product of the pressure P and sliding velocity v. The concept of the combined hardness (Eq. B.5) is employed to estimate the evolution of the coating hardness considering the thinning effect of the coating. The friction model parameters include load independent parameters, μ_{ps} , hardness ratio between coating and substrate, α, and the coefficient of thickness, β; k_{λ_1} , k_K, N_{λ_1} and N_k which relate to the evolution of friction and wear are determined empirically, as shown in Table B.1 (Podra and Andersson, 1999; Korsunsky et al., 1998; Komvopoulos, 1991; Holmberg, 1992). Further details of this model can be found in reference (Ma et al., 2015).

Table B.1: Material constants and model parameters of the friction model

λ_2	μ_{ps}	μ_α	α	k_{λ_1}	k_K	N_{λ_1}	N_k
2	0.311	0.17	6	4.58e17	7.27e-23	-3.84	4.095

B.3 Coating design: a feasible study

The interactive friction model is then utilised in a room temperature U-shape bending process via the Multi-objective FEA platform, as a feasibility study to predict the wear of coating. The U-shape bending process is shown in Fig.B.2. This cold forming process is simulated as a symmetric model with a stroke of 75mm, forming speed of 250mm/s, blank holding force of 30kN and initial friction coefficient of 0.17. The forming tools include a die, punch and blank holder. The coating thickness after different forming cycles are estimated and visualized through the multi-objective FEA platform. The detailed procedures can be found in (Wang et al., 2016).

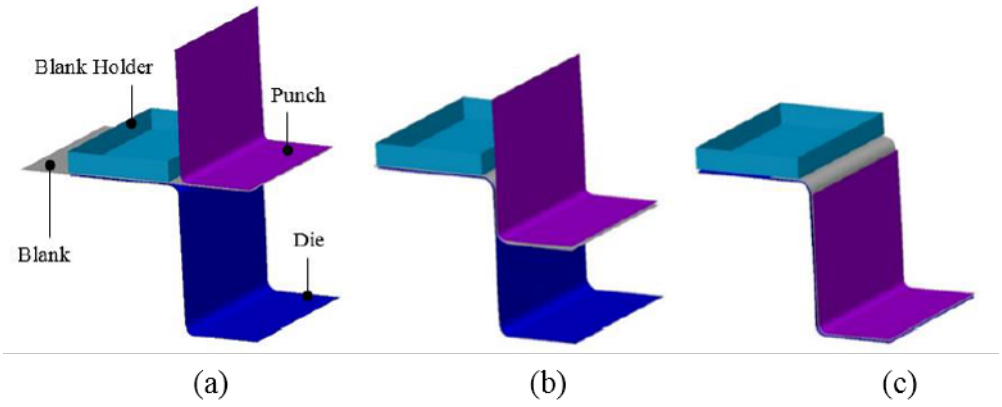


Figure B.2: Pam-stamp simulation of U-shape bending process, presenting the (a) first, (b) forming and (c) final stages of the process; the model consists of a blank, blank holder, punch and die

B.4 Results and discussion

Through this multi-objective FEA platform, the wear of coating of U-shape bending process under multi-cycle condition is carried out. The material constants and model parameters used are listed in Table B.1. The initial coating thickness is 2.10 μm, and the simulation stops when the target loading cycle is reached or the coating is worn out, i.e. the minimum coating thickness on the tool reaches zero. According to the results, it is found that the breakdown cycle for the die of this U-shape bending model is approximately 40600 cycles. Fig. B.3 (a), (b), (c)

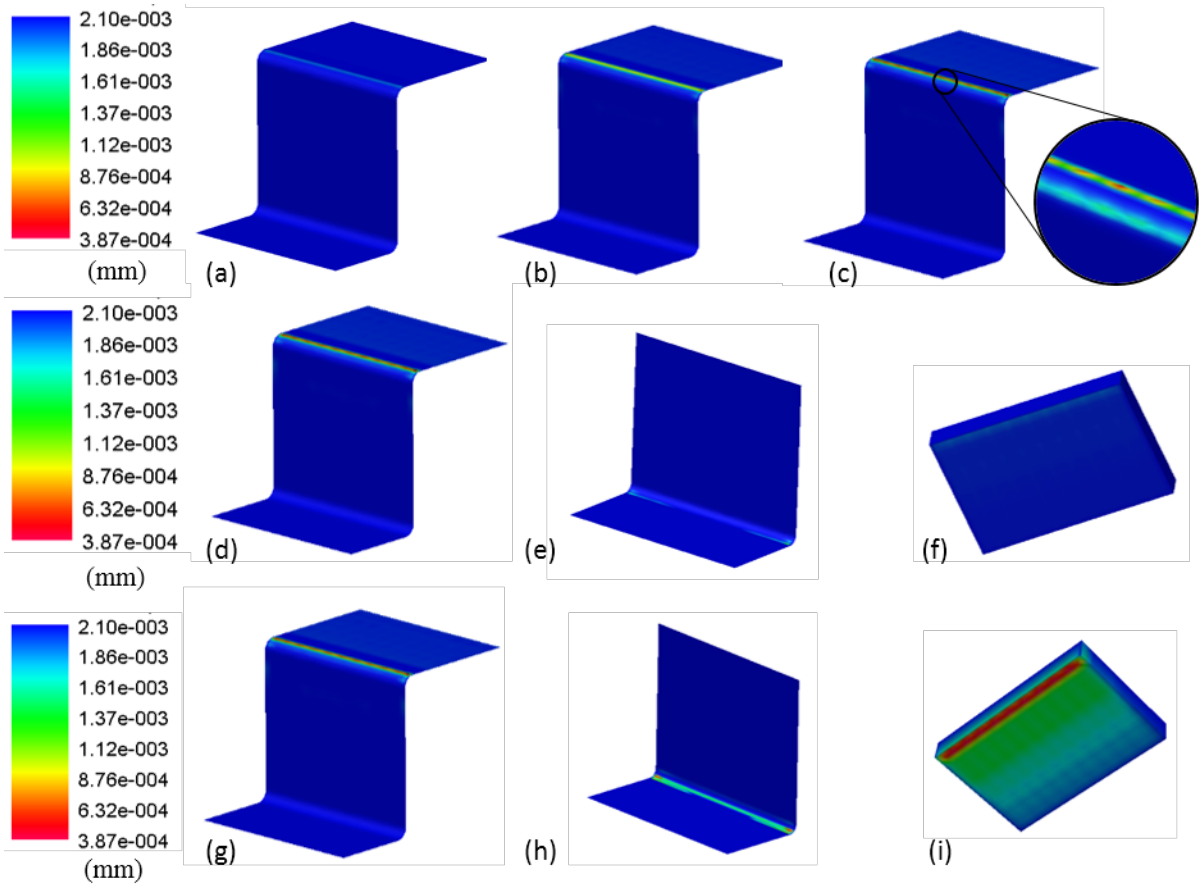


Figure B.3: Remaining coating thickness distributions on the die after (a)500 cycles (b) 20000 cycles (c) 40000 cycles of forming operations detailed wear features, and remaining coating thickness distributions on the (d) die (e) punch (f) top blank holder, after 40000 cycles of forming operations, and coating distribution of (g) die (h) punch and (i) top blank holder when coating breaks down

illustrates the distribution of remaining coating thickness on the die after 500, 20000 and 40000 forming cycles, respectively. It can been seen that the wear of coating mostly concentrates on the entrance region of the die, which undergoes severe sliding wear as a result of high contact pressure and long accumulated sliding distance between the blank and die. The minimum coating thickness on the die remains at about 2.10 μm after 500 cycles, and decreases to 1.08 μm and 0.032 μm after 25000 and 40000 forming cycles, respectively. The detailed features at the draw-die is also illustrated, which is a typical draw-die wear feature [12]. The wear rate gradually increased with time on account of the reduction in combined hardness. The coating thickness decreases continuously afterwards and then eventually breaks down at 40600 cycles. Therefore in this case, it is recommended that for a die with requested forming cycle of 40000, coating with thickness of at least 2.10 μm be used. Furthermore, the wear situations for all

three forming tools for the U-shape bending process were then estimated and compared. Fig. B.3 (d), (e), (f) shows the remaining coating thickness of the die, punch and blank holder after 40000 forming cycles. Their initial coating thicknesses were all set as 2.10 μm. 98% of the coating on the die is worn in this condition, whilst the wear behaviour on the punch and blank holder are negligible. The remaining coating thickness for the punch was still over 2.0 μm, and almost kept at 2.1 μm on blank holder.

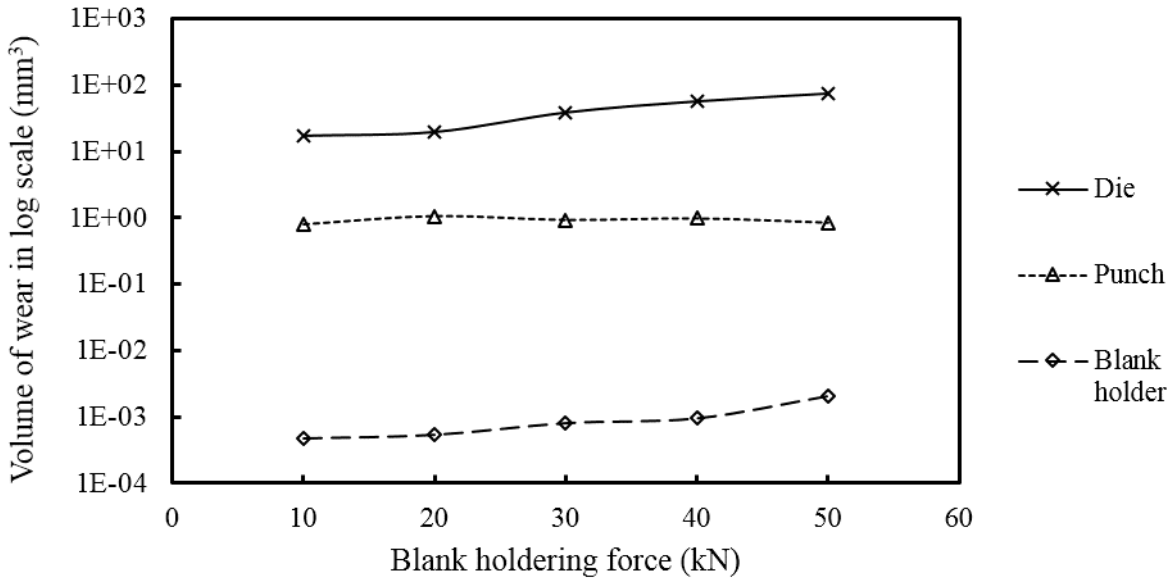


Figure B.4: Wear of volume after 40000 cycles of forming operation

The coating distributions of die, blank holder and punch when the coating breaks down on the tool on itself are shown in Fig. B.3 (g), (h), (i). For the upper blank holder, the coating at the entrance region undergoes relatively severe wear, while the critical wear part of the punch is the corner. The simulations results for different blank holding forces, 10kN, 20kN, 30kN, 40kN and 50kN were then used for further investigation and illustration, and the other forming parameters kept the same. The volume of wear on the forming tools after 40000 cycles of forming operation at different blank holding forces were calculated and plotted in log scale as shown in Fig. B.4. From the figure, it can be clearly seen that the wear on these three forming tools are in different levels. Despite of large accumulated sliding distance, the pressure is considerably lower. As for punch, the contact pressure applied on the punch is similar to that on die, but when comparing to the contact condition between die and blank, the relative sliding distance between the punch and blank is significantly shorter. Fig. B.5 illustrates the

typical distribution of pressure sliding distance on the die, punch and blank holder at a blank holding force of 30kN. The relative sliding speed is calculated from the change of location of forming tools and blank material. From Fig.B.4, the volume of wear on punch and blank holder increases with the rise of blank holding force and the wear on the punch kept almost steady. It is because that with the increase of the blank holding force, the pressure on the critical part of tools increased, the effect of which will override the slight decrease in sliding distance between the tools and blank, eventually leading to relatively severe wear. Fig. B.6 shows a more detailed view of the wear condition at different blank holding force on die and blank holder.

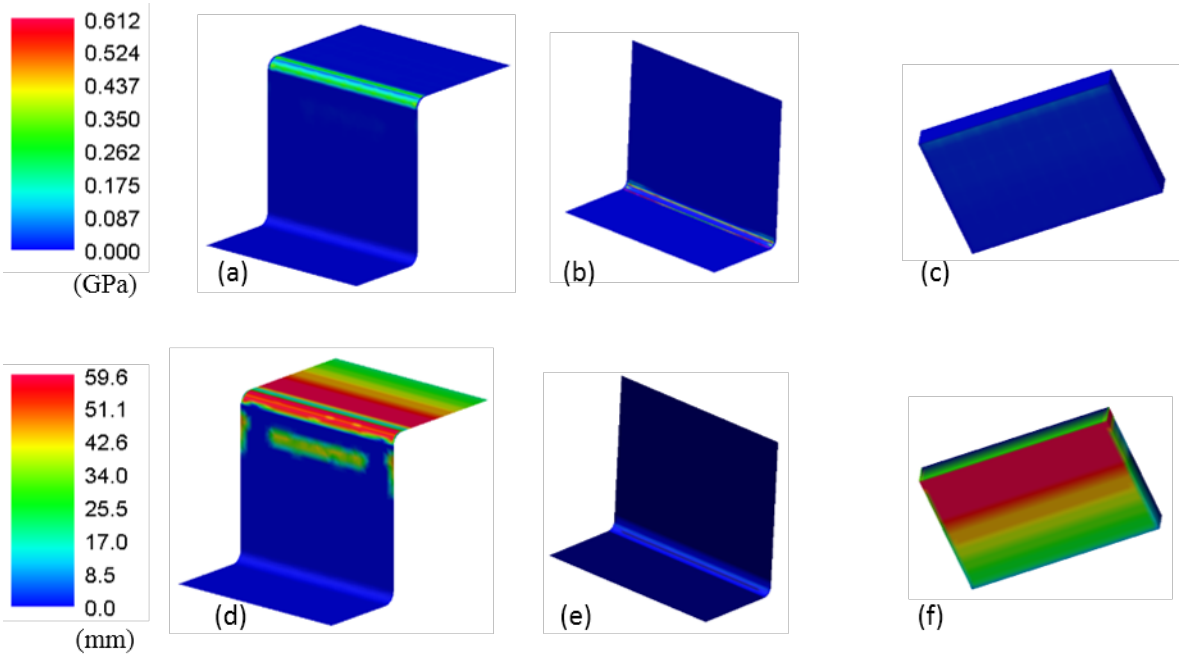


Figure B.5: Typical pressure distribution on the (a) die (b) punch (c) top blank holder for U-shape bending, and relative sliding distance distribution on the (d) die (e) punch (f) top blank holder for U-shape bending at blank holding force of 30 kN

Coating design is a significant issue in the metal forming industry. In addition to the wear volume, the critical wear points on tools are considered in this case study as well. In order to prevent the failure of the coating on forming tools, the required coating thickness to allow 40000 cycles of forming operations is calculated via the multi-objective FEA platform and the results are shown in Fig. B.7, where the minimum coating thickness required in this case is obtained. Furthermore, by using this methodology, the optimized design of coating thicknesses can be obtained for any requested forming cycles or different forming conditions on a set of forming tools, and a more appropriate maintenance routine on the tools can be scheduled consequently.

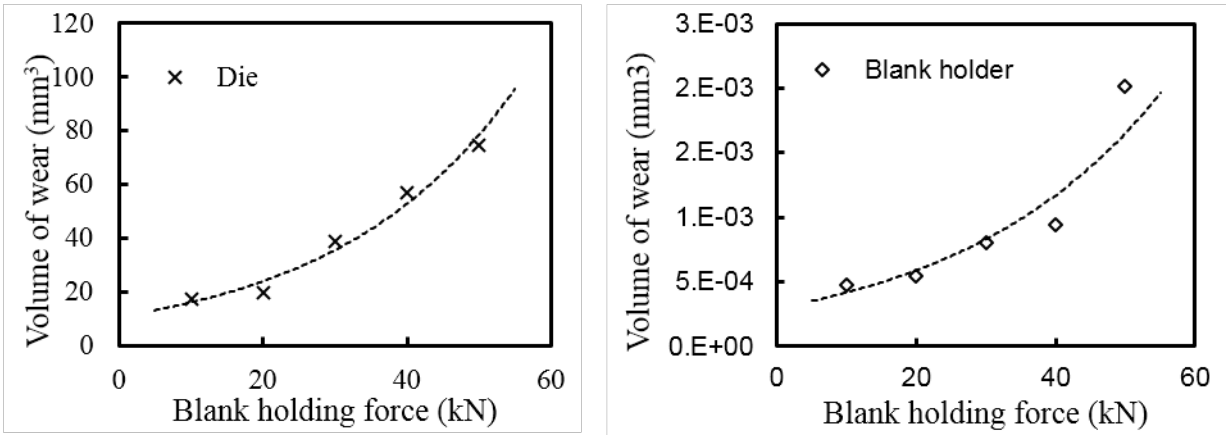


Figure B.6: Volume of wear on Die (right) and Blank holder (left) after 40000 cycles of forming operation

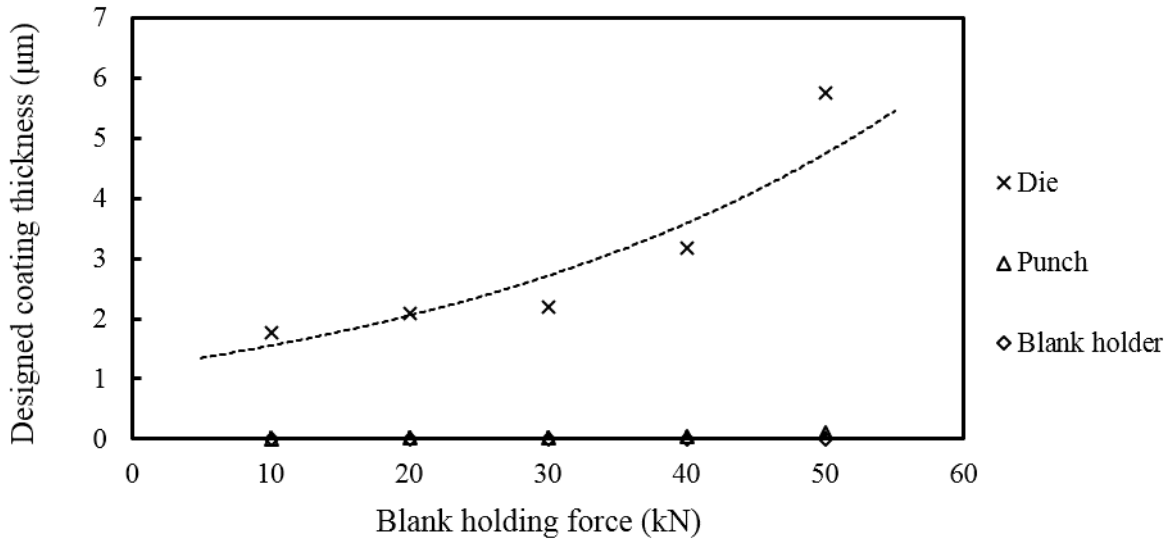


Figure B.7: Designed coating thickness of die, punch and top blank holder for 40000 cycles

This paper provides a novel method to estimate the wear of coating and establish the coating design guideline.

Table B.2: Designed coating thickness applied on forming tool for U-shape bending case study

Tools	Die	Punch	Blank holder
Designed coating thickness	$>2.1\ \mu m$	$>0.1\ \mu m$	$>0.005\ \mu m$

B.5 Conclusion

An advanced friction model was combined with the conventional FE simulation showing the feasibility for predicting wear of coating. In the present research, the combination of the friction model and FE simulation has enabled the coating life prediction for a sheet metal forming processes. The distributions of coating thickness after different forming cycles are estimated and visualised, which could provide the information about the wear condition during the forming process. Based on these, a guideline for coating design of the forming tools has been developed.

Appendix C

Appendix: Data-driven tensile test guidelines for hot stamping of aluminium alloys

C.1 Introduction

Material property characterisation is an essential requirement of FE simulations, as their accuracy is greatly enhanced with a detailed definition of the material's deformation behaviour, input in the form of either discrete data known as 'look-up tables', or a set of constitutive equations describing their flow stresses. Thus, sensible selection of the conditions at which the material properties are characterised, through tensile or formability testing for example, is needed. Currently, tensile testing conditions are usually selected based on experience as opposed to the real requirements of the actual application of the material. Strain rates in the range of 10^{-5} - 10^{-2} s^{-1} are used to study superplastic forming (Horita et al., 2000; Watanabe et al., 1999), strain rates of 10^{-1} - 1 s^{-1} are used for steel sheet metal forming(Turetta et al., 2006), and strain rates of 10^{-4} - 10^{-2} s^{-1} are utilised in the study of low-cycle fatigue (Hong and Lee, 2004). Large variations in temperature ranges also exist across different applications, such as in warm and hot stamping of aluminium alloys, where a range of 150 - 525 °C is used

(Mohamed et al., 2012; El Fakir et al., 2014). To enhance the utility of the material data input, the selected test matrix must be targeted according to the specific application of the material and its associated conditions of strain rate and temperature. In the present research, an innovative data driven approach was developed by data mining existing experimentally verified FE simulation results obtained from the *SmartForming*®. By tracking the deformation history of each element, the real thermo-mechanical conditions in a hot stamping process were identified.

C.2 Methodology: data-driven approach for tensile test

As a FE simulation orientated multi-objective platform, experimentally verified simulations from *SmartForming* ® can be used to construct a database from historical FE simulations to provide a comprehensive quantification of temperature and strain rate conditions. In this section, the 'Strategy' module is implemented to study the deformation characteristics of AA6082 under hot stamping conditions.

The 'Strategy' module works in three stages: data acquisition, data processing and data analysis, as shown in Fig.C.1. Data is acquired through the multi-objective *SmartForming*® platform, which can be accessed via www.smartforming.com. This is an online portal system developed at Imperial College enabling engineers to share their knowledge and sophisticated models. The case study in this paper is based on a database for hot stamping simulations of lab scale dome tests. Simulations were conducted at different forming conditions, such as different forming speeds and blank holding forces. The database consists of the thermo-mechanical history of all elements in all stages of each simulation to capture the characteristics of the

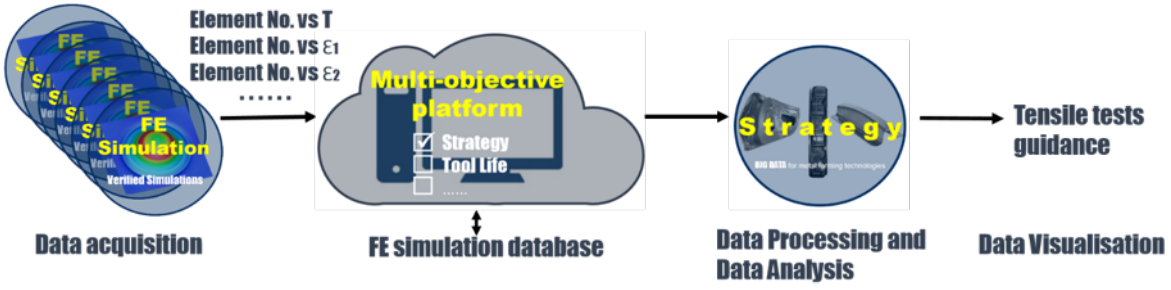


Figure C.1: Smartforming simulation database - 'strategy' implementation process

deformation process. Data from each simulation is stored as a separate entity and managed in the central cloud data system, and is then processed and analysed in the functional module. To establish a uniaxial tensile test guide for the hot stamping technique, evolutions of temperature and strain rate are selected from each simulation file. The first step involves filtering the raw data to distinguish between elements from different regions, e.g. the blank holding area, die cavity etc. In this study, the elements in the blankholder region are removed since plastic deformation in this region is very low, and does not represent the characteristics of hot stamping. Due to the possibility of each simulation file having different numbers of elements, the data could potentially be distorted, thus a weighting strategy is applied to adjust the proportional relevance of each simulation to generate representative data. Single and bivariate parameter distributions are then generated for data analysis.

C.3 Results and discussion: thermo-mechanical characteristics of the hot aluminium stamping technology

Hot stamping of the dome shapes exhibits complicated temperature, strain rate and strain path histories. Fig.C.2 shows the temperature and strain rate distributions for AA6082 dome shaped parts formed under hot stamping conditions. The temperature distribution is found to be negatively skewed as the majority of elements undergoing hot stamping tend to have higher temperatures. 66% of the elements were formed in the 400 - 450 °C temperature range. The peak of the distribution indicates the most frequent occurrence, and corresponds to the initial forming temperature of 450 °C used in the lab scale dome tests. The minimum temperature was found to be around 210 °C, while the maximum was 455°C, which may have been caused by frictional heat. The strain rate distribution resembles a normal distribution, and although the peak region of strain rates of 0.1 - 1 s^{-1} are commonly tested, strain rates higher than 1 s^{-1} are also encountered during hot stamping, occupying 29% of the distribution, where the maximum strain rate was around 30 s^{-1}. Single parameter distributions provide valuable insights into the lower and upper limits, as well as the variation of the conditions encountered in hot stamping

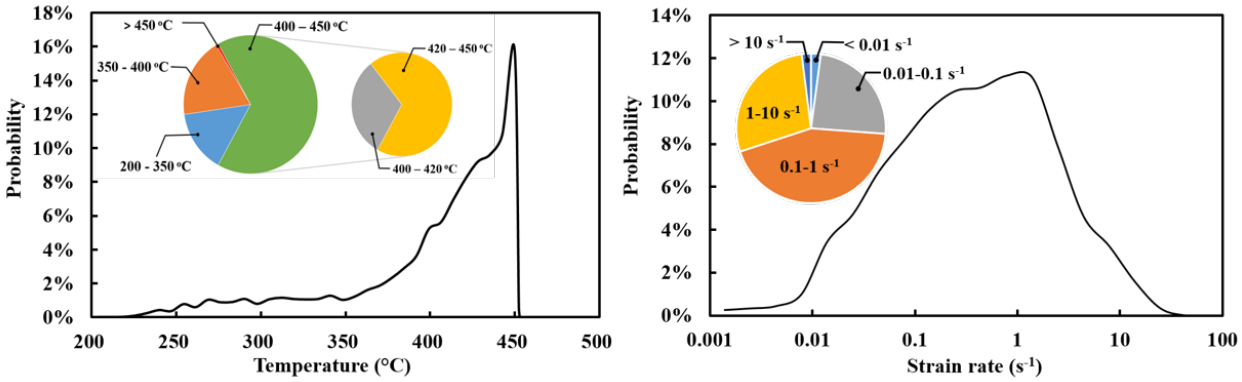


Figure C.2: Temperature and strain rate distribution for AA6082 formed under hot stamping conditions

processes.

To facilitate the design of tensile test guidelines, a bivariate distribution incorporating the relationship between temperature and strain rate was investigated. This offers greater benefits as tensile tests are conducted at conditions based on both parameters. The relationship between temperature and strain rate obtained from the dome shape forming simulations is visualised in Fig.C.3, and provides the tensile test boundaries for the hot stamping of dome shapes from AA6082. The maximum and minimum values are the same as those identified in the single parameter distribution. However, higher strain rates (> 5 s^{-1}) were found to be only associated with high temperatures between 350 - 450 °C; this phenomenon is expected as at higher temperatures, the material is softer and hence more plastic deformation occurs leading to higher strain rates. 71.5% of the elements deformed in the temperature and strain rate range of 400 - 455 °C and 0.01 - 10 s^{-1} respectively. For all temperatures below 350 °C, a maximum strain rate of 5 s^{-1} would be sufficient, which occurred for 13.5% of the elements. It is therefore critical to conduct tensile tests that cover the lower and upper limits, as well as to focus on specific combinations of conditions with the greatest probabilities.

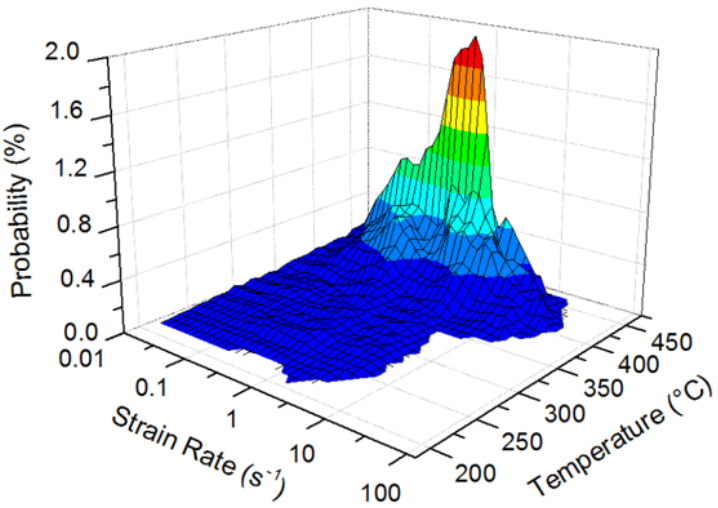


Figure C.3: Temperature and strain rate distribution for AA6082 formed under hot stamping conditions

C.4 Conclusion

The parametric study utilised in the 'Strategy' functional module provides a viable approach for determining test matrices for tensile tests and the conditions to be investigated. The module integrates data from different simulation parts used in the *SmartForming* ® platform, and numerically analyses the temperature and strain rate distributions to reduce uncertainties in the critical input used in simulating the mechanical behaviour. It has captured dominant temperature and strain rate conditions the blank undergoes during a hot stamping process and detected the trends in the hot stamping of AA6082. The boundaries and trends identified will allow researchers to conduct more focused and targeted tensile tests, reducing the efforts of experiments, and improving efficiency and productivity. As the *SmartForming* ® platform database expands, more material and forming technique specific tensile test guides could be generated, with opportunities to develop more strategic analyses to gain insights into various forming techniques.

Bibliography

Ablat, M. A. and Qattawi, A. (2017), 'Numerical simulation of sheet metal forming: a review', *The international journal of advanced manufacturing technology* **89**(1-4), 1235–1250.

Altan, T., Oh, S.-I. and Gegel, G. (1983), 'Metal forming fundamentals and applications', *American Society for Metals, 1983,* p. 353.

Avitzur, B. (1968), *Metal forming: processes and analysis*, Vol. 968, McGraw-Hill New York.

Bai, Q., Lin, J., Zhan, L., Dean, T., Balint, D. and Zhang, Z. (2012), 'An efficient closed-form method for determining interfacial heat transfer coefficient in metal forming', *International Journal of Machine Tools and Manufacture* **56**, 102–110.

Bay, N., Olsson, D. D. and Andreasen, J. L. (2008), 'Lubricant test methods for sheet metal forming', *Tribology International* **41**(9-10), 844–853.

Binder, M., Klocke, F. and Döbbeler, B. (2017), 'An advanced numerical approach on tool wear simulation for tool and process design in metal cutting', *Simulation Modelling Practice and Theory* **70**, 65–82.

Bruschi, S., Altan, T., Banabic, D., Bariani, P., Brosius, A., Cao, J., Ghiotti, A., Khraisheh, M., Merklein, M. and Tekkaya, A. (2014), 'Testing and modelling of material behaviour and formability in sheet metal forming', *CIRP Annals* **63**(2), 727–749.

Bunshah, R. and Weissmantel, C. (2000), 'Handbook of hard coatings'.

Burges, C., Shaked, T., Renshaw, E., Lazier, A., Deeds, M., Hamilton, N. and Hullender, G. N.

(2005), Learning to rank using gradient descent, *in* 'Proceedings of the 22nd International Conference on Machine learning (ICML-05)', pp. 89–96.

Caron, E. J., Daun, K. J. and Wells, M. A. (2014), 'Experimental heat transfer coefficient measurements during hot forming die quenching of boron steel at high temperatures', *International Journal of Heat and Mass Transfer* **71**, 396–404.

Carpenter, B. (2008), 'Lazy sparse stochastic gradient descent for regularized multinomial logistic regression', *Alias-i, Inc., Tech. Rep* pp. 1–20.

Casella, G. and Berger, R. L. (2002), *Statistical Inference*.

Choi, K., Fazekas, G., Sandler, M. and Cho, K. (2017), Convolutional recurrent neural networks for music classification, *in* '2017 IEEE International Conference on Acoustics, Speech and Signal Processing (ICASSP)', IEEE, pp. 2392–2396.

Chongthairungruang, B., Uthaisangsuk, V., Suranuntchai, S. and Jirathearanat, S. (2013), 'Springback prediction in sheet metal forming of high strength steels', *Materials & Design* **50**, 253–266.

Chowdhury, M. A., Khalil, M. K., Nuruzzaman, D. M. and Rahaman, M. L. (2011), 'The effect of sliding speed and normal load on friction and wear property of aluminum', *International Journal of Mechanical and Mechanics Engineering* **11**(1), 53–57.

Dahle, A. K., Lee, Y. C., Nave, M. D., Schaffer, P. L. and StJohn, D. H. (2001), 'Development of the as-cast microstructure in magnesium–aluminium alloys', *Journal of light metals* **1**(1), 61–72.

de Baas, A. (2010), 'Research road mapping in materials', *Directorate-General for Research, Directorate GâĂŤIndustrial Technologies, Unit G* **3**.

Dohda, K., Boher, C., Rezai-Aria, F. and Mahayotsanun, N. (2015), 'Tribology in metal forming at elevated temperatures', *Friction* **3**(1), 1–27.

El Fakir, O., Wang, L., Balint, D., Dear, J. P., Lin, J. and Dean, T. A. (2014), 'Numerical study of the solution heat treatment, forming, and in-die quenching (hfq) process on aa5754', *International Journal of Machine Tools and Manufacture* **87**, 39–48.

Eriksen, M. (1997), 'The influence of die geometry on tool wear in deep drawing', *Wear* **207**(1-2), 10–15.

Figueiredo, L., Ramalho, A., Oliveira, M. C. and Menezes, L. F. (2011), 'Experimental study of friction in sheet metal forming', *Wear* **271**(9-10), 1651–1657.

Froes, F. (1994), 'Advanced metals for aerospace and automotive use', *Materials Science and Engineering: A* **184**(2), 119–133.

Gal, Y. and Ghahramani, Z. (2015), 'A Theoretically Grounded Application of Dropout in Recurrent Neural Networks'.
URL: *http://arxiv.org/abs/1512.05287*

Gali, O. A., Riahi, A. R. and Alpas, A. T. (2013), 'The tribological behaviour of AA5083 alloy plastically deformed at warm forming temperatures', *Wear* **302**(1-2), 1257–1267.

Gao, H., El Fakir, O., Wang, L., Politis, D. J. and Li, Z. (2017), 'Forming limit prediction for hot stamping processes featuring non-isothermal and complex loading conditions', *International Journal of Mechanical Sciences* **131**, 792–810.

Garrett, R., Lin, J. and Dean, T. (2005), 'An investigation of the effects of solution heat treatment on mechanical properties for aa 6xxx alloys: experimentation and modelling', *International Journal of Plasticity* **21**(8), 1640–1657.

Ghiotti, A. and Bruschi, S. (2011), Tribological behaviour of DLC coatings for sheet metal forming tools, Technical Report 9-10.

Ghiotti, A., Bruschi, S., Medea, F. and Hamasaiid, A. (2016), 'Tribological behavior of high thermal conductivity steels for hot stamping tools', *Tribology International* **97**, 412–422.

Ghiotti, A., Sgarabotto, F. and Bruschi, S. (2013), 'A novel approach to wear testing in hot stamping of high strength boron steel sheets', *Wear* **302**(1-2), 1319–1326.

Gourieroux, C., Monfort, A. and Renault, E. (1993), 'Indirect inference', *Journal of applied econometrics* **8**(S1), S85–S118.

Graves, A. (2012), Supervised sequence labelling, *in* 'Supervised sequence labelling with recurrent neural networks', Springer, pp. 5–13.

Hanna, M. D. (2009), 'Tribological evaluation of aluminum and magnesium sheet forming at high temperatures', *Wear* **267**(5-8), 1046–1050.

Hansen, N. (1977), 'The effect of grain size and strain on the tensile flow stress of aluminium at room temperature', *Acta Metallurgica* **25**(8), 863–869.

Hanson, M. (2008), *On Adhesion and Galling in Metal Forming*.

He, Z., Wang, Z. and Teng, B. (2004*a*), 'A graphic representation of traction for a 3d elastic/plastic stress state', *International Journal of Mechanical Engineering Education* **32**(2), 153–159.

He, Z., Wang, Z. and Teng, B. (2004*b*), 'Three-dimensional representation of normal stress magnitude with applications to hydrobulge forming', *The Journal of Strain Analysis for Engineering Design* **39**(2), 205–211.

Heinrichs, J. and Jacobson, S. (2009), 'Laboratory test simulation of galling in cold forming of aluminium', *Wear* **267**(12), 2278–2286.

Heinrichs, J. and Jacobson, S. (2010), 'Laboratory test simulation of aluminium cold forming - influence from PVD tool coatings on the tendency to galling', *Surface and Coatings Technology* **204**(21-22), 3606–3613.

Hochreiter, S. and Schmidhuber, J. (1997), 'Long short-term memory', *Neural computation* **9**(8), 1735–80.
URL: *http://www.ncbi.nlm.nih.gov/pubmed/9377276*

Holmberg, K. (1992), 'A concept for friction mechanisms of coated surfaces', *Surface and Coatings Technology* **56**(1), 1–10.

Hong, S.-G. and Lee, S.-B. (2004), 'The tensile and low-cycle fatigue behavior of cold worked 316l stainless steel: influence of dynamic strain aging', *International Journal of Fatigue* **26**(8), 899–910.

Horita, Z., Furukawa, M., Nemoto, M., Barnes, A. and Langdon, T. (2000), 'Superplastic forming at high strain rates after severe plastic deformation', *Acta Materialia* **48**(14), 3633–3640.

Hu, J., Marciniak, Z. and Duncan, J. (2002), *Mechanics of sheet metal forming*, Elsevier.

Hu, W., He, Z. and Fang, Y. (2004), 'Uniform principle on stress, strain and yield locus for analysing metal forming processes: the contribution of prof. zr wang', *Journal of materials processing technology* **151**(1-3), 27–32.

Hu, Y., Yuan, X., Ma, G., Masen, M. and Wang, L. (2015), 'Tool-life prediction under multi-cycle loading during metal forming: a feasibility study', *Manufacturing Review* **2**, 28.

Hu, Y., Zheng, Y., Politis, D., Masen, M., Cui, J. and Wang, L. (2019), 'Development of an interactive friction model to predict aluminum transfer in a pin-on-disc sliding system', *Tribology International* **130**, 216–228.

Hu, Y., Zheng, Y., Yang, X., Politis, D., Wang, L., Gharbi, M. and Cui, J. (2018), Fe simulation of aluminium galling induced forming tool failures under multi-cycle loading conditions: A feasibility study, *in* 'Advanced High Strength Steel And Press Hardening-Proceedings Of The 4th International Conference On Advanced High Strength Steel And Press Hardening (Ichsu2018)', World Scientific, p. 194.

Ilkhchy, A. F., Jabbari, M. and Davami, P. (2012), 'Effect of pressure on heat transfer coefficient at the metal/mold interface of a356 aluminum alloy', *International Communications in Heat and Mass Transfer* **39**(5), 705–712.

Isik, K., Silva, M., Tekkaya, A. and Martins, P. (2014), 'Formability limits by fracture in sheet metal forming', *Journal of materials processing technology* **214**(8), 1557–1565.

Khoury, M. J. and Ioannidis, J. P. (2014), 'Big data meets public health', *Science* **346**(6213), 1054–1055.

Kingma, D. P. and Ba, J. (2014), 'Adam: A method for stochastic optimization', *arXiv preprint arXiv:1412.6980* .

Kleinbaum, D. G., Dietz, K., Gail, M., Klein, M. and Klein, M. (2002), *Logistic regression*, Springer.

Komvopoulos, K. (1991), 'Sliding friction mechanisms of boundary-lubricated layered surfaces: Part iiâĂŤtheoretical analysis', *Tribology transactions* **34**(2), 281–291.

Kopec, M., Wang, K., Politis, D. J., Wang, Y., Wang, L. and Lin, J. (2018), 'Formability and microstructure evolution mechanisms of ti6al4v alloy during a novel hot stamping process', *Materials Science and Engineering: A* **719**, 72–81.

Kopec, M., Wang, K., Wang, Y., Wang, L. and Lin, J. (2018), Feasibility study of a novel hot stamping process for ti6al4v alloy, *in* 'MATEC Web of Conferences', Vol. 190, EDP Sciences, p. 08001.

Korsunsky, A., McGurk, M., Bull, S. and Page, T. (1998), 'On the hardness of coated systems', *Surface and Coatings Technology* **99**(1-2), 171–183.

Kwon, O., Lee, N. and Shin, B. (2014), 'Data quality management, data usage experience and acquisition intention of big data analytics', *International Journal of Information Management* **34**(3), 387–394.

Lee, J., Lapira, E., Bagheri, B. and Kao, H.-a. (2013), 'Recent advances and trends in predictive manufacturing systems in big data environment', *Manufacturing Letters* **1**(1), 38–41.

Li, D. and Ghosh, A. K. (2004), 'Effects of temperature and blank holding force on biaxial forming behavior of aluminum sheet alloys', *Journal of materials engineering and performance* **13**(3), 348–360.

Li, K., Carden, W. and Wagoner, R. (2002), 'Simulation of springback', *International Journal of Mechanical Sciences* **44**(1), 103–122.

Li, Z., Qu, H., Chen, F., Wang, Y., Tan, Z., Kopec, M., Wang, K. and Zheng, K. (2019), 'Deformation behavior and microstructural evolution during hot stamping of ta15 sheets: Experimentation and modelling', *Materials* **12**(2), 223.

Lin, J. (2015), *Fundamentals of materials modelling for metals processing technologies: theories and applications*, World Scientific Publishing Company.

Liu, J., Gao, H., El Fakir, O., Wang, L. and Lin, J. (2016), 'Hot stamping of AA6082 tailor welded blanks: experiment and FE simulation', *Manufacturing Review* **3**(January), 8.

Liu, X., El Fakir, O., Zheng, Y., Gharbi, M. M. and Wang, L. (2019), 'Effect of tool coatings on the interfacial heat transfer coefficient in hot stamping of aluminium alloys under variable contact pressure conditions', *International Journal of Heat and Mass Transfer* **137**, 74–83.

Liu, X., Ji, K., Fakir, E. O., Fang, H., Gharbi, M. M. and Wang, L. (2017), 'Determination of the Interfacial Heat Transfer Coefficient for a Hot Aluminium Stamping Process', *Journal of Materials Processing Technology* **247**(April), 158–170.

Luo, Y., Luckey, S., Friedman, P. and Peng, Y. (2008), 'Development of an advanced superplastic forming process utilizing a mechanical pre-forming operation', *International Journal of Machine Tools and Manufacture* **48**(12-13), 1509–1518.

Ma, G., Wang, L., Gao, H., Zhang, J. and Reddyhoff, T. (2015), 'The friction coefficient evolution of a tin coated contact during sliding wear', *Applied Surface Science* **345**, 109–115.

Mallick, P. K. (2010), *Materials, design and manufacturing for lightweight vehicles*, Elsevier.

Masters, I., Williams, D. and Roy, R. (2013), 'Friction behaviour in strip draw test of pre-stretched high strength automotive aluminium alloys', *International Journal of Machine Tools and Manufacture* **73**, 17–24.

Milkereit, B., Wanderka, N., Schick, C. and Kessler, O. (2012), 'Continuous cooling precipitation diagrams of al–mg–si alloys', *Materials Science and Engineering: A* **550**, 87–96.

Mitchell, T. M. (1997), *Machine Learning*, McGraw-Hill.

Mohamed, M. S., Foster, A. D., Lin, J., Balint, D. S. and Dean, T. A. (2012), 'Investigation of deformation and failure features in hot stamping of AA6082: Experimentation and modelling', *International Journal of Machine Tools and Manufacture* **53**(1), 27–38.

Myhr, O. R., Grong, Ø. and Schäfer, C. (2015), 'An extended age-hardening model for al-mg-si alloys incorporating the room-temperature storage and cold deformation process stages', *Metallurgical and Materials Transactions A* **46**(12), 6018–6039.

Ng, A. (2018), 'CS229: Machine Learning'.
URL: *http://cs229.stanford.edu/syllabus.html*

Nielsen, C. and Bay, N. (2018), 'Review of friction modeling in metal forming processes', *Journal of Materials Processing Technology* **255**, 234–241.

Papineni, K., Roukos, S., Ward, T. and Zhu, W.-J. (2002), Bleu: a method for automatic evaluation of machine translation, *in* 'Proceedings of the 40th annual meeting on association for computational linguistics', Association for Computational Linguistics, pp. 311–318.

Pereira, M. P., Duncan, J. L., Yan, W. and Rolfe, B. F. (2009), 'Contact pressure evolution at the die radius in sheet metal stamping', *Journal of Materials Processing Technology* **209**(7), 3532–3541.

Pereira, M. P., Yan, W. and Rolfe, B. F. (2010), 'Sliding distance, contact pressure and wear in sheet metal stamping', *Wear* **268**(11-12), 1275–1284.

Pereira, M. P., Yan, W. and Rolfe, B. F. (2012), 'Wear at the die radius in sheet metal stamping', *Wear* **274-275**(April), 355–367.

Peters, M., Kumpfert, J., Ward, C. H. and Leyens, C. (2003), 'Titanium alloys for aerospace applications', *Advanced engineering materials* **5**(6), 419–427.

Podgornik, B., Hogmark, S. and Pezdirnik, J. (2004), 'Comparison between different test methods for evaluation of galling properties of surface engineered tool surfaces', *Wear* **257**(7-8), 843–851.

Podgornik, B., Hogmark, S. and Sandberg, O. (2002), Hard pvd coatings and their perspectives in forming tool applications, *in* '6th International Tooling Conference, Karlstad (Sweden)', pp. 1053–1066.

Podgornik, B., Hogmark, S. and Sandberg, O. (2006), 'Proper coating selection for improved galling performance of forming tool steel', *Wear* **261**(1), 15–21.

Podgornik, B. and Jerina, J. (2012), 'Surface topography effect on galling resistance of coated and uncoated tool steel', *Surface and Coatings Technology* **206**(11-12), 2792–2800.

Podgornik, B., Zajec, B., Bay, N. and Vižintin, J. (2011), 'Application of hard coatings for blanking and piercing tools', *Wear* **270**(11-12), 850–856.

Podra, P. and Andersson, S. (1999), 'Simulating sliding wear with finite element method', *Tribology international* **32**(2), 71–81.

Preis, T., Moat, H. S. and Stanley, H. E. (2013), 'Quantifying trading behavior in financial markets using google trends', *Scientific reports* **3**, 1684.

Qin, J., Liu, Y. and Grosvenor, R. (2016), 'A categorical framework of manufacturing for industry 4.0 and beyond', *Procedia Cirp* **52**, 173–178.

Schedin, E. (1994), 'Galling mechanisms in Sheet Forming Operations', *Experimental Techniques* **179**, 123–128.

Shercliff, H. and Ashby, M. (1990), 'A process model for age hardening of aluminium alloysâĂŤi. the model', *Acta Metallurgica et Materialia* **38**(10), 1789–1802.

So, H. (1996), 'Characteristics of wear results tested by pin-on-disc at moderate to high speeds', *Tribology International* **29**(5), 415–423.

Socher, R., Karpathy, A., Le, Q. V., Manning, C. D. and Ng, A. Y. (2014), 'Grounded compositional semantics for finding and describing images with sentences', *Transactions of the Association for Computational Linguistics* **2**, 207–218.

Standard Test Method for Wear Testing with a Pin-on-Disk Apparatus (2016), *ASTM Standard* .

Sun, Y., Wang, K., Politis, D. J., Chen, G. and Wang, L. (2020), 'An experimental investigation on the ductility and post-form strength of a martensitic steel in a novel warm stamping process', *Journal of Materials Processing Technology* **275**, 116387.

Tang, Q., He, J. and Zhang, W. (2015), 'Influencing factors of thermal contact conductance between tc4/30crmnsi interfaces', *International Journal of Heat and Mass Transfer* **86**, 694–698.

Turetta, A., Bruschi, S. and Ghiotti, A. (2006), 'Investigation of 22mnb5 formability in hot stamping operations', *Journal of Materials Processing Technology* **177**(1-3), 396–400.

Wang, A., El Fakir, O., Liu, J., Zhang, Q., Zheng, Y. and Wang, L. (2019), 'Multi-objective finite element simulations of a sheet metal-forming process via a cloud-based platform', *The International Journal of Advanced Manufacturing Technology* **100**(9-12), 2753–2765.

Wang, L., El Fakir, O., Sun, Y., Ji, K., Luan, X., Cai, Z. and Liu, X. (2019), 'A method of forming parts from sheet metal'.

Wang, L., He, Y., Zhou, J. and Duszczyk, J. (2010), 'Effect of temperature on the frictional behaviour of an aluminium alloy sliding against steel during ball-on-disc tests', *Tribology International* **43**(1-2), 299–306.

Wang, L., Zhou, D., Yuan, X., Gao, H., Wang, A., Liu, J., Fakir, E. O., Politis, D. J. and Lin, J. (2016), 'Knowledge Based Cloud FE Simulation of Sheet Metal Forming Processes', *Journal of Visualized Experiments Knowledge Based Cloud FE Simulation of Sheet Metal Forming Processes* .

Watanabe, H., Mukai, T., Kohzu, M., Tanabe, S. and Higashi, K. (1999), 'Effect of temperature and grain size on the dominant diffusion process for superplastic flow in an az61 magnesium alloy', *Acta materialia* **47**(14), 3753–3758.

Wilson, D. and Martinez, T. R. (2003), 'The general inefficiency of batch training for gradient descent learning', *Neural Networks* **16**(10), 1429–1451.
URL: *https://www.sciencedirect.com/science/article/pii/S0893608003001382*

Yanagida, A., Kurihara, T. and Azushima, A. (2010), 'Development of tribo-simulator for hot stamping', *Journal of Materials Processing Technology* **210**(3), 456–460.

Yuan, S., Li, F. and He, B. (2008), 'Relationship between lode parameter and deformation type', *J. Harbin Inst. Technol* **40**(1), 61–64.

Zaremba, W., Sutskever, I. and Vinyals, O. (2014), 'Recurrent Neural Network Regularization'.
URL: *http://arxiv.org/abs/1409.2329*

Zhang, Q., Luan, X., Dhawan, S., Politis, D. J., Du, Q., Fu, M. W., Wang, K., Gharbi, M. M. and Wang, L. (2019), 'Development of the post-form strength prediction model for a high-strength 6xxx aluminium alloy with pre-existing precipitates and residual dislocations', *International Journal of Plasticity* **119**, 230–248.

Zhou, K., Liu, T. and Zhou, L. (2015), Industry 4.0: Towards future industrial opportunities and challenges, *in* '2015 12th International conference on fuzzy systems and knowledge discovery (FSKD)', IEEE, pp. 2147–2152.